

5-2018

Evaluation of Thermal Mechanisms to Predict the Transient Electroplastic Effect in Aluminum and an Investigation of Electrically Assisted Drilling

Brandt J. Ruskiewicz
Clemson University, brandtruszki@gmail.com

Follow this and additional works at: https://tigerprints.clemson.edu/all_dissertations

Recommended Citation

Ruskiewicz, Brandt J., "Evaluation of Thermal Mechanisms to Predict the Transient Electroplastic Effect in Aluminum and an Investigation of Electrically Assisted Drilling" (2018). *All Dissertations*. 2113.
https://tigerprints.clemson.edu/all_dissertations/2113

This Dissertation is brought to you for free and open access by the Dissertations at TigerPrints. It has been accepted for inclusion in All Dissertations by an authorized administrator of TigerPrints. For more information, please contact kokeefe@clemson.edu.

EVALUATION OF THERMAL MECHANISMS TO PREDICT THE TRANSIENT
ELECTROPLASTIC EFFECT IN ALUMINUM AND AN INVESTIGATION OF
ELECTRICALLY ASSISTED DRILLING

A Dissertation
Presented to
the Graduate School of
Clemson University

In Partial Fulfillment
of the Requirements for the Degree
Doctor of Philosophy
Automotive Engineering

by
Brandt J. Ruskiewicz
May 2018

Accepted by:
Dr. Laine Mears, Committee Chair
Dr. David Schmueser
Dr. Xin Zhao
Dr. Gang Li

ABSTRACT

The objective of this research is twofold: first, to evaluate if the microscale Joule heating theory can predict the transient electroplastic effect in 7075-T6 aluminum. Second, to determine if electrical application can have a significant impact on drilling of 1500MPa steel, and if the operation is predictable using a modified Merchant's machining model. Both 7075-T6 and 1500 MPa steel are of interest to the automotive industry due to their high strength-to-weight ratios. These metals are important to aid in lightweighting to meet increasingly strict governmental fuel economy standards. However, the strength of the steel makes it difficult to machine in post-forming operations. The ductility of the aluminum makes it impossible to form using conventional methods, especially for deep parts such as a body side outer. A potential fix to these problems is electrical augmentation to locally or globally soften the metal. It has been shown that electricity can increase ductility/formability in metals while also decreasing the forming loads and stresses required (this group of phenomena is termed the *electroplastic effect*). While the effects of electricity are well known, the underlying mechanisms are not, resulting in four key theories, two of which have already been disproven.

This research examines one of the remaining two theories to predict the transient electroplastic effect. The microscale Joule heating theory suggests that microscale hot spots develop inside of the metal in areas of high electrical resistivity, such as grain boundaries where dislocations pile up during deformation. A coupled mechanical-thermal-electrical model was partitioned with grains, grain boundaries, and precipitates. Temperature and dislocation density-dependent electrical resistivity was used in order to evaluate the

microscale Joule heating theory. It was found that this theory cannot fully explain the resultant stress drop caused during the transient phase of electrically-assisted pulsed tension. During model testing it was discovered that electricity changes the strain hardening behavior of aluminum. To further investigate, the effect of electricity on precipitates was explored through measurement of precipitate size and distribution in specimens treated with different electrical treatments.

An electrically-assisted drilling experiment was designed, fabricated, and tested to determine the effect of electricity on a drilling process. A design of experiments study was conducted on 1008 steel to determine if electric current had a significant effect on process temperature, axial force, and tool wear compared to inputs of feedrate and spindle RPM. It was found that current was dominant and that tool wear and cutting forces could be decreased with electric current. The first electrically-assisted drilling model was created by modifying Merchant's machining model. This model was found to have shortcomings due to knowledge limitations on friction and equipment limitations on temperature measurement. The knowledge generated from the 1008 experiments was used to further the constraining limits of the drilling process, leading to 1000% tool life improvement on drilling of 1500 MPa steel while increasing the achievable feedrate for cutting by 200%.

DEDICATION

*To my Parents James and Mary Ruszkiewicz
For their unconditional love, support, and guidance*

*To my Girlfriend of 7 Years Katie Carone
For her encouragement and support throughout my academic career*

ACKNOWLEDGMENTS

I would like to express my deepest appreciation to my advisor Dr. Laine Mears for his guidance and support throughout my graduate career. You have taught me many valuable lessons applicable to both research and life and have helped me to define my future.

Next, I would like to thank Dr. John T. Roth for his guidance during my undergraduate career and belief that I could become a great researcher. The opportunities and advice that you gave me during my time at Penn State and Clemson have greatly shaped my career and my decision to become a professor.

I extend my thanks to the professors and staff that have aided me throughout my research career: Dr. Ihab Ragai, Glenn Craig, Gary Mathis, Dr. Chetan Nikhare, and Dr. Hongseok Choi.

Thank you to my research committee for helping me to conduct the best research that I was able to: Dr. Xin Zhao, Dr. David Schmueser, and Dr. Gang Li.

I would like to thank the members of Dr. Mears research team Farbod, Abram, Matt, Jamie, Lujia, Durul, and Vassilis for their camaraderie, support, and ability to turn a conference into a party.

Finally, I would like to thank my parents for always pushing me to be my best and to succeed and my girlfriend Katie Carone for her encouragement to finish my degree.

TABLE OF CONTENTS

	Page
TITLE PAGE	i
ABSTRACT	ii
DEDICATION	iv
ACKNOWLEDGMENTS	v
CHAPTER	
1. INTRODUCTION	1
Research Objective	1
Motivation.....	1
Problem Statement.....	3
Research Questions.....	5
2. BACKGROUND ON THE ELECTROPLASTIC EFFECT	6
The Electroplastic Effect and Its Uses.....	6
The Four Major Theories.....	11
The Electroplastic Effect View	14
Thermal Softening View.....	21
Conclusions.....	26
3. BACKGROUND ON ALUMINUM	29
Metallic Bonds.....	29
Metallic Lattice Defects.....	29
Metal Crystal Plasticity and Dislocation Modeling.....	31
Aluminum Alloys and Strengthening Mechanisms	35
4. EVALUATION OF THE MIROSCALE JOULE HEATING THEORY	41
Table of Contents (Continued)	

Table of Contents (Continued)

	Page
Evaluation of Recent Studies in Electroplastic Theory	41
Experimental Setup.....	44
Literature Based Bulk Joule Heating Model.....	46
Grain Boundary Model (Scaled Model)	53
Precipitate Model.....	61
Grain Boundary Thickness Sensitivity	64
Conclusions.....	68
5. THE BULK MODEL, ELECTRICAL RESISTIVITY, CURRENT DENSITY	70
Current Density Evaluation.....	70
Evaluation of the Bulk Model and Electrical Resistivity Modeling	77
Conclusions.....	83
6. A NEW THOERY: ELECTRON STAGNATION.....	85
The 5 Criterion of an Electroplastic Effect Theory	85
The Electron Stagnation Theory	86
Analogy of the Electron Stagnation Theory	88
Satisfaction of the 5 Criterion	89
7. EFFECT OF ELECTRICITY ON PRECIPITATES IN ALUMINUM	93
Precipitate Measurement and Microscopy.....	93
The Effect of Current Density on Precipitation	94
Conclusions.....	103
8. THE ELECTROPLASTIC EFFECT AT ELEVATED STRAIN RATE.....	105
Experimental Setup and Control	105
The Existence of the Electroplastic Effect at High Strain Rate	106
Conclusions.....	111

Table of Contents (Continued)

	Page
9. ELECTRICALLY ASSISTED DRILLING	113
Electrically-assisted Machining	113
Experimental Setup	114
Design of Experiments for 1008CR Steel.....	115
Model of Electrically-assisted Drilling	121
Effect of Electricity on Tungsten Carbide and its Implication on EA Machining....	134
Elevated Feedrate Drilling of 1500MPa Steel	139
Hole Quality and Heat Affected Zone	151
Conclusions.....	155
10. SUMMARY AND CONCLUSIONS	157
Intellectual Merit.....	157
Broader Impacts	158
Future Work and Recommendations	159
11. APPENDICES	160
ABAQUS Subroutine.....	160
Matlab Code for Creating Subroutine Data	161
Matlab Code for Drilling Model	163
REFERENCES	174
LIST OF JOURNAL ARTICLES.....	185
CONFERENCE PROCEEDINGS AND PRESENTATIONS	186

LIST OF FIGURES

Figure	Page
1-1 Failure of thermal softening models to predict the stress reduction in the presence of pulsed electric current.....	4
2-1 Uniaxial tension behavior in electrically-assisted tension of commercially pure titanium [9].....	6
2-2 Pulsed current tension of 5754 aluminum leading to 250% ductility improvement .	7
2-3 Brittle to ductile transformation in electrically-assisted impression die forging	8
2-4 Constant current density (CCD) vs. non-constant current density (NCCD) effect on flow stress in 304 stainless steel	9
2-5 Current density's effect on energy requirement for open die forging of various metals	10
2-6 (left) Electrically-assisted compression vs. isothermal compression for titanium [24] (right) Heated tension of 6061-T6511 vs. annealed electrically pulsed specimens [60]. Note the lower flow stress in the presence of electric current	14
2-7 Temperature prediction using an energy balance for electrically-assisted tension for both stationary and deformation testing [7]	18
2-8 Flow stress prediction using modified power law and energy balance [7]	19
3-1 Vacancies and interstitials in a metallic lattice.....	30
3-2 Edge dislocation visualization	31
3-3 Screw dislocation visualization	31
3-4 Crystal Slip Planes in FCC	33
4-1 Experimental setup for electrically-assisted tension	45
4-2 Stress and temperature results compared to 0A baseline for 60 second period square wave forms.....	46

List of Figures (Continued)

Figure	Page
4-3 Model setup, boundary conditions applied at the outer partitioned regions.....	47
List of Figures (Continued)	
4-4 Isothermal model vs. experiment at room and elevated temperature	48
4-5 Bulk model vs experiment, temperature and stress result, note that the model cannot predict the correct stress drop even with the correct temperature	49
4-6 Electrical conductivity vs. stress at various temperatures (°C) with a grain boundary multiplier of 1000	53
4-7 (Left) Traced grain boundaries from EBSD of as-received 7075-T6 aluminum and (right) partitioned grain boundaries in ABAQUS.....	54
4-8 Axial stress and temperature prior to the first electrical pulse from the bulk model showing the location of the grain boundary model; axial stress in this area is 533 MPa. The temperature result from the bulk model shows that there is a uniform temperature where the grain boundary specimen is taken	55
4-9 Comparison of temperature and stress for the 1 st electrical pulse for experiment, bulk model, and scaled model with homogeneous properties	57
4-10 Comparison between experiment, bulk, and scaled model fit to experiment for the first electrical pulse	59
4-11 Current density field caused by grain boundary portioning (A/mm ²)	60
4-12 Precipitates in 7075-T6 as-received material	62
4-13 (Top) Entire specimen with grain boundaries and precipitates (bottom) zoomed in area to show precipitates	63
4-14 Current density results (top) with precipitates (bottom) without precipitates, units are A/mm ²	64
4-15 Hexagon grains and grain boundaries used in the sensitivity study	65
4-16 Power curve fit for grain boundary multiplier as a function of grain boundary thickness.....	67

List of Figures (Continued)

Figure	Page
4-17 Current density results from 0.375 micron grain boundary thickness model, units are A/mm ²	68
5-1 Experimental stress (left) and temperature (right) results at 0.001/sec strain rate for (a) 60sec period waves, (b) 20sec period waves, (c) 10sec period waves, (D) 3.5sec period waves	74
5-2 Correlation between input of energy and outputs of 1 st pulse stress, average temperature, and maximum temperature	76
5-3 Model vs. experiment for 0A tension of 7075-T6 at 2 strain rates.....	78
5-4 Temperature (left) and stress (right) experiment vs. model results for (a) continuous current for both strain rates, (b) 2 wave forms at 0.001/s strain rate, (c) 2 wave forms at 0.01/s strain rate	80
5-5 Accuracy of the temperature prediction of the bulk model, the yellow vertical line is at 89A/mm ² , the horizontal line is at 10% accuracy. Note that increasing loss in accuracy as current density increases past 89A/mm ²	81
6-1 Increased electron density at an obstacle due to electron stagnation, the large blue dot is an obstacle, the smaller black dots are electrons.....	87
7-1 Precipitate measurement, the dark spots are precipitates. The precipitate size is found by averaging the vertical and horizontal spans	94
7-2 TEM images of precipitates from electrically-assisted tension conducted at a strain rate of 0.001/s, (a) as received, no deformation, (b) 15 A/mm ² continuous, (c) 71CD3D60P, (d) 225CD0.3D60P.....	97
7-3 TEM images of precipitates from electrically-assisted tension conducted at a strain rate of 0.01/s, (a) as received, no deformation, (b) 15 A/mm ² continuous, (c) 28CD1D3.5P, (d) 89CD0.3D10P.....	98
7-4 Precipitate size and distribution vs. current density, error bars represent 1 standard deviation.....	99
7-5 Correlation plots from trend analysis for precipitate size and density vs maximum temperature and current density	101

List of Figures (Continued)

Figure	Page
8-1 Images captured at the onset of arcing due to specimen fracture, A8201	106
8-2 Stress-strain results from elevated strain rate testing (a) 0.001/s, (b), 0.01/s, (c) 0.1/s, (d) 1/s	108
8-3 Overheating of the necking/fracture zone at 0.001/s strain rate	109
8-4 Explosive arcing during specimen failure, (left) 200A/mm ² 0.1/s, (right) 200A/mm ² 1/s	109
9-1 Schematic of an electrically-assisted drilling setup	115
9-2 Main effects plot for axial force during EA drilling of 1008CR steel	116
9-3 Axial force and temperature comparison for 3 sequential drilling operations conducted at 300A, 350RPM, and 25.4mm/min	118
9-4 Main effects plot for maximum temperature in EA drilling of 1008CR steel	119
9-5 Temperature comparison for (a) 300A, (b) 150A, and (c) 0A in different drilling conditions of 1008CR steel	120
9-6 Main effects plot for average flank wear in EA drilling of 1008CR steel	121
9-7 Example of nodal setup for a single element in 2D explicit finite volume heat transfer model, viewed from the top	122
9-8 Contact segments for drilling of thin sheets where tapered bit length is less than the sheet thickness	126
9-9 Model vs. experiment for maximum temperature and axial force during EA drilling process of 1008CR steel at 350RPM and 12.7mm/min for (a) 300A, (b) 150A, and (c) 0A	127
9-10 Temperature contour comparison between model and thermal camera experimental data for 1008CR steel	132
9-11 Compression dies used during testing	135
9-12 Brittle fracture of WC in compression	136

List of Figures (Continued)

Figure	Page
9-13 Stress/strain curves for EA compression of WC at various current densities List of Figures (Continued)	137
9-14 WC with a current density of 50A/mm ² , note the color change due to heat	137
9-15 Tool wear from EA turning [8].....	139
9-16 Main effects plot for maximum axial force during EA drilling of PHS1500.....	142
9-17 Axial force comparison for different current magnitudes (a) 50.8 mm/min 1 st cut, (b) 50.8 mm/min 3 rd cut, (c) 101.6 mm/min 1 st cut, and (d) 101.6 mm/min 3 rd cut. Cut 1 shown for the 1 st and 3 rd cuts for 50.8 mm/min due to failure. Cut 2 shown for 0A 3 rd cut at 101.6mm/min due to bit failure on the 2 nd cut	143
9-18 Main effects plot for maximum temperature during electroplastic drilling of PHS1500	146
9-19 Temperature comparison for different current magnitudes (a) 50.8 mm/min 1 st cut, (b) 50.8 mm/min 3 rd cut, (c) 101.6 mm/min 1 st cut, and (d) 101.6 mm/min 3 rd cut. Cut 1 shown for the 1 st and 3 rd cuts for 50.8 mm/min due to failure. Cut 2 shown for 0A 3 rd cut at 101.6mm/min due to bit failure on the 2 nd cut	147
9-20 Axial force results for 3 sequential cuts for (a) 0A 50.8mm/min, (b) 300A 50.8mm/min, (c) 600A 50.8mm/min, (d) 0A 101.6mm/min, (e) 300A 101.6mm/min, (f) 600A 101.6mm/min	148
9-21 Axial force results for cutting to failure for (a) 300A 50.8mm/min, (b) 600A 50.8mm/min, (c) 300A 101.6mm/min, (d) 600A 101.6mm/min	149
9-22 Extrusion height for first 3 cuts over all parameter sets tested. At 50.8mm/min the 300A and 600A cases produced the same result on the first cut	152
9-23 Vickers hardness measurements taken radially from the drilled hole for each parameter set after the 1 st cut	155

LIST OF TABLES

Table	Page
1-1 Lightweight materials and their potential mass reductions	2
4-1 Johnson-Cook plasticity model for 7075-T6 Aluminum.....	49
4-2 Comparison of stress and temperature at the end of 3 electrical pulses. The scaled model represents the scaled model with homogenous properties. The scaled model fit is the scaled model with the grain boundary dislocation density factor set to predict the correct flow stress drop.....	58
4-3 Material constants and resultant grain boundary thickness for 9 micron hexagon grains.....	66
5-1 Square wave forms to nominally match the electrical energy from a continuous electrical application and the actual energy calculated after experiment for each waveform	72
5-2 Quadratic and linear regression accuracy between inputs and outputs for use in replacing current density. Values greater than 0.65 are highlighted green.....	75
5-3 Johnson-Cook Parameters for Bulk Model Evaluation Study.....	77
5-4 Linear and quadratic curve fit coefficients to show predictability of the electroplastic effect when high current densities are ignored	83
7-1 Average precipitate size and density comparison of electrically-assisted tensile specimens.....	96
7-2 Correlations between inputs and process results on precipitate size and density, green highlight is applied to $R^2 > 0.65$	99
8-1 Current density used for each strain rate tested.....	106
8-2 Thermal camera comparison	106
8-3 Tabular results from elevated strain rate tensile testing	110
9-1 Inputs and outputs for DoE for 1008CR steel	115
9-2 Tool wear images for EA drilling of 1008CR steel at 350RPM	117

List of Tables (Continued)

Table	Page
9-3 Johnson-Cook plasticity model parameters for mild steel.....	124
9-4 Model accuracy results for maximum axial force during drilling of 1008CR steel across all parameter sets, underlines tests experienced arcing	128
9-5 Model accuracy results for maximum temperature during drilling of 1008CR steel across all parameter sets, underlines tests experienced arcing	129
9-6 Summary of testing.....	135
9-7 DoE for PHS1500 Steel.....	140
9-8 Tooling images after 3 cuts in drilling PHS1500 steel for 2 different feedrates and 3 different currents.....	141
9-9 Maximum force and temperature results from high feedrate drilling of PHS1500 steel	144
9-10 Tooling after failure testing, all bits are failed except for 600A at 50.8 mm/min. 300A at 101.6mm/min has chips and a large crack through the carbide portion of the bit	150

CHAPTER ONE

1. INTRODUCTION

Research Objective

The objective of this research was to first evaluate one of the theories that seeks to explain the unpredictable transient electroplastic effect (microscale Joule heating theory). Second, to determine the advantageous effects of electricity on a drilling process and to create the first electrically-assisted machining model. The microscale Joule heating theory was evaluated through a Finite Element Analysis (FEA) model with grains, grain boundaries, and precipitates partitioned with electrical resistivity as a function of temperature and dislocation density, or of temperature and a resistivity multiplier. The effect of electricity on a drilling process was examined using Design of Experiments (DoE) to quantify the primary and interaction effects between electric current, feedrate, spindle rotational speed, and number of cuts on the outputs of process temperature, axial cutting force, and tool life. Merchant's machining model is modified and coupled with a 2D finite volume heat transfer analysis to predict process temperature and force.

Motivation

The Corporate Average Fuel Economy (CAFE) standards for 2025 require the fleet average fuel economy of automotive OEMs to be 54.5mpg [1]. There are many different methods to achieve this goal, such as improvements in conventional powertrain efficiency or the use of hybrid and electric vehicles. Hybrid and electric these vehicles have heavier drive lines than conventional gas combustion engines which counteracts some of the increase in fuel economy gained from these propulsion systems. In order to further increase the fuel economy, OEMs must turn to lightweighting. Lightweighting utilizes materials

with a high strength to weight ratio; examples of such materials are shown in Table 1-1 along with potential mass savings compared to conventional low carbon steels used in the automotive industry.

Table 1-1: Lightweight materials and their potential mass reductions

Lightweight Material	Mass Reduction Possible
Magnesium	30-70%
Carbon Fiber Composites	50-70%
Aluminum	30-60%
Titanium	40-55%
Glass Fiber Composites	25-35%
Advanced High Strength Steels	15-28%
High Strength Steels	10-20%

The use of lightweight materials can result in a 6-8% fuel economy improvement for every 10% reduction in vehicle mass [2]. However, many of these new lightweight materials present problems for convention forming and joining processes due to elevated strength (*e.g.*, high strength steel) that lead to die damage and accelerated die wear in stamping, as well as reduced formability (*e.g.*, aluminum and magnesium), significantly limiting the shapes that can be formed [3; 4]. While it is possible to purchase new machinery designed to form new lightweight materials, this comes with a hefty price tag as full stamping lines for an OEM or Tier 1 supplier can reach 100 million USD. As such, manufacturers have turned to thermal augmentation as a lower cost solution to process these materials in conventional equipment. This approach manifests itself as warm, hot, or incremental heated forming to reduce part strength or increase ductility leading to increased

formability [5; 6]. However, conventional heating techniques that use furnaces are inefficient due to losses in the conveyor style setups typically used in the automotive industry.

Electricity has been shown to decrease flow stress and increase ductility in sheet metal forming similar to furnace-based methods. Electrical treatment can heat a part faster and can target specific areas compared to furnace treatment, which is advantageous for heat treated parts where the manufacturer does not want to change the properties of an entire part. Later in this work, a case was examined whereby a part is heated from 25°C to 570°C in 0.3 seconds, much faster than what is attainable using conventional furnace heating methods. Electricity can also be applied directly to stamping dies, removing the need for extra processing stations in the manufacturing line. However, the machinery needs to have its electrical circuits isolated from the applied electric current in order to prevent destruction of controlling equipment. In addition, high strength parts that require further processing to fix a defect or to add a feature post-forming often require laser-assisted machining techniques. These expensive techniques could be potentially replaced with electrical augmentation to drive down the cost of these machining operations. The use of electricity in manufacturing is promising, but remains unpredictable due to a lack of understanding of the fundamentals of the effect of electricity on deformation in metals.

Problem Statement

The electroplastic effect is the effect of electricity on metals during deformation, it leads to reduced flow stress and increased ductility in forming processes and reduced cutting loads in machining. The electroplastic effect uses are well documented in the

literature, but it remains unpredictable due to a lack of knowledge of its fundamental mechanisms. The inability of a thermal softening model to account for the stress reduction in the presence of a pulsed electric current is shown in Figure 1-1 [7].

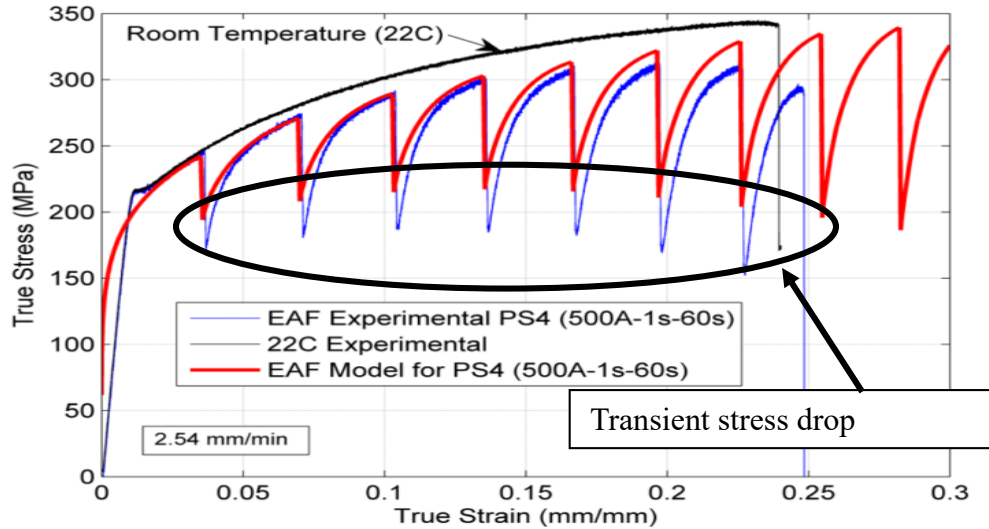


Figure 1-1: Failure of thermal softening models to predict the stress reduction in the presence of pulsed electric current

Two of four potential theories have been invalidated for short-term transient situations where strain and temperature are continually evolving. The leading remaining theory is the microscale Joule heating theory, whereby increased electrical resistivity near grain boundaries and precipitates leads to increased Joule heating (*i.e.*, hot spots), and thereby enhance softening at localized points within the metal. These hot spots could lead to the correct prediction of the transient stress drop in Figure 1-1. If the electroplastic effect cannot be effectively predicted then it cannot be reliably used in industry, limiting the progression of this as a promising technology. As such, it is crucial to evaluate existing theories and if necessary propose new theories to predict the electroplastic effect.

Often times high strength parts require post forming modification through machining, or high strength components must be machined from hard to machine materials. Machining high strength parts accelerates tool wear, leading to increased tool costs and eventually increased product cost. It has been shown that electricity can reduce cutting forces in machining [8], but there has not yet been a comprehensive study to characterize an electrically-assisted machining process and to determine potential advantages with respect to tool life, temperature, and cutting forces. In order for electrically-assisted machining to compete with similar augmented techniques such as ultrasonically-assisted and laser-assisted machining, a greater understanding of the effect of electricity on a drilling process must be achieved and modeled.

Research Questions

To further the field of EAM, the following research questions must be addressed:

Research Question 1: Can the transient stress drop be predicted using the microscale Joule heating theory, where a heterogeneous resistivity field exists at localized regions of high electrical resistivity due to precipitate and dislocation concentration? Are further theories necessary to understand the electroplastic effect?

Research Question 2: What are the advantageous effects of electricity on a drilling process with respect to tool life and cutting forces? Can the process be modeled by adapting an existing machining model to correctly predict the temperature and cutting forces through the process? Is this technology applicable to the automotive industry for post-forming machining of high strength components?

CHAPTER TWO

2. BACKGROUND ON THE ELECTROPLASTIC EFFECT

The Electroplastic Effect and Its Uses

The Electroplastic Effect in Tension

Typically, an electrically-assisted tension test shows a reduction of flow stress and may show an increase in fracture strain (*i.e.*, ductility) compared to forming in the absence of electricity. The reduction in flow stress corresponds with a reduction in forming force or required deformation energy. An example is shown in Figure 2-1, which shows the effect of continuous current application during tension of commercially pure titanium [9].

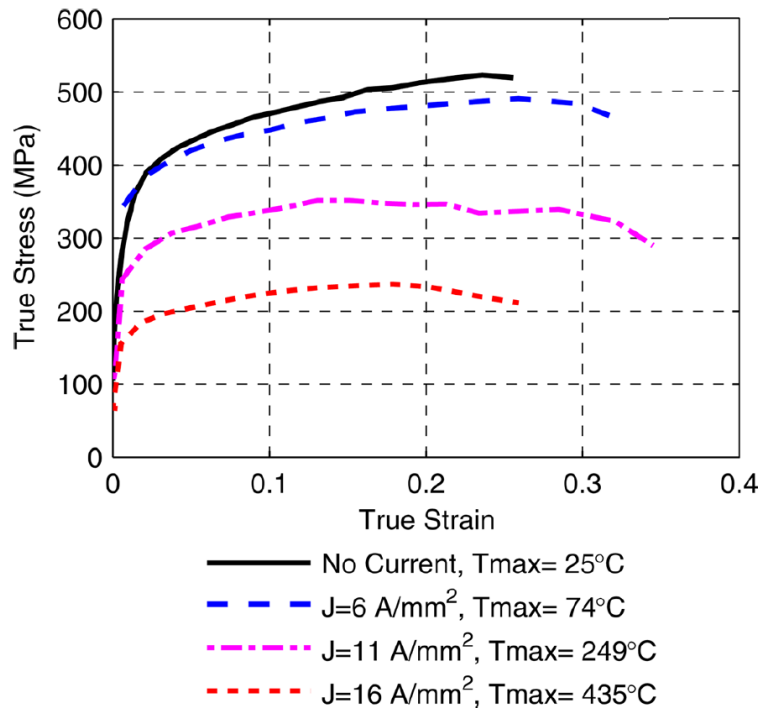


Figure 2-1: Uniaxial tension behavior in electrically-assisted tension of commercially pure titanium [9]

The magnitude of this reduction positively correlates with grain size. Smaller grains result in greater flow stress reduction, while larger grains result in a lower flow stress reduction [10-16]. Additional effects include the elimination of Lüder's band formation

shown during tensile deformation of 5083 aluminum and a reduction in anisotropic effects in the same metal [17]. Continuous application of constant direct current in tension has been shown to cause reduced fracture strain as compared to non-electrical tests. This is due to the increase in current density caused at the onset of localized necking [7; 18]. As the necking zone area decreases, the current density and subsequent heat generation rapidly increase. This leads to over-softening of the metal and premature failure during continuous current application. It has been shown that alternating current or square wave pulsed direct current can aid in reducing over-softening of the necking zone, an example of which is shown in Figure 2 [19; 20].

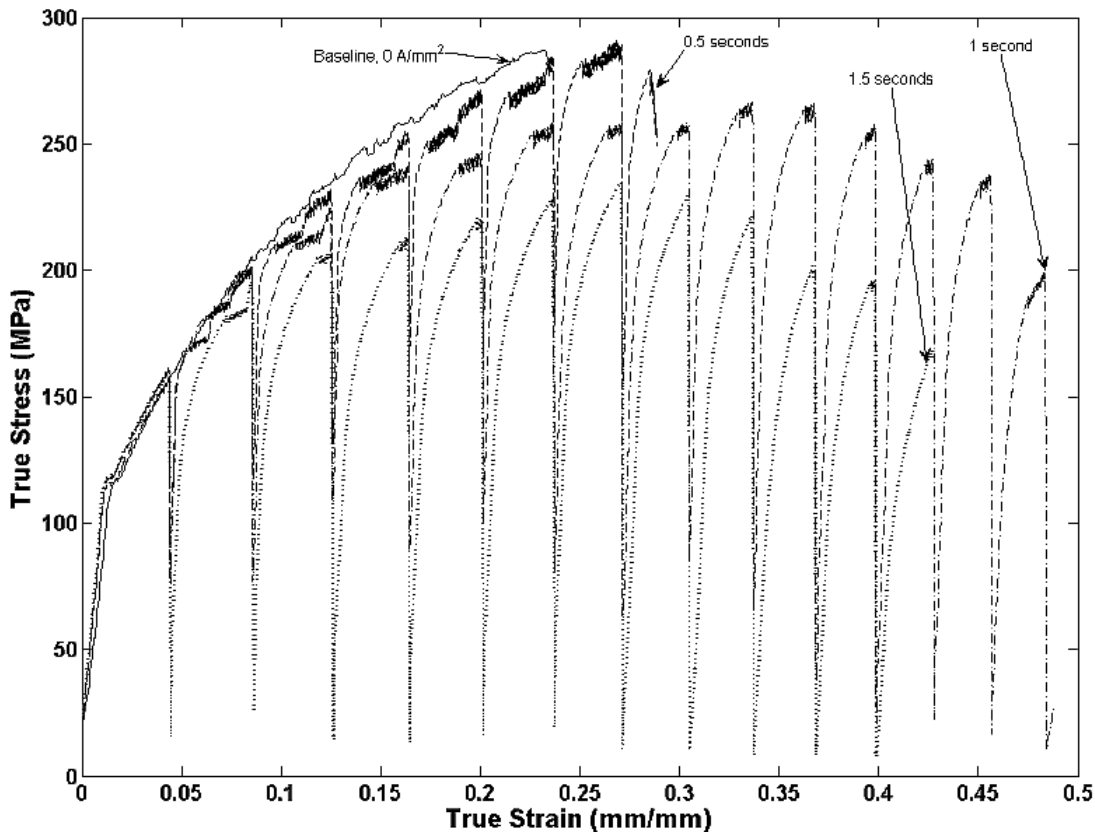


Figure 2-2: Pulsed current tension of 5754 aluminum leading to 250% ductility improvement [19]

While pulsed current application leads to greater ductility, it will also yield a greater

magnitude flow stress and forming force than continuous current application. The effect of electric field application has also been studied, and shown to have similar results as directly applying current to a part [21-23]. Additionally, an increase in whisker formation is seen as small, thin extrusions protruding from the surface of the material. Whisker formation is a result of transgranular dislocations, grain boundary sliding, and diffusion creep; all of which have been shown to accelerate when electricity is applied.

The Electroplastic Effect in Compression and Forging

Common effects seen during electrically-assisted compression tests across many materials are: reduction in compressive flow stress, decrease in elastic modulus, increase in formability, elimination of brittle crack initiation and propagation, and decrease in specific energy for deformation [24-26]. As an example, during impression die forging of magnesium AZ31B, it was found that below a current density of 30 A/mm^2 the magnesium fractured and had poor formability, while above this threshold density, there was no cracking during forging, as shown in Figure 2-3 [27].

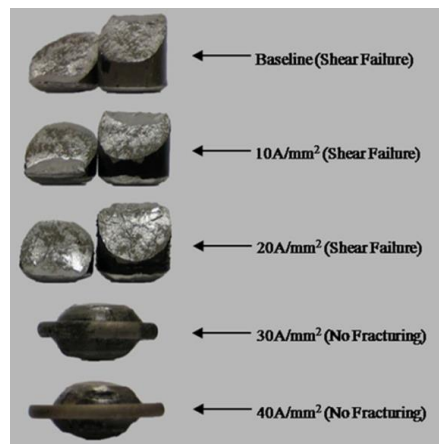


Figure 2-3: Brittle to ductile transformation in electrically-assisted impression die forging [27]

During electrically-assisted forming, small oscillations in the forming load can be observed, which could be due to a cyclic softening/hardening phenomenon [28]. Unlike tensile testing, continuous current is typically favored over pulsed current when deforming under compressive loads since the cross-sectional area of the specimen increases with deformation. This results in a continuously decreasing current density and subsequent decreasing electroplastic effect. To further examine this effect, testing that maintained constant current density (current increased proportional to specimen's cross sectional area increase) in the specimen throughout the compression cycle was conducted and compared with typical nominal current density testing (current density set based on initial area) [29]. The results can be seen in Figure 2-4, and show that applying constant current density (CCD) results in lower flow stress at higher strain than nominal or non-constant current density (NCCD).

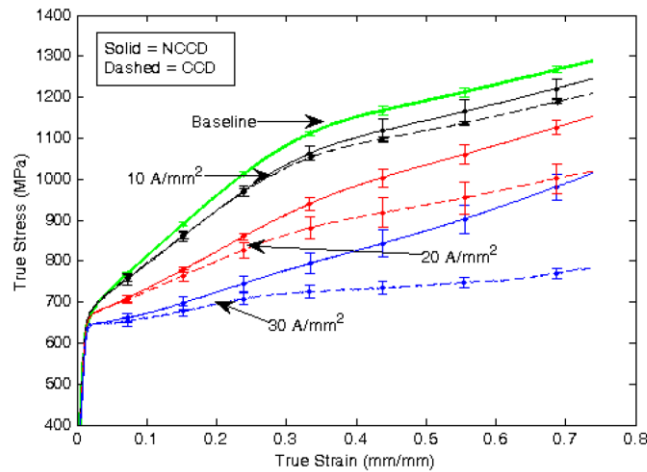


Figure 2-4: Constant current density (CCD) vs. non-constant current density (NCCD) effect on flow stress in 304 stainless steel [29]

In compression and tension, there is a phenomenon known as a threshold current density. Below a certain current density (material and process dependent) there will be

little effect from electricity, after a threshold value is reached, the effects are large [14; 15]. Threshold current densities are visible more often in compression for various materials than in tension, as shown in Figure 2-5 [25].

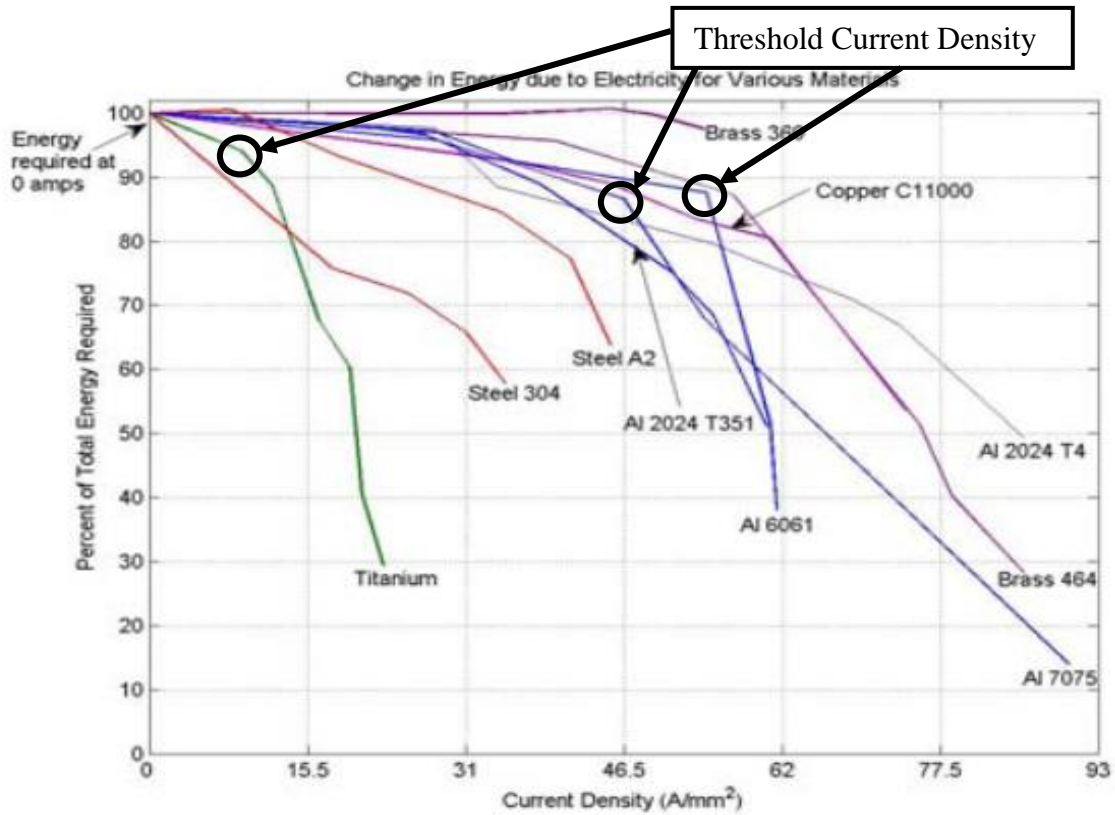


Figure 2-5: Current density's effect on energy requirement for open die forging of various metals [25]

The Electroplastic Effect in Complex Stress States

In simple and complex bending, similar trends as in tension and compression testing are seen in the presence of electric current. Bending forces may be reduced and ductility and formability may be increased [30-33]. An example of this effect can be seen in Li *et al.*'s work [32] for simple bending of titanium, without electric current there is cracking on the tensile edge of the specimen; with pulsed current the cracking is removed.

Subsequent to bending and other forming methods, electrical current has been

shown to have a significant effect on springback reduction in many materials such as advanced high strength steels, stainless steel, and 2024-T3 Al [34-38]. The material's springback can be effectively reduced by applying the electrical current through the area of residual stress concentration.

The Four Major Theories

The electroplastic effects are well documented experimentally, as shown in the previous section; however, the research community does not yet understand the fundamental mechanisms underlying the behavior. There are four theories that seek to explain the electroplastic effect.

Electron Wind. In the electron wind theory, electrons from an applied electrical current flow through a metal at a drift velocity and collide with stopped or mobile dislocations resulting in a momentum transfer from the electron to the dislocation [39-47]. This momentum transfer augments the dislocation motion, leading to flow stress reduction, increased ductility, reduced forming force, and reduced springback.

Metallic Bond Dissolution. In this theory, plastic flow is enhanced through the dissolution of metallic bonds brought on by excessive electron presence in the crystal lattice [48]. Metallic bonds are created by electron sharing in an electron cloud that surrounds positively charged ion cores. As current flow is applied to a metal, a proportional electron flow is induced. These additional electrons give rise to weakened bonding between the ion cores due to decreased electron sharing. This theory can be extended to the case of extremely high current magnitude, where ion cores are all but free from electron sharing, and able to move through the metal's lattice, resulting in full bond dissolution and greatly decreased forming force, flow stress, and springback.

Joule Heating. The Joule heating theory has two forms, bulk homogenous Joule heating and heterogeneous microscale Joule heating. Bulk Joule heating is explained as heat generated from electric current as it flows across the internal material resistance due to electrons scattering off of ion cores, lattice imperfections, and dislocations [9; 49-51]. This heat generation induces thermal softening of the metal, allowing for increased formability and decreased flow stress, forming force, and springback. As such, the mechanisms of the bulk homogenous Joule heating theory is bulk homogenous thermal softening, the equivalent mechanism to heating a part in a furnace.

However, in order to explain the flow stress reduction that is observed beyond what would be achieved through isothermal heating, this theory has been extended to incorporate microscale Joule heating. In this embodiment, it is theorized that increased resistivity due to dislocations, lattice imperfections, stacking faults, lattice misalignment, and grain boundaries will lead to localized areas of increased temperature around heterogeneities beyond the bulk observed temperature, and account for improved dislocation motion in the same region [49]. This model version's mechanism is still thermal softening, however, it is a thermal softening mechanism exclusive to electrical augmentation due to the heterogeneous resistivity field and non-uniform heating. Researchers have postulated that bulk Joule heating accounts for 40-70% of the electroplastic effect [43; 51-55]. This theory is evaluated in this research dissertation.

Magnetoplasticity. In magnetoplasticity theory, the electric current through a part causes a magnetic field, which results in easier dislocation motion, and therefore reduced flow stress [56-58]. This is caused by the conversion of singlet to triplet states by the

electric field. Triplet states are at a higher energy state and allow for easier motion and overcoming of dislocation obstacles or for stuck dislocation to overcome their pinning obstacle and continue motion, resulting in increased dislocation depinning rates and decreased flow stress.

Most research work has simply tested for Joule heating effects versus other effects [9; 11; 14; 24; 59; 60]. It is difficult to directly test for microscale or atomic-scale dynamic effects such as dissolution of metallic bonds or the electron wind, while bulk thermal softening is more easily observed. Isothermal furnace-heated testing or isothermal cooling testing is compared with electrically-assisted processes to empirically determine the extent of the electroplastic effect, but more work is needed to design experiments to directly test competing theories. As such, models and experimental validation of these theories will be placed into 2 groups. The *Electroplastic Effect View* will comprise the theories of the electron wind, magnetoplasticity, and dissolution of metallic bonds. The *Thermal Softening View* will comprise both bulk and microscale Joule heating. It is important to note that Joule heating itself is electrical resistive heating and as such is an “electroplastic effect”, *i.e.* an effect caused by electricity and only electricity. However, the mechanism of the electroplastic effect in the Joule heating category is assumed to be bulk thermal softening so long as homogenous heating is also assumed; heterogeneous Joule heating based on increased electrical obstacles or resistivity may be attributable to only electricity, and similar results may not be obtainable using furnace-based heating.

The Electroplastic Effect View

Fan *et al.* conducted tensile tests of C260 brass in the presence of electrical current at two different grain sizes; electrical results were compared with furnace heating testing [14]. It was found that electricity caused a larger stress reduction than furnace heating alone for both grain sizes, even at the same temperature, as shown in Figure 2-6. Similar testing has been done in tension and in compression on various materials by other authors with similar results; in all cases electrical testing had lower flow stress than elevated temperature testing at the same temperature values [11; 14; 24; 59-62].

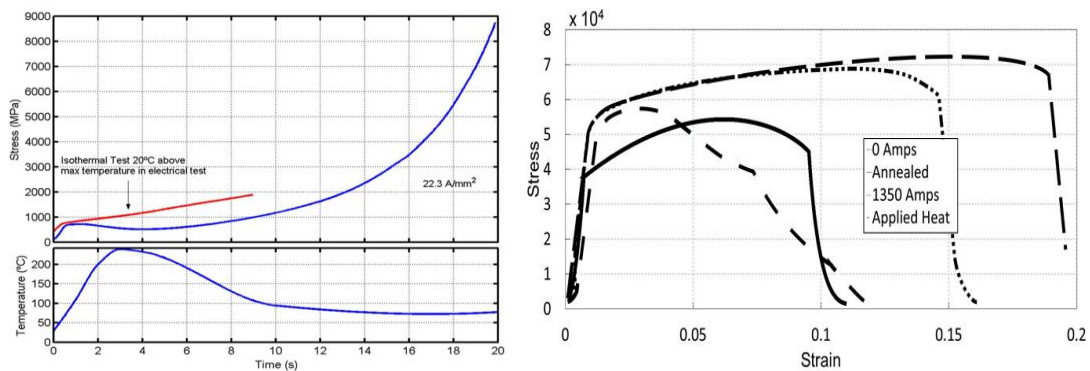


Figure 2-6: (left) Electrically-assisted compression vs. isothermal compression for titanium [24] (right) Heated tension of 6061-T6511 vs. annealed electrically pulsed specimens [60]. Note the lower flow stress in the presence of electric current

Fan *et al.* also found that smaller grains resulted in increased Joule heating at the macro scale, along with increased flow stress [14]. The difference between elevated temperature testing and electrical testing increased for smaller grain sizes. When examined microscopically, it was found that grain boundary melting existed for the smaller grain materials. Interestingly, the maximum macroscale temperature observed for this test was only 570°C, while the melt temperature for the brass is 916°C. This suggests that there is

microscale Joule heating at a higher magnitude near grain boundaries which is unobservable on the macroscale.

Okazaki *et al.* examined three different mechanisms of the electroplastic effect in an attempt to gain a greater understanding as to the magnitude of each effect on the total effect of electricity in forming: skin, pinch, and Joule heating effects [51]. As shown above by comparing furnace heated testing to electrically-assisted testing, the electroplastic effect seems to have a greater effect on flow stress reduction than can be explained through thermal softening caused by Joule heating based temperature rise.

The skin effect is the localization of current near the specimen's surface arising from dynamic application of current; in this situation, the electrical distribution in the specimen is biased towards the edges, and is non-uniform. It was found that for a pulse frequency of 9 kHz in a 0.5 mm diameter cylindrical slug of titanium, the skin depth was 1.52 mm, which was 3 times the diameter of the cylindrical specimen tested. As such, it was determined that the skin effect had little contribution to the electroplastic effect.

The pinch effect is created by an intrinsic magnetic field created from the application of electricity, which produces radial compressive stress during compressive processing. This radial stress causes a decrease in the axial stress for a specimen in tension. It was concluded that when this equation was solved for a solid wire in tension at a current density of 5000 A/mm², the radial stress induced was only 0.33 MPa, which accounted for only 0.4% of the electroplastic effect seen in tension [51].

The final effect examined by Okazaki *et al.* was Joule heating, or simple resistive heating. The equation for simple Joule heating is shown in Equation 1, where I is current,

R is resistance, t is time, ΔT is the temperature change, and C_p is specific heat. It was shown that thermal softening due to the temperature rise from Joule heating was able to account for 40-70% of the flow stress reduction.

Temperature rise from Joule heating:

$$\Delta T = \frac{I^2 R t}{C_p} \quad (1)$$

Siopis *et al.* examined the effect of severe prior plastic deformation on the effect of electricity in C101 copper compression testing. This testing is significant since it compares the same material but with different degrees of cold work, each of which had similar temperature rises from the electric current [15]. As-received C101 copper was compared to copper specimens that were annealed and then passed through an equal channel angular extrusion (ECAE) die. The ECAE die has the same inlet and outlet diameter, but the specimen is passed through a 90° bend in the middle of the die. This constrained path induces plastic deformation/cold work, and reduces the grain size of the material without changing its geometry. The specimens were passed through the ECAE die until they had the same grain size as the as received material, but with a much greater degree of cold work. The specimens were then compressed while applying electricity. It was found that the stress reduction was much greater in the ECAE specimen when compared to the baseline test of the as-received copper. It was noted that the temperature difference between the two electrical test specimens was low. As such, the difference in flow stress was attributed to non-thermal electroplastic effects.

Though it has been shown so far that Joule heating is not able to completely account for the electroplastic effect, Jones (2012) modeled electrically-assisted tension of AZ31B magnesium using square wave pulsed electric current using a Joule heating based thermal softening approach [7]. An energy balance was used to predict temperature rise for a 1-dimensional nodal explicit solution. In order to account for necking and for the increase in temperature due to increasing current density, an empirical linear approach was used. The specimen's strain was mapped using an etched circle grid on the specimens. After each test, the strain for each element was used to determine deformation. Length, width, and thickness of each element was calculated by strain at each time step. This allowed for accurate prediction of the necking area and temperature for both deformation and stationary models, shown in Figure 2-7.

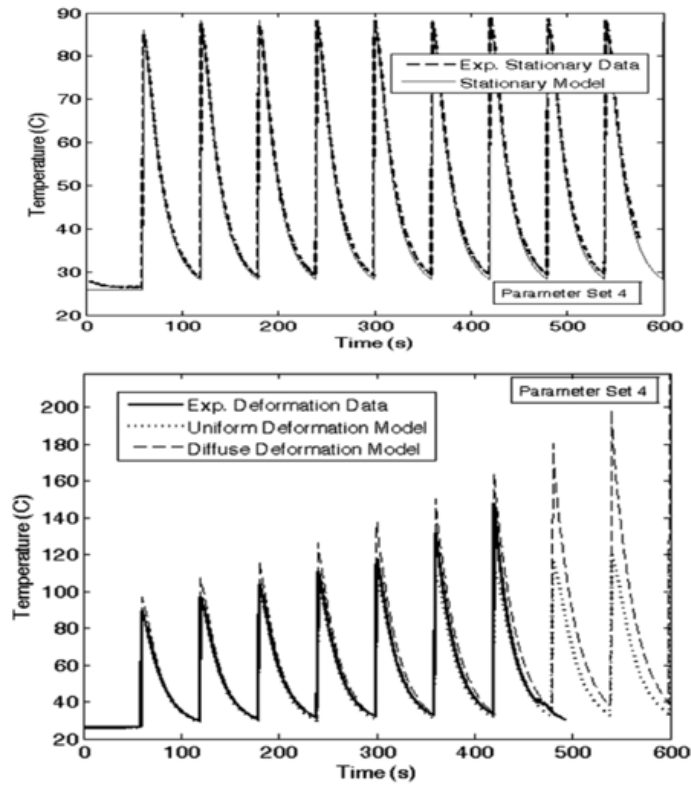


Figure 2-7: Temperature prediction using an energy balance for electrically-assisted tension for both stationary and deformation testing [7]

Material properties were modified during each time step using temperature-dependent material models. The temperature data was used to predict stress using a power law material model with an empirical softening exponent. As noted from the temperature plots, after each pulse (represented by a temperature spike) the temperature decreases to room temperature, at which point the cold flow stress would be expected. However, the recovered stress state is less than the original material, as shown in Figure 16.

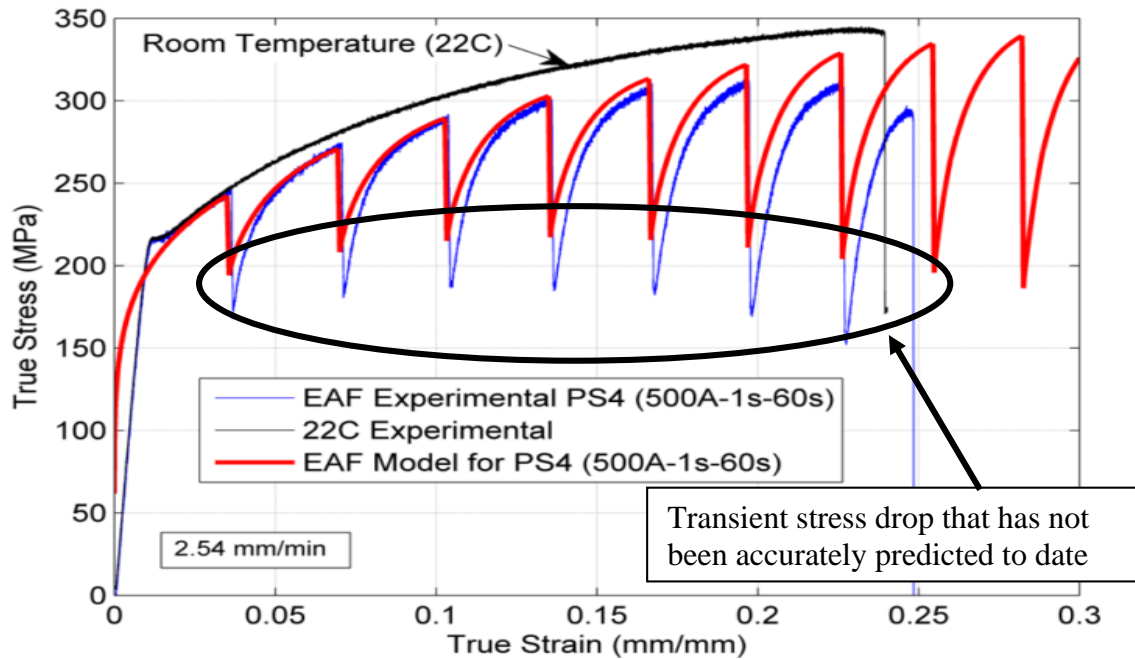


Figure 2-8: Flow stress prediction using modified power law and energy balance [7]

While the bulk temperature prediction is accurate using Joule heating as the only thermal input, the model fails to capture the transient stress drop seen during the onset of electric current agreeing with earlier shown works that the electroplastic effect cannot be fully understood using macro-scale Joule heating. A similar model was used for examining sawtooth waveforms for 7075-T6 aluminum in tension; the stress drop was again not accurately predicted by a bulk Joule heat model [63].

Hariharan *et al.* expanded upon Jones' model to create the current state of the art electroplastic effect prediction model by creating a coupled thermal-electrical-mechanical finite element model in ABAQUS[®] that solved for temperature and flow stress simultaneously rather than a cascading temperature - flow stress predictor [54]. 5052 aluminum ASTM E8 specimens were examined.

Heat transfer inside of the clamped regions was ignored and set to a constant value since the large grips act as heat sinks; only the exposed portion was modeled. Pulsed current was examined rather than continuous current as done in previous models in order to try to predict the transient stress drop caused by the onset of electric current. The simulation was conducted up until the onset of necking, at which point the simulation was stopped to allow for a simpler prediction. Temperature dependent material properties were modeled using a Ludwick model.

Hariharan's model is in good agreement with experimental results at isothermal room temperature. However, an elevated temperature isothermal test was not used to validate its ability to properly predict elevated temperature flow stress. When the first simulation was run, it was noted that the temperature prediction was higher than experimental observation. Therefore, a constant correction factor of 0.6 was placed on the model to allow for more accurate temperature prediction [54]. This factor can be thought of as similar to the EEC coefficient created by Bunget *et al.* and Salandro *et al.* [30; 64], and would describe that only a portion of electricity goes into Joule heating. It is found that the stress is accurately predicted, though thermal softening is not completely captured. This was attributed by the authors as the effect of precipitate growth in the aluminum due to elevated temperature. Once again, the stress drop is not predicted accurately. It was concluded that a portion of the stress drop was caused by thermal expansion, but the thermal expansion effect lessened as test time increased. As such, there is still no true understanding or way to predict transient flow stress drop caused by electrical pulses. It was concluded that Joule heating accounted for around 60% of the electroplastic effect. A

similar coupled thermal-electrical-mechanical model was constructed for AZ31B magnesium, a Joule heat fraction of 1 was used, meaning all of the electricity was converted to heat, it was found that the stress drop was still unpredictable, though this model assumed all electrical energy went into heat [65].

Molotskii and Fleurov took a different approach to predict the electroplastic effect that does not rely on Joule heating. Rather, they mathematically examined magnetic effects as a way to explain the electroplastic effect in metals [56]. An electric current induces a magnetic field, resulting in increased dislocation depinning by converting singlet (S) states to triplet (T) states, noting that depinning in T states is much easier than S states [56]. It is assumed that the main mechanism of the electroplastic effect is the changing of obstacle spacing in a cylindrical specimen resulting in easier deformation motion through depinning from the triplet state. No direct experimental comparison is presented from the authors of the paper. A detailed review of magnetoplasticity can be found in Golovin's work [58].

Thermal Softening View

Magargee *et al.* took a different approach to comparing isothermal testing and electrical testing and also modeled flow stress in a quasi-steady state tensile process [9]. Rather than heating the specimen to match the electrical effect, the electrical specimen was cooled to room temperature using forced air convection on a thin specimen of Grade 2 titanium to compare with room temperature non-electrical tests. The deformation was not started until the specimen reached steady state temperature. It was found that the air cooled test had the same flow stress as the baseline test with no electricity; however, without air cooling, a large flow stress drop was observed. Meaning that the electroplastic effect did

not exist without a rise in temperature. Goldman *et al.* previously found similar results in tension when cooling lead to a 4.2K superconducting state [66]. It was found that when there was not a significant temperature rise from Joule heating there was no flow stress reduction. If the temperature rise from Joule heating was high enough to cause the material to leave a superconducting state then there were significant flow stress reductions. Similar results were found by Jordan and Kinsey during pulsed micro bending of C260 brass and found that force reductions only occurred during temperature spikes for 3 different grain sizes [67].

Margaree *et al.* used two different material models to predict flow stress, both assuming that only Joule heating is present from the electric current but applied to a steady state where the temperature of the specimen did not change [9]. The first model used is a modified power law or Hollomon model that had a temperature dependent strength coefficient. The second model examined is a modified Johnson-Cook model with an empirical exponential softening parameter. Johnson-Cook uses similar terms as the Hollomon model but includes strain rate sensitivity and temperature sensitivity terms that act as multipliers on the power law model. The results from these models are in good agreement. The Johnson-Cook is a higher degree-of-freedom model, and is paired with a softening parameter to allow for modification of the resulting flow stress curve based on temperature. The model was applied to Grade 2 titanium in compression using data from [30], and material model parameters were determined using least squared regression fitting to baseline (no electricity) data. It was shown that the model was somewhat in agreement with experimental data, though the curve shapes are incorrect in the presence of electricity.

The flow stress in tension was predictable using only temperature-based simulation assuming homogenous heating without the inclusion of additional electroplastic effects. The drawback with this model is only applied to quasi-steady state tension of thin foils where temperature does not change and is known. Similar results were found by Wang *et al.* who extended upon Magargee's model using 1D heat transfer to predict temperature and a 5-factor influenced stress model (thermal softening, strain hardening, rate hardening, solute-dislocation interaction, and electron-dislocation interaction) for AZ31 Magnesium [9; 68]. It was found that Joule heating and thermal softening was the dominate stress reduction mechanism; however this only applies at quasi-steady state timing where the temperature does not change even though electricity is flowing.

Zheng *et al.* conducted similar works to Magargee, using quasi-steady state electrical application, except that the effect of strain was tested and modeled [12]. Zheng *et al.* tested pure titanium foils that were 0.05 mm thick. As expected, higher strain rate resulted in higher flow stress but lower ductility, and increased temperature resulted in lower flow stress. Zheng *et al.* used a simple energy balance to calculate temperature of the specimens to validate the experimental results. A Fields-Bachofen model of flow stress was chosen by the authors for stress prediction, due to its ability to compensate for strain rate through an added strain rate sensitivity term of $\dot{\epsilon}^m$ to the existing power law model. The material model parameters were found experimentally for each temperature. Since these parameters correspond to a known current density used to produce the temperature, it was possible to find the model parameters as functions of current density rather than functions of temperature. This allowed for modeling flow stress as a function of current

density without the need for temperature prediction after the parameter curves are found; this is the first model not to require temperature for every calculation. The model is accurate for all strain rates tested in quasi-steady state electrically-assisted tension of thin foils. However, this model can only be applied to thin titanium foils. Additionally, the operation must be quasi-steady state with steady temperature.

Grain size effects were studied by Siopis and Kinsey in C101 Copper and by Fan *et al.* in C260 brass, respectively [14; 69]. Siopis and Kinsey conducted compression testing in the presence of electricity with three different grain sizes (164, 43, 9 μm). It was found that stress reduction was greater in specimens with smaller grains when compared to a baseline test of the same grain size, and that the threshold density increased as the grain size increased, suggesting that threshold current density may be linked to grain size or the number of grain boundaries in a specimen. This could support the microscale Joule heating effect, as more grain boundaries would result in a greater area dislocation stacking leading to greater dislocation density and resistivity. As shown by Nabarro in his book, *The Theory of Crystal Dislocations*, various material factors can contribute to metallic resistivity, through the model shown in Equation 2 [49], where ρ_e is the total resistivity of the metal and ρ_t is the thermal resistivity of the metal caused by lattice vibrations due to increased temperature and thermal energy. The concentration coefficients c_v, c_I, c_d, c_s represent voids, interstitials, dislocation density, and stacking fault area density, respectively. $P_v, P_I, P_d,$ and P_s are material constants that have the dimensions of $\Omega\text{-cm}, \Omega\text{-cm}^4, \Omega\text{-cm}^3,$ and $\Omega\text{-cm}^2$ respectively. This model can be interpreted to support microscale Joule heating since the resistivity will be higher with greater stacking fault and dislocation densities,

which will appear in higher densities near grain boundaries. This model fails to account for lattice misalignment based resistivity differences which may dominate near grain boundaries.

$$\rho_e = \rho_t + P_v c_v + P_I c_I + P_d c_d + P_s c_s \quad (2)$$

Kinsey *et al.* examined the effect of electricity on tensile tests conducted at high strain rate (*i.e.*, over 1000/s) [70]. 304 stainless steel and Grade 5 titanium were both tested using a Kolsky bar experiment setup to provide high strain rate. Therein, it was found that at high strain rate, even at current densities higher than what would be used for quasi-static testing (*i.e.*, over 50 A/mm²), there was little effect. The slight difference observed in stress was attributed to a small temperature rise during the testing (*i.e.*, 50 °C for steel, 235 °C for titanium). As such, it was concluded that Joule heating was able to account for the small flow stress differences during high strain rate tension, and as such, the electroplastic effect was absent at these rates.

Kang *et al.* were the first to look at *in situ* dislocation motion in the presence of an electric current, through the use of a transmission electron microscope (TEM) with nano-tensile specimens [71]. Single crystal copper tensile specimens with gauge area dimensions 10 μm length, 10 μm width, and 100 nm thickness, were set into a fixture with dimensions of 5x1.5 mm. It was shown through both analytical and numerical simulation that due to the specimen to fixture size ratio, there would be no significant temperature rise (max 0.2°C) up to a current density of 5000 A/mm². As such, Joule heating was eliminated in this testing. Dislocation motion is monitored using bright field images during the electrically-assisted tensile process. It was concluded that with current densities up to 5000

A/mm², there was no dislocation mobility change in the presence of electric current, nor was there dislocation depinning caused by a magnetic field from the applied electric current. This work continues to disprove the electron wind in an experimental sense to add to Molotskii's and Molotskii and Fleurov's theoretical disproof [56; 72]. It also disproves Molotskii's and Molotskii and Fleurov's dislocation depinning theory, at least at the nanoscale [56; 72]. Further investigation is required to determine if the same lack of transport mechanisms will be present in macro-scale specimens. Similar results were found by Kim *et al.* in AZ31 Magnesium [73].

Conclusions

This background section has elucidated the current understanding, theories, and modeling of the electroplastic effect on metallic materials. There are four dominant theories: electron wind [39-47; 74], Joule heating [43; 51-55], magnetoplasticity [56; 72], and dissolution of metallic bonds [48]. Most experimental data and models attempt to separate Joule heating from other effects to determine if the electroplastic effect is more than thermal softening due to temperature rise from Joule heating. As such, two viewpoints developed, the *Thermal Softening viewpoint* where the electroplastic effect was assumed/shown to be Joule heating, and the *Electroplastic Effect viewpoint* where the electroplastic effect was assumed/shown to be caused by more than thermal softening from temperature rise due to Joule heating, this includes the electron wind, dissolution of bonds, and magnetoplasticity.

The *Electroplastic Effect viewpoint* argument is supported by:

- Electrically-assisted tension and compression have greater flow stress reduction than isothermal testing done at the same temperature [11; 14; 24; 59-62].
- Modeling demonstrating that Joule heating accounted for 40-70% of the electroplastic effect [43; 51-55].
- Specimens with greater cold work exhibit lower flow stresses without a large temperature difference [69].
- FEA models have been unable to predict stress drop during transient pulsed electric current tension testing [7; 54; 65].
 - Many of these models require a Joule heat fraction or Electroplastic Effect Coefficient (EEC) in order to predict the correct temperature. This means that only a portion of the electricity goes into heating.

The *Thermal Softening viewpoint* argument is supported by:

- Air cooled electrically-assisted tension tests at room temperature showed the same flow stress as a specimen without electricity [9].
- At steady state, the flow stress in tension and compression can be fully predicted by assuming 100% Joule heating from electricity (no heat fraction/EEC) [9; 12].
- Electricity had no effect on flow stress during high strain tensile testing (strain rate $>1000 \text{ s}^{-1}$). The temperature rise from electricity was low [70].
- Mathematical disproving of electron wind theory, stating it is not possible for the electron wind to transfer enough momentum to cause a noticeable plasticity difference in flow stress [56].

- *In situ* electrically-assisted tension testing under TEM found that for a single grain copper with current densities up to 5000 A/mm², there was no dislocation motion difference [71; 73]. Temperature rise was eliminated using heat sinking fixtures; however, the electron wind and magnetoplasticity theory did not require elevated temperature for an effect, which was shown to be absent due to no difference in dislocation motion.

From the literature review presented herein, it is likely that the electroplastic effect in metallic materials is caused by Joule heating. *In situ* TEM of a single grain copper has shown that there is no dislocation motion differences from a magnetic field (magnetoplasticity) or from electron collision based momentum transfer (electron wind) [71; 73]. It is also shown that the electroplastic effect on flow stress can be fully predicted at the steady state using a 100% Joule heating assumption [9; 12]. This means that the main unpredictable portion of the electroplastic effect is the stress drop caused by the onset of electric current. However, this could be explained using microscale Joule heating at flaws such as grain boundaries or micro-cracks within the metal. Grain boundaries will have an increased dislocation density as strain increases which in turn will increase the resistivity of the grain boundaries leading to increased Joule heating and hot spots at these locations as shown by grain boundary welding in [14; 49]. Micro-cracks will result in increased current densities on each side of the crack, or if the voltage is high enough, the electricity could jump the air gap of the crack resulting in arcing/welding.

CHAPTER THREE

3. BACKGROUND ON METALLIC MATERIAL SCIENCE AND ALUMINUMS

Metallic Bonds

Metal crystalline structures are formed by metallic bonds. This type of bonding utilizes group sharing of valence electrons between positively charged ion cores. The electrons are free to move around the ion cores in an electron cloud. The arrangement of the ion cores determines the crystal structure of the metal. There are 3 crystal types for metals: face centered cubic (FCC), body centered cubic (BCC), and hexagonal close packed (HCP) [75]. The primary metal in this research is aluminum, which has an FCC structure; the steel used in the drilling research has a BCC structure. There are possible defects within a crystal lattice, including point and line defects [76].

Metallic Lattice Defects

Point defects can be either intrinsic or extrinsic. Intrinsic defects can exist in a perfect lattice, and are caused by vacancies or interstitials in the lattice. Extrinsic are caused by alloying elements or impurities. A lattice vacancy occurs when one of the ion cores in the lattice is missing, which leaves a blank spot. An interstitial is an atom in a position that it would not normally occupy; this is shown in Figure 3-1. Vacancies are common in crystalline materials and allow for diffusion to take place at a low energy state. Interstitials are less common and force the matrix to a higher energy level. Extrinsic defects are caused by solutes (alloying elements added on purpose) and impurities (elements that are not meant to be in the metal). Foreign atoms may take a vacant spot; in this case it is called a substitutional atom. Interstitial impurities also occur but are restricted to smaller atoms

than the lattice atoms in order to avoid breaking the lattice structure. Solute atoms typically result in a mechanical strengthening; this is called solid solution hardening. The solute atom in substitution is typically smaller or larger than the base metal's atoms, which results in a distorted lattice that will impede the movement of dislocations.

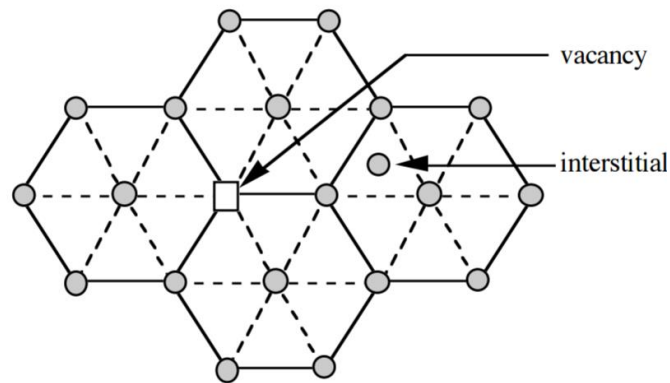


Figure 3-1: Vacancies and interstitials in a metallic lattice

Linear defects contains different types of dislocations: edge, screw, and a combination of edge and screw [76]. Dislocations influence yield strength and flow stress during deformation and can also factor into crystal growth and electrical properties. An edge dislocation occurs when the part of the lattice is shifted resulting in atoms sliding over top of each other along a slip plane, shown in Figure 3-2. Screw dislocations unlike edge dislocations are not a simple slip where an entire portion of the lattice is shifted. A screw dislocation shifts only a portion of the lattice, as shown in Figure 3-3.

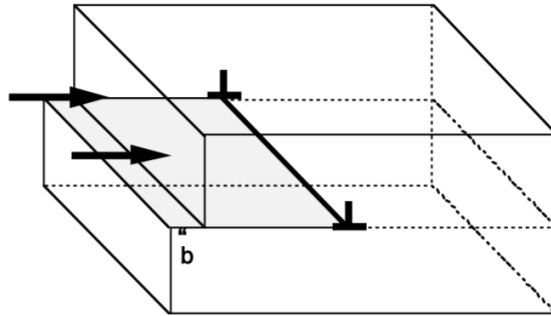


Figure 3-2: Edge dislocation visualization [76]

Screw dislocations unlike edge dislocations are not a simple slip where an entire portion of the lattice is shifted. A screw dislocation shifts only a portion of the lattice, as shown in Figure 3-3.

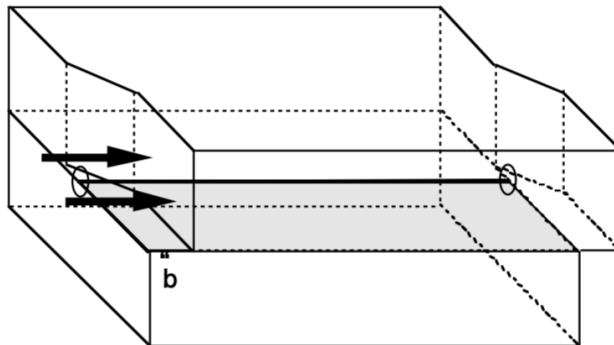


Figure 3-3: Screw dislocation visualization [76]

Metal Crystal Plasticity and Dislocation Modeling

Plasticity in crystallographic metals is caused by dislocation motion along shear planes. Elastic deformation is simply a stretching of metallic bonds that does not cause dislocations. For this reason, there is no permanent deformation and the metal will return to its original shape when the load is removed. The dislocation motion is caused by mechanical shearing from an external force. As such, all metallic failures, even in tension are caused by shear forces. Dislocation motion and slip occur along slip planes with a slip

direction. The total number of slip planes is known as a slip system. Slip will occur along the closed packed planes, which are the planes of the crystal that have the most atoms per area [75]. The crystallographic planes are labeled by Miller indices [77] using a unit cube and a coordinate set for FCC and BCC structures, or a hexagon and 4 sets of coordinates for HCP structures. The planes are shown in Figure 3-4 for FCC. FCC structures will slip along the $\{111\}$ plane in the $\langle 110 \rangle$ direction [78].

The Burger's vector represents the difference between a distorted and undistorted lattice when the distortion is caused by a dislocation [79]. It represents the magnitude and direction of the atomic displacement which occurs when the dislocation moves. The magnitude of the Burger's vector (b) for FCC and BCC crystal structures is shown in Equation 3, where h , k , and l are coordinates of the slip direction $\langle 110 \rangle$ for FCC, and a is the edge length of the unit cell [75]. FCC structures have 4 atoms per unit cell and Aluminum has a density of 2.7 g/cm^3 . The density is divided by the molar mass of aluminum (26.981 g/mol) to get the number of moles/ cm^3 . This yields 0.1 mol/cm^3 . This is then multiplied by Avogadro's number (6.022×10^{23}) to get the number of atoms, this yields $6.022 \times 10^{22} \text{ atoms/cm}^3$. Dividing this number by 4 gives $1.51 \times 10^{22} \text{ unit cells/cm}^3$. Taking the reciprocal of this gives $6.64 \times 10^{-23} \text{ cm}^3/\text{unit cells}$. Taking the cube root of this will yield $4.05 \times 10^{-10} \text{ m}$ which is the edge length in meters.

$$||b|| = a\sqrt{h^2 + k^2 + l^2} \quad (m) \quad (3)$$

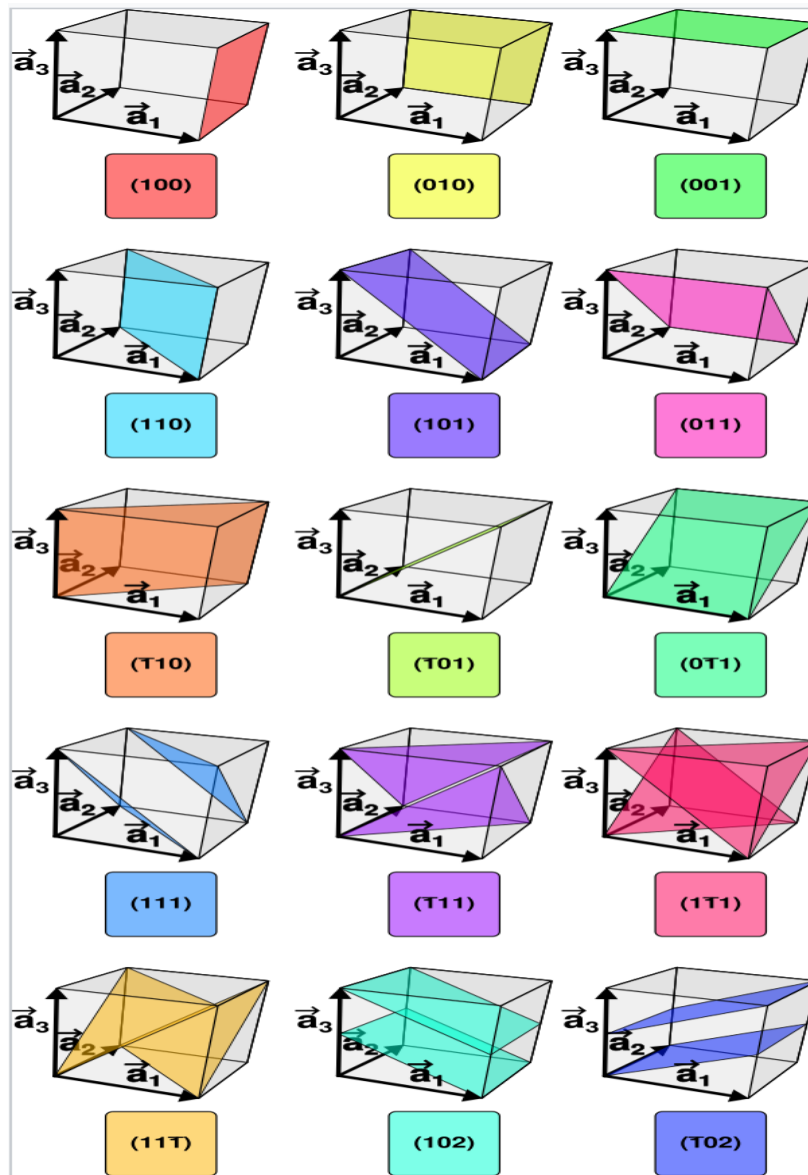


Figure 3-4: Crystal Slip Planes in FCC

In order for slip to initiate, a critical resolved shear stress (CRSS) must be achieved [75; 80]. CRSS is the shear stress in the slip direction that is needed to cause a lattice in a grain to slip. This value is constant for crystal families. The Resolved Shear Stress (RSS) can be calculated using Equation 4, where σ is the applied tensile stress, λ is the angle between slip direction and loading, and θ is the angle between the slip plane and loading.

$$RSS = \sigma * \max(\cos\theta, \cos\lambda) \quad (4)$$

A simple relationship between flow stress and dislocation density is shown in Equation 5, where σ is the flow stress, b is the magnitude of the Berger's vector, ρ_d is the dislocation density, α is the thermal activation constant, and μ is the shear modulus [81]. This equation is accurate only when flow stress can be assumed dominated by dislocations interacting with each other, this will only be true for a pure FCC metal. A slight modification was made to this equation to include an average Taylor factor (M), shown in Equation 6. For aluminum, M is assumed to be 3 and α is assumed to be 1/3 at room temperature [82], as such these cancel out resulting in Equation 7. Due to thermal activation of dislocation motion and creation, α will depend on temperature.

$$\rho_d = \left(\frac{\sigma}{\alpha\mu b} \right)^2 \quad (5)$$

$$\rho_d = \left(\frac{\sigma}{M\alpha\mu b} \right)^2 \quad (6)$$

$$\rho_d = \left(\frac{\sigma}{\mu b} \right)^2 \quad (7)$$

Most dislocation density models are used to find dislocation density and then flow stress. However, it has been shown that stress models such as the Johnson-Cook model are able to accurately predict flow stress up until the transient stress drop. To address this, Equation 7 will be solved to get dislocation density based on the flow stress found from the Johnson-Cook model.

Aluminum Alloys and Strengthening Mechanisms

Aluminum and its alloys are metals where the dominant element in the metal is aluminum. Alloying elements include copper, magnesium, manganese, silicon, tin, and zinc. Aluminums fall into two categories: cast and wrought. From those two categories they are further classified into heat-treatable and non-heat-treatable [83]. Wrought alloys are aluminums that are cast and then further processed into their final shape, this could include rolling, extrusion, or forging. Cast alloys are cast directly to their final shape, and are cheaper than wrought alloys but can have lower strength due to casting porosity.

Aluminum is heavily used in the aerospace industry and is gaining attention in the automotive industry due to its good strength to weight ratio, which is better than conventional steels. Aluminum will also not corrode as easily as steel, as aluminum oxidizes quickly, forming an aluminum-oxide layer which will prevent further corrosion [84]. However, aluminum can still degrade through galvanic corrosion, an effect caused by two metals with different electro-negativity coming into contact with each other. Also known as dissimilar metal corrosion, this phenomena presents a problem in the automotive industry because steel and aluminum have opposite electro-negativities and will corrode each other quickly if in contact; this is typically addressed using adhesives to separate the metals. Finally, if heat treated improperly, element segregation can cause the aluminum to corrode from the inside out due to elemental imbalances.

When compared to steel for the automotive industry, there are advantages and disadvantages of using aluminum, listed below:

Advantages:

- Better strength to weight ratio for closures

- Less likely to corrode when exposed to air and water
- Can be higher strength than forming steels

Disadvantages:

- Lower elastic modulus (70 GPa versus 200 GPa for steel), this leads to increased springback in stamping
- Cars are still mostly steel, galvanic corrosion must be addressed
- Aluminum is difficult to weld (high thermal and electrical conductivity)
- No infinite life stress value in fatigue (steel has an infinite life value)
- Will not glow before melting, difficult to work with for repair shops if heating is necessary
- High temperature sensitivity, this metal cannot be used for combustion chambers in engines

The commonly seen treatments appended to the name of an aluminum are listed below; examples include 5052-H2 or 7075-T6 where H2 and T6 are the treatments [85; 86].

- 0- fully annealed, softest state
- H- strained and possibly heated
 - H1- strain hardened no heating
 - H2- strain hardened and partially annealed
 - H3- strain hardened and low temperature heating
- T: Heat treated for a temper
- T1: Cooled from hot working then aged at room temperature

- T2: Cooled from hot working, then cold worked, then aged
- T3: Solution heat treatment then cold worked
- T4: Solution treated then naturally aged
- T5: Cooled from hot working, then aged at elevated temperature
- T6: Solution treated then artificially aged
- T7: Solution treated then stabilized
- W: solution heat treatment only

The names of the aluminum families indicate the alloying elements and possible hardening mechanisms, listed below by series [86]:

- 1000: Pure aluminum
- 2000: alloyed with copper and precipitation hardened
- 3000: alloyed with manganese
- 4000: alloyed with silicon
- 5000: alloyed with magnesium
- 6000: alloyed with magnesium and silicon (6061 is the most commonly used aluminum alloy)
- 7000: alloyed with zinc, these are the highest strength aluminums
- 8000: alloyed with other elements not listed in 1000-7000

Cast alloys are indicated by “AA” in front of a 3-digit sequence. The first digit indicates the alloy, nominally following the same first digit as the wrought alloys above (except for 300 series, which has silicon, copper and magnesium, and 800 series where tin

is alloyed). An example, AA356 is a cast aluminum alloy that has silicon, copper, and magnesium.

The strengthening mechanisms of aluminum include: work hardening, solid-solution hardening, fine grain hardening, and aging [87-89].

Work hardening is the same as strain hardening or cold working; the part is strained which in turn will increase the strength of the metal and decreases its ductility. This is caused by dislocation pileup at grain boundaries making further dislocation motion difficult.

Fine grain hardening is done using grain refinement to decrease the size of grains in the part; this in turn increases the length of grain boundaries in parts. This will accelerate strain hardening since there are more barriers to block dislocation motion and to cause dislocation pileups.

Solution treatment/homogenization heats aluminum to a temperature between 460-560°C in order to cause the alloying elements to re-dissolve into the metal to form a solid solution with a homogenized distribution of alloying elements. After casting, the alloying elements are usually precipitated out during solidification and are non-uniformly distributed in the metal.

Aging is one of the most common methods for strengthening aluminum. At high temperature, alloying elements are dissolved homogeneously in a solid solution, which is accomplished through solution treatment. If the temperature is then reduced, the alloying elements that have not yet dissolved and stabilized are unable to precipitate out of solid solution, causing the solid solution to be super-saturated with alloying elements since they

have not precipitated out. Aging can be done at room temperature or a slightly elevated temperature, and will allow the alloying element to precipitate out. The precipitates in turn will block slip systems and dislocation motion leading to elevated strength. This is typically done by solution treatment followed by a quench and then either a natural aging (room temperature) or an artificial aging (elevated temperature). The solution treatment forces the precipitates into a solid solution at elevated temperature; the quenching then freezes the solid solution at a supersaturated point to allow for aging to precipitate out the alloying elements.

7075 is an aluminum alloy that contains zinc, as stated above. It has good fatigue strength but average machinability and is more likely to corrode than other aluminum alloys. It is more expensive than most aluminum alloys. 7075 is a heat treatable alloy, and its properties are heavily dependent on heat treatment [90-92].

- 7075-0 is annealed and is the weakest form of 7075 but is corrosion resistant and has a ductility of 9-10%, and a tensile strength of no more than 280 MPa. This is accomplished by holding the aluminum at 412°C for 3 hours and then decreasing the temperature of the furnace by 10°C until a temperature of 260°C at which point it is air cooled [93].
- 7075-T6 is the alloy used in this research. It has a tensile strength up to 540 MPa and an elongation between 5-11%. The higher strength in the T6 condition offers strength much higher than the annealed alloy but at a similar ductility. This temper is achieved by homogenizing cast 7075 at 450°C for several hours. The alloy is then quenched and aged at 120°C for 24 hours [88]. This results in finely dispersed precipitates within the

grains and grain boundaries. If reheated, the precipitates will continue to grow and will result in overaging and a weakening of the alloy.

- 7075-T7 has a tensile strength of 505 MPa and a ductility of 13%. This is accomplished by overaging the alloy by aging at 120°C for several hours, then heating at 160°C for 24 hours. The precipitates are larger than those of T6 but results in an alloy that is less likely to stress crack.
- 7075-RRA (Retrogression and re-age). This treatment is done to re-age the alloy to return it to T6 strength. This is done by overaging, and then heating the part at 120°C for 24 hours. However, this can be done at different temperatures between 180-240°C for 15 minutes. Higher temperatures will reduce the aging time drastically, and likely lead to overaging.

CHAPTER FOUR

4. EVALUATION OF THE MICROSCALE JOULE HEATING THEORY

This section provides an initial evaluation of the current work in electroplastic theory as it relates to the validity of the four theories explained in Chapter 2. Next, the microscale Joule heating theory is evaluated using Finite Element Analysis.

Evaluation of Recent Studies in Electroplastic Theory

The section examines existing theories for the transient electroplastic effect through examination of current works in the literature. It is known that a portion of the stress drop is caused by thermal expansion and thermal softening due to the bulk temperature rise from Joule heating, but the remaining mechanism(s) for accurately predicting the stress drop remain unknown to this date.

The Electron Wind Theory

The electron wind theory is often dismissed as the potential cause for the electroplastic effect, as multiple mathematical models have shown that the electron wind force is orders of magnitude too low to account for stress reductions from an applied electric current coupled with *in situ* electrically-assisted dislocation motion observation studies [7; 56; 71; 94]. However, the electron wind itself is a well-documented phenomenon arising from the study of electromigration (EM). EM is atomic diffusion driven by an electric field as current passes through a metal, and is heavily studied as a potential failure mechanism for thin film connectors in circuits [95]. Over a long period of time, the electron-driven diffusion leads to fracture of thin film electronic connectors. The driving mechanism behind EM is the electron wind, where collisions of electrons with ion cores result in mass diffusion towards the grounded side of the metal [96]. Over a long

period of time, this leads to thinning and fracturing of the metal towards the side where electricity was applied. It is known that the electron wind in EM is magnified at grain boundaries due to increased obstacles and electron scattering from collisions. However, due to the long time scale required for EM, it is unlikely that the electron wind is solely responsible for the transient stress drop from the electroplastic effect.

The Magnetoplasticity Theory

The magnetoplasticity theory, as proposed by Molotskii *et al.* to explain the electroplastic effect, stems from the field of electromagnetic forming [56; 72]. Electromagnetic forming is a high rate forming technology that uses pulsed magnetic fields to apply forming loads to materials with high electrical conductivity [97]. This is done by applying a pulsed current with frequency ranging from 5-100kHz to a metal coil placed near the workpiece to be formed.

The magnetoplasticity theory has not been supported in the EAM research community, as electromagnetic forming requires coils of wires with pulsed current in the kHz range. Most electrically-assisted forming papers do not use coils of wire and the pulse frequency is much lower than electromagnetic forming, suggesting that magnetoplasticity cannot be solely responsible for the electroplastic effect given the current pulse frequency and lack of coiled wires.

The Dissolution of Bonds Theory

The dissolution of metallic bond theory can be understood as the electrical flow brought on by an applied current pushing extra electrons into the lattice and saturating the electron cloud, which allows for reduced sharing between ion cores and subsequent

improved ion core mobility within the electron cloud. In theory, if the current density is high enough, it may be possible to completely dissolve the bonds of the metal. The dissolution of bonds theory remains untested and still has the potential to explain the electroplastic effect.

A Note on In-Situ TEM Studies

Recent *in-situ* observation of dislocation motion in an electrically-assisted tensile test under a Transmission Electron Microscope (TEM) has shown that there is no significant change to dislocation motion in single crystal copper (SCC) [71] and 5052 aluminum [94]. However, in the case of single crystal copper (SCC), the strain was held constant (no deformation) during the electrical pulse while dislocations were studied on the [1 1 0] zone axis [71]. The electron wind and magnetoplasticity theories as applied to deformation mechanics rely on dislocation motion assistance to overcome obstacles through electron collision based momentum transfer, meaning that this theory is not tested in the TEM studies since deformation (dislocation motion) is stopped during the electrical pulse. Instead, this TEM study shows that electromigration does not exist during short duration electrical pulses.

In the pure SCC, the only obstacle was other dislocations as the SCC is free of precipitates and grain boundaries. In the case of 5052 aluminum, the zone axis and whether or not the TEM images were taken at a grain boundary or near an obstacle is not given [94]. Both papers fail to address whether the direction of electric current parallels the primary deformation zone axis, which may lead to differences in observed electron-dislocation interaction. The thickness of TEM specimens (typically near 100nm) leads to some

uncertainty on results from *in situ* TEM studies. The resultant surface area to thickness ratio may cause a significant skin effect from the electric current, where most of the current runs along the outer edges of the parts rather than through the thickness, resulting in the observation of a non-existent electron-dislocation interaction. The thickness of the specimen also results in a planarized deformation mechanic where dislocations are generated in 2D rather than 3D, resulting in altered dislocation dynamics through the planarization of obstacles.

Taking a TEM picture requires exposure time for the camera to process the current electron image; longer exposure times typically correlate to higher quality images. However, this presents a problem if true *in situ* dislocation observation during an electrically-assisted deformation process is to be observed. If dislocations are continuously moving while a picture is attempted, the exposure time of the camera becomes a problem for imaging as the image is continually changing throughout the exposure time of the camera due to dislocation motion.

Experimental Setup

To determine if the electroplastic effect is predictable in pulsed tension of 7075-T6 aluminum, the following experiment is conducted and modeled using the state of the art model. It is expected that the current state of the art model (bulk model) will not be able to predict the transient stress drop.

7075-T6 specimens are cut from a single sheet of 1-mm thick aluminum to ASTM E8 standards. The specimens are painted black in the gauge length on the front side to allow temperature measurement from a FLIR A40M thermal camera used at a sampling

rate of 6.5 Hz with a resolution of 0.1 °C. Figure 4-1 shows a schematic of the testing setup.

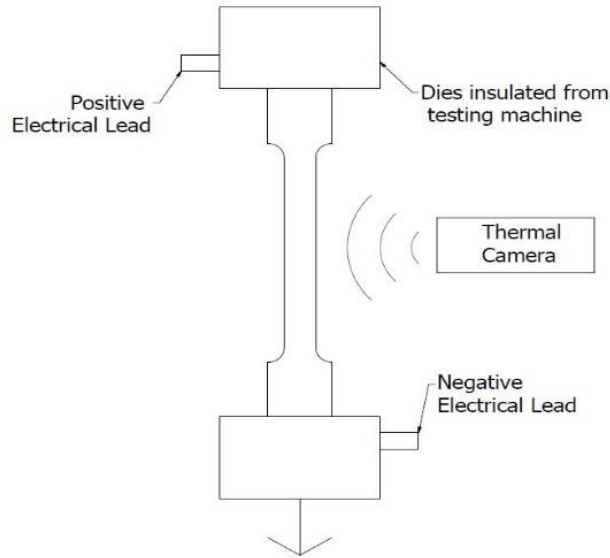


Figure 4-1: Experimental setup for electrically-assisted tension

The specimens were deformed on an Instron 1332 servo-hydraulic machine parallel to the roll direction at a platen velocity of 2.5 mm/min until fracture. Electricity was applied from a Darrah 4-kA power supply controlled by LabVIEW software. Square wave current application was applied with a nominal current density of $60\text{A}/\text{mm}^2$ with a pulse duration of 1 or 3 seconds with a pulse period of 60 seconds. 3 replications of each test were conducted to ensure repeatability of the data presented. The flow stress and temperature results are shown in Figure 4-2. For comparison with the model described in the following, only the 1-second duration pulse is used. The 3-second duration pulse resulted in overaging, visible since the flow stress did not approach the room temperature stress curve following the first electrical pulse, even though the temperature had returned

to room temperature. This would present problems with the Johnson-Cook material model, because it cannot account for over-aging based softening.

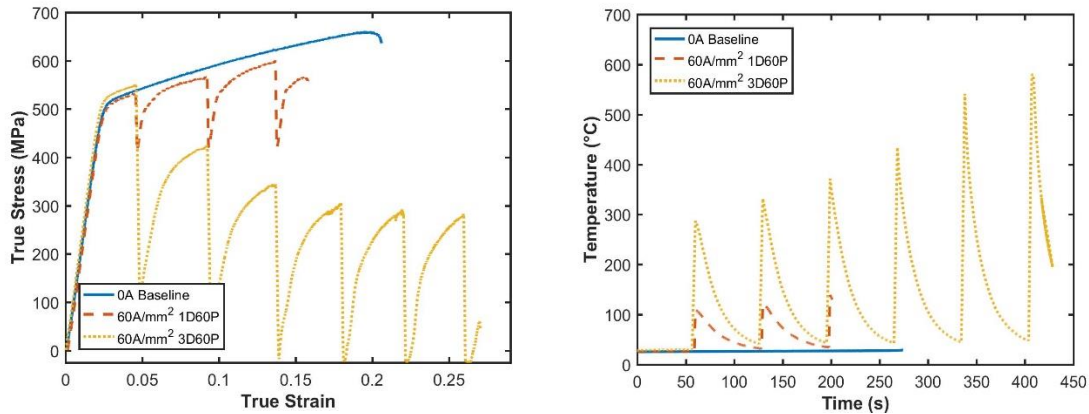


Figure 4-2: Stress and temperature results compared to 0A baseline for 60 second period square wave forms

Literature Based Bulk Joule Heating Model

The current state of the art model from the literature (bulk model) is recreated to ensure that the stress drop observed in Figure 4-2 cannot be predicted. A half-symmetry model of an ASTM E8 dogbone specimen was created with a thickness of 1mm in ABAQUS 6.14. The model setup is shown in Figure 4-3, and is described below:

- The model was meshed with Q3D8 thermal-structural-electrical brick elements with 5 elements through the thickness.
- The gripped region was held at constant ambient temperature, due to high thermal conductivity of aluminum inside of large steel grips.
- The exposed region was subject to both convection and radiation with a combined coefficient of 22.5W/m²K.
- The left clamped region was fully fixed.

- The right clamped region could only move in the axial direction.
- The right clamped region was given a velocity of 2.5mm/min.
- Electricity was applied to the left side and grounded at the right side of the specimen to give a nominal current density of 60A/mm² in the gage region.
- The solution increment was set to 0.1s.
- The Johnson-Cook plasticity model was used for flow stress calculation.
- A symmetry condition was applied at the center of the specimen in the length direction.

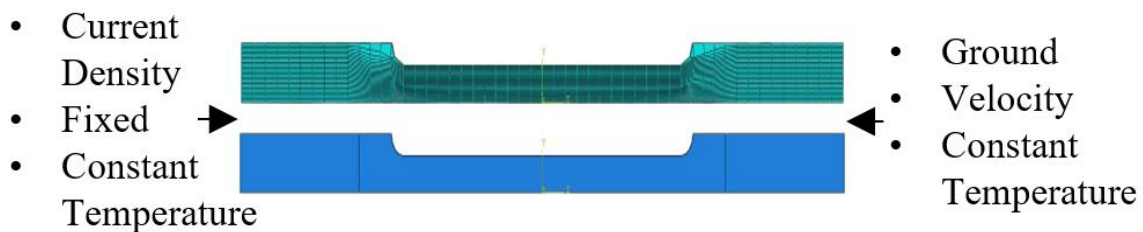


Figure 4-3: Model setup, boundary conditions applied at the outer partitioned regions

This model was used without electricity to evaluate the Johnson-Cook parameters for 7075-T6 found in [98]. For elevated temperature, the specimen was given a uniform and constant temperature boundary condition.

Johnson-Cook Parameter Evaluation

The Johnson-Cook model is composed of 3 terms; the full equation is given in Eq. 8. The first term represents the flow stress of a metal in quasi-static uniaxial tension. The second term represents the strain rate effects, which will be absent in this model since all testing is done at the quasi-static rate. The final term is temperature sensitivity, which is important to study the Joule heating theory due to the resultant temperature rise. The

parameters A , B , and n were validated using a room temperature tensile test, with the results shown in Figure 4-4. To check parameter m , elevated temperature tensile tests were conducted by an outside lab at 150°C (highest temperature reached during the electrically-assisted experiments), the resulting stress-strain curve is shown in Figure 4-4. The elevated temperature test model loses accuracy past 15% strain; however, the electrically pulsed tensile specimens typically break near this strain. The parameters used in the Johnson-Cook model are shown in Table 4-1. The yield stress, A , was slightly modified to 500MPa from 546MPa to match experiment.

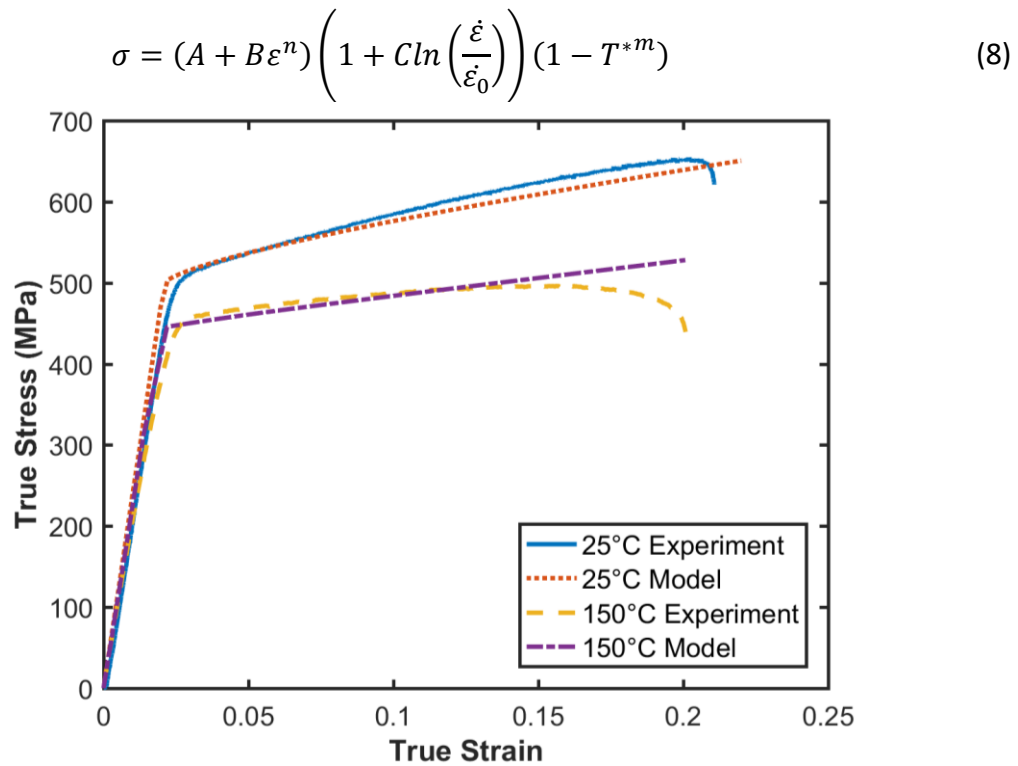


Figure 4-4: Isothermal model vs. experiment at room and elevated temperature

Table 4-1: Johnson-Cook plasticity model for 7075-T6 Aluminum [98]

A (MPa)	B (MPa)	n	m
500	678	0.71	1.56

Electrically Pulsed Bulk Model

The bulk model predicts the correct temperature as shown in Figure 4-5, but cannot predict the correct stress during the electrical pulse. The predicted stress was higher than experiment, which matches the findings of Jones *et al.* and Hariharan *et al.* [7; 54]. It is known that the transient stress drop is composed of thermal softening, thermal expansion from Joule heating, as well as a contested additional effect (see theories in the background section).

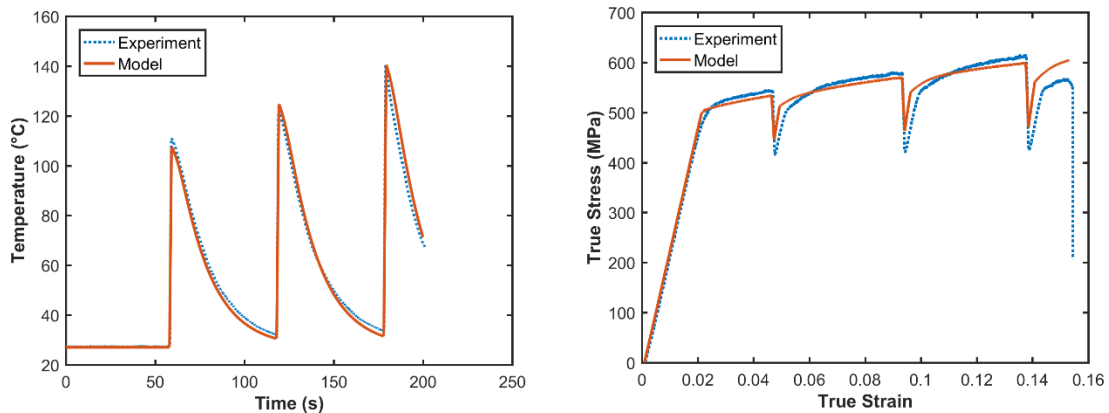


Figure 4-5: Bulk model vs experiment, temperature and stress result, note that the model cannot predict the correct stress drop even with the correct temperature

This dissertation hypothesizes that the remaining effect is a microscale phenomenon of thermal expansion and thermal softening, known as the *Heterogeneous Joule Heating* theory. In other words, since dislocations stack up at grain boundaries, the resistivity of the metal will be increased in these zones. Therefore, higher power dissipation

for a fixed current will raise local temperatures and induce greater softening and localized expansion, resulting in an increased stress drop. In order to investigate this theory, the electrical resistivity was modeled as a function of dislocation density and temperature. The dislocation density was based on axial stress which will cause a heterogeneous resistivity field prior to an electrical pulse. During the electrical pulse, while areas of higher electrical resistivity heat and soften more than others the electrical resistivity field will gain a larger spatial variance as hotter zones will continue to increase in resistivity linearly with temperature creating larger resistivity gradients across the specimen.

Electrical resistivity was modeled as a function of temperature and dislocation density, this model roughly represents a single crystal material without grain boundaries as a source for dislocation stacking, meaning the dislocation density in this model was lower than a model with grain boundaries.

It has been shown that electrical resistivity is composed of three main mechanisms: temperature or thermal resistivity, dislocation density based resistivity, and stacking fault area based resistivity [49]. This work examines dislocation density and thermal based electrical resistivity such that the total resistivity of each element was found using Eq. 9, where ρ_e is the total electrical resistivity, ρ_t is the thermal resistivity, SR_d is the specific resistivity of a dislocation density which is between $1.2-3.3 \times 10^{-19} \Omega\text{-cm}^3$ for aluminum [99-101] (3.3×10^{-19} was selected as the specific resistivity of a dislocation density in this work) and, D_d is the dislocation density.

$$\rho_e = \rho_t + SR_d D_d \quad (9)$$

Temperature dependent electrical resistivity was modeled using a linear function shown in Eq. 10 [64], where ρ_0 ($=4 \times 10^{-8} \Omega\text{-m}$) is the room temperature resistivity of the unworked metal, α_t ($=0.0039$) is the temperature sensitivity of electrical resistivity, and ΔT is the temperature difference between the elevated temperature and room temperature.

$$\rho_t = \rho_0(1 + \alpha_t \Delta T) \quad (10)$$

Dislocation density was calculated using Eq. 11 [81], where σ is the flow stress, α is the thermal activation constant, b is the Berger's vector, μ is the shear modulus, and M is the Taylor factor. It has been shown that for aluminum, the thermal activation constant (α) and Taylor factor (M) are $1/3$ and 3 respectively, which cancel each other to obtain Eq. 12. This past work approached the electroplastic effect as a Joule heating phenomenon where the entire effect is thermal softening; as such, it was assumed that electricity would not interact with the thermal activation constant. In Eq. 12, an additional parameter, G_{bd} , is added as the dislocation density multiplier to compensate for dislocations stacking at grain boundaries. This term will be used later in the grain boundary model; for now it is set to unity. Using Eq. 12 resulted in an increase in electrical resistivity at the beginning of the electrical pulse which decreased as temperature increased and dislocations annihilated, potentially allowing for the prediction of the stress drop during an electrical pulse.

$$D_d = \left(\frac{\sigma}{\alpha \mu b M} \right)^2 \quad (11)$$

$$D_d = G_{bd} \left(\frac{\sigma}{\mu b} \right)^2 \quad (12)$$

Combining Eq.s 1, 2, and 4, Eq. 13 was derived which represents the total electrical resistivity from dislocations and temperature.

$$\rho_e = \rho_0(1 + \alpha_t \Delta T) + SR_D G_{bd} \left(\frac{\sigma}{\mu b} \right)^2 \quad (13)$$

First, Eq. 13 was solved numerically at 100°C and 50MPa increments of temperatures and stress to develop tabular data of electrical conductivity. Then, a user defined field subroutine (USDFLD) was written to set electrical conductivity as a function of temperature and stress values. If the grain boundary factor is left as unity, then the dislocation density is not large enough to change the electrical conductivity, meaning that the temperature and stress results are the same as shown Figure 4-5. If the grain boundary factor is increased then a larger effect on electrical conductivity is found, for example, a grain boundary factor of 1000 is used, a more significant effect is found, shown in Figure 4-6, which correlates to dislocation density of the order of magnitude 10^{17} (by contrast, with a grain boundary factor of 1, conductivity shows no relation to stress).

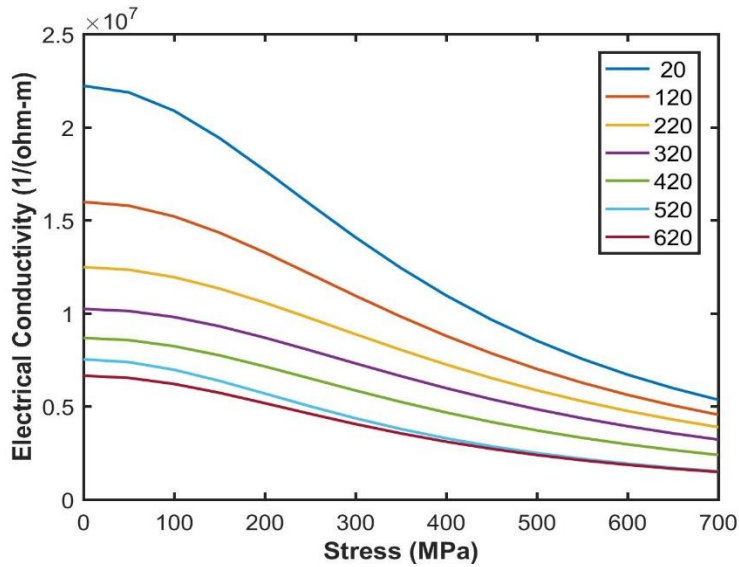


Figure 4-6: Electrical conductivity vs. stress at various temperatures (°C) with a grain boundary multiplier of 1000

Grain Boundary Model (Scaled Model)

It was found that making electrical resistivity a function of dislocation density and temperature did not cause a significant change on the bulk specimen. In order to study the heterogeneous Joule heating theory, grains and grain boundaries were modeled during the tensile test. However, the heterogeneous Joule heating theory only applies during the electrical pulses. As such, in order to reduce computational load while studying a microscale phenomenon, a small piece of the gage region of the tensile specimen was meshed with grains and grain boundaries and then solved only during the pulse duration. First, the microscale was assigned homogeneous properties (no grain boundary or dislocation density based properties) and checked to ensure it produced results similar to the bulk model during the electrical pulse. Once the grain model was tuned using deformation rate to match the bulk model, the grain boundary dislocation density multiplier

is applied and the subroutine for dislocation density and temperature based electrical resistivity was activated.

Grain size was determined to be $8.9 \pm 2.5 \mu\text{m}$ on an Electron Back Scatter Diffraction (EBSD) image of as-received 7075-T6 aluminum using the line intercept method with 20 repetitions. The grains and grain boundaries from half of the image were traced and used to create grain boundary partitions in the model, shown in Figure 4-7.

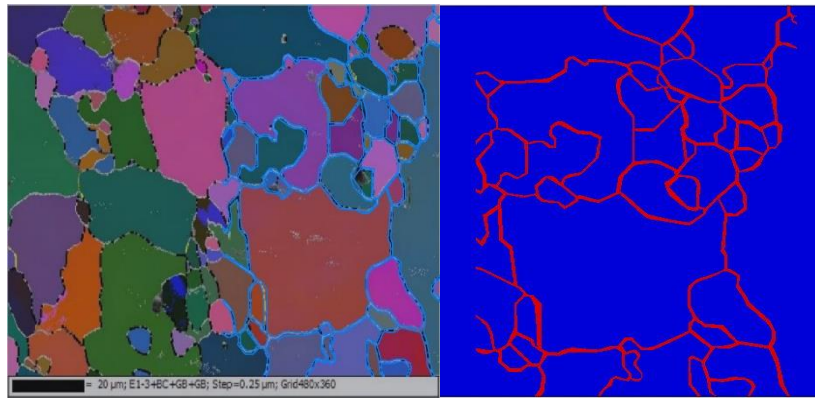


Figure 4-7: (Left) Traced grain boundaries from EBSD of as-received 7075-T6 aluminum and (right) partitioned grain boundaries in ABAQUS

The specimen size was set to a rectangle with dimensions $1 \times 0.09 \times 0.01 \text{mm}$ to reduce computational load and to prevent patterning of the copied grain boundaries. The length was much greater than the width such that stress bands resulting from the end boundary conditions will not interfere with the grain boundary region. The thickness was decreased to 0.01mm to prevent aspect ratio errors from the greatly reduced mesh size (150,000 elements, 1 element through the thickness). The grain size model represented a small piece of the central gage region, shown in Figure 4-8, this region is at a uniform axial stress level prior to the electrical pulse.

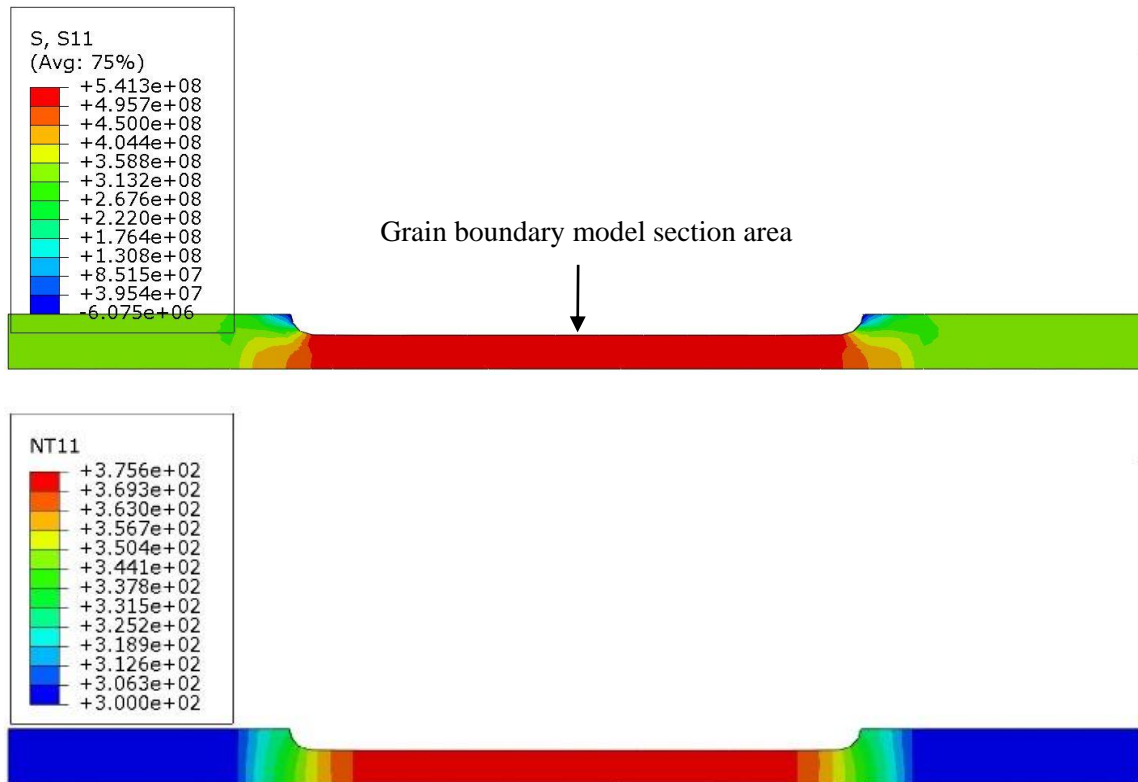


Figure 4-8: Axial stress and temperature prior to the first electrical pulse from the bulk model showing the location of the grain boundary model; axial stress in this area is 533 MPa. The temperature result from the bulk model shows that there is a uniform temperature where the grain boundary specimen is taken

Only the electrical pulse was modeled to reduce computational load rather than modeling the full plain deformation without electricity that occurred before and after the electrical pulses. The model was evaluated for the 3 pulses seen during experiment before specimen fracture of the pulsed tensile test shown in Figure 4-5. The scaled model's setup is listed below:

- The left end was fixed.
- The right end was fixed in all directions except axial direction.
- The right end was electrically grounded.

- Current density was set to match the bulk model's current density prior to the electrical pulse and was applied at the left end of the specimen.
- A velocity boundary condition was applied at the right end and adjusted such that the strain rate of the scaled model matches the strain rate of the bulk model within the gage region.
- The initial temperature and axial stress were set to the gage region temperature/stress of the bulk specimen prior to the electrical pulse.
- The solution time increment was selected as 0.05s.
 - An increment of 0.01s was tested and found not to have an effect.

The model was tested with the grains and grain boundaries both set to bulk material properties to ensure that stress and temperature throughout the 1-second pulse match the bulk model, the results are shown in Figure 4-9, which shows an example of the validation of the scaled model by comparing it to the bulk model and the experimental data.

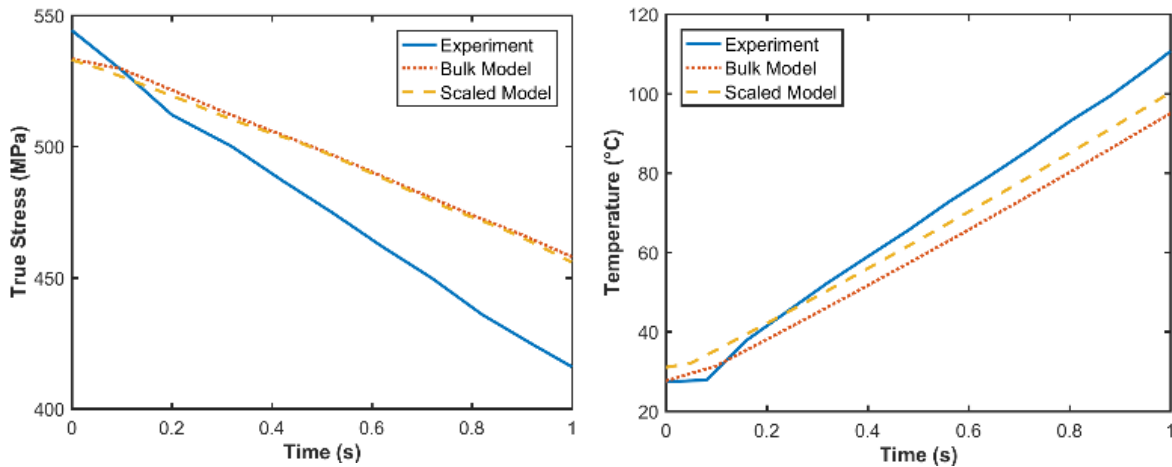


Figure 4-9: Comparison of temperature and stress for the 1st electrical pulse for experiment, bulk model, and scaled model with homogeneous properties.

The scaled model must match the bulk model to ensure that the results from adding grains and grain boundaries are fully responsible for changes in model accuracy. The experimental data is shown to show what difference the heterogeneous Joule heating theory must be responsible for, the scaled model line with grains and grain boundaries added will need to lie on top of the experimental data line. The entire scaled model specimen reached a uniform temperature, which was expected since a region larger than the micro-specimen heats uniformly in the bulk model (Figure 4-9). The temperature and stress results at the end of the 3 electrical pulses (time=1 second) are shown in Table 4-2.

Table 4-2: Comparison of stress and temperature at the end of 3 electrical pulses. The scaled model represents the scaled model with homogenous properties. The scaled model fit is the scaled model with the grain boundary dislocation density factor set to predict the correct flow stress drop.

	Experiment	Bulk Model	Scaled Model	Scaled Model Fit
1 st Pulse				
Stress (MPa)	416	457	457	417
Temperature (°C)	111	103	101	120
2 nd Pulse				
Stress (MPa)	427	477	476	426
Temperature (°C)	122	119	118	143
3 rd Pulse				
Stress (MPa)	430	487	486	432
Temperature (°C)	141	137	138	164

In this table, *Scaled Model* represents the validation of the scaled model compared with the bulk model, the material properties of this model are set to homogenous. *Scaled Model Fit* is the results from the scaled model with dislocation density and temperature dependent electrical resistivity with a dislocation density multiplier on grain boundary elements. The dislocation density multiplier was selected such that the scaled model could predict the same stress at the end of the 1-second pulse as an experiment. This resulted in grain boundary multipliers near 17,000 for each of the 3 pulses. This assumed that the entire heterogeneous resistivity difference was caused by dislocations and ignored lattice misalignment at grain boundaries as well as stacking fault density. Figure 4-10, shows an example of the fitted scaled model compared to experiment and the bulk model. In order to predict the correct stress drop the temperature at the end of the pulse (time=1 second) was higher than the bulk temperature found during the experiment, shown in Table 4-2.

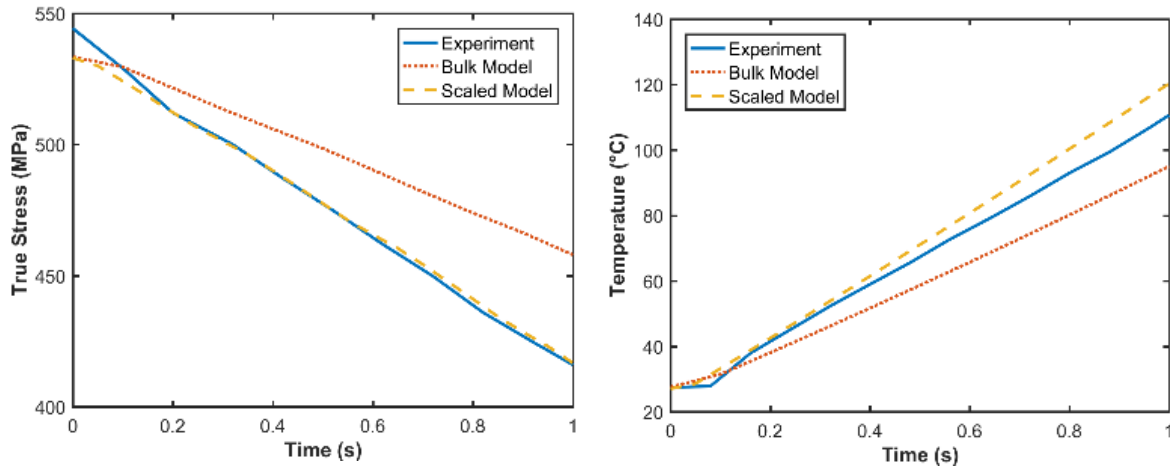


Figure 4-10: Comparison between experiment, bulk, and scaled model fit to experiment for the first electrical pulse

The fitted scaled model for the first pulse resulted in a temperature of 120°C, an 8% increase over experiment and 17% increase over the bulk model’s prediction. The fitted scaled model for the 2nd pulse resulted in a temperature of 143°C, a 17% increase over experiment and 20% increase over the bulk model. The fitted model for the 3rd pulse resulted in a temperature of 164°C, a 16 % increase over the experiment and a 20% increase over the bulk model. If the initial stress was directly matched to experiment and all other parameters are assumed to be correct the required temperature for the stress drop increased to 127°C, 14% higher than experiment for the first pulse, 149°C, 22% higher than experiment for the second pulse, and 178°C, 26% higher than experiment for the third pulse. The entire microscale model heated uniformly even though the heterogeneous resistivity field caused a non-uniform current density as shown in Figure 4-11, similar results were found in [102].

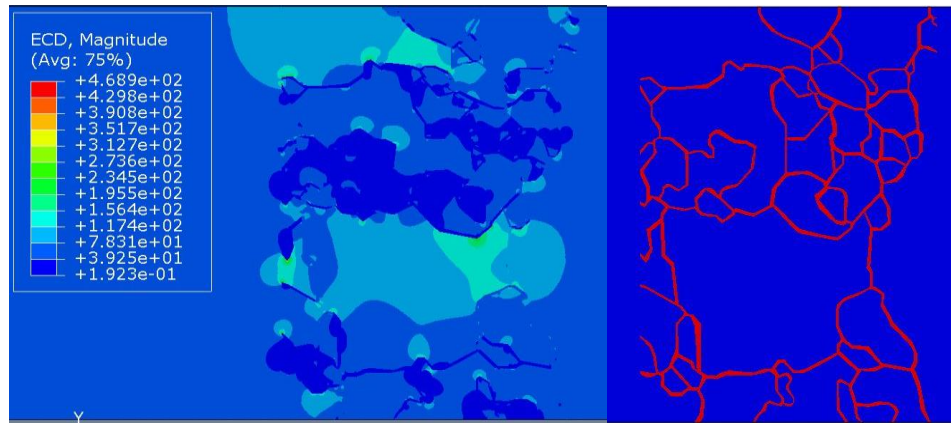


Figure 4-11: Current density field caused by grain boundary portioning (A/mm^2)

The current was concentrated in areas where there are fewer grain boundaries and larger grains due to the lower resistance to electrical flow. Changing the grain boundary dislocation density multiplier does not change the current density distribution but does change the magnitude. However, even at high current densities, above $200A/mm^2$ the grain boundaries do not rise to a higher temperature than the surrounding grains due to the thermal conductivity of aluminum. The grain boundaries are much smaller than the grains, and as such, the grains act as large heat sinks; if the grain boundaries heat up, the entire part does as well, assuming they produce enough heat to generate more heat than the lower resistance grain elements.

The dislocation density to obtain the required stress drops is on the order of $10^{19}/m^2$, this exceeds the range for dislocation density of severely worked metals (10^{18}) [103], at the first pulse, the axial strain is only 0.05, meaning the specimen is far from severely work-hardened. The ratio of the electrical resistivity of the grain boundaries compared to the grains is 190 before the electrical pulse, much higher than 2.5-10 ratio found in the literature [104]. These results suggest that heterogeneous Joule heating is unable to fully

account for the transient electroplastic effect since the grains act as large heat sinks which rapidly draw heat from the grain boundaries resulting in uniform elevated temperature fields across the entire specimen. This means that if the grain boundaries heat up enough to generate the appropriate softening to predict the transient stress drop, the predicted bulk temperature is higher than what is found in the experiment. The greater the strain when the electrical pulse is used, the greater the difference between the grain boundary model's temperature prediction and experiment. In addition, the bulk and scaled model's prediction of flow stress before the electrical pulse was typically around 10MPa under experiment, which would result in an even higher required temperature in order to predict the stress drop if the scaled model started at the experiment's flow stress.

As the grain boundaries are traced from the EBSD image, the thickness is likely larger than what is realistic which would cause the grains to heat sink the grain boundaries even faster. This is explored later in this dissertation by modifying the thickness of the grain boundaries in a specimen meshed with hexagon grains.

Precipitate Model

7075-T6 is a precipitate strengthened aluminum; T6 is the strongest precipitated version of 7075 commercially available, strengthened through uniform precipitation throughout its matrix. The precipitates are intermetallic $MgZn_2$ which has an electrical resistivity of 25.6×10^{-6} ohm-cm [105]. As the precipitates are more resistive than the base aluminum, they may influence the current density and resultant temperature results. It may be possible for the precipitates lower conductivity to force the current density to be near uniform, leading to a greater current density flowing through grain boundaries and a higher grain

boundary temperature than the scaled model. To examine this effect, precipitates were added to a section of the scaled model from the previous section. The precipitates were assumed round and evenly dispersed with a diameter of 67nm measured as the average size of the as-received material using a High-Resolution Transmission Electron Microscope (HRTEM) operating at 300kV, shown in

Figure 4-12. Similar precipitate sizes were found for 7075-T6 in [106]. The precipitate density was set to $15/\mu\text{m}^2$ [106]. The precipitates and grain boundaries used in the FEA model are shown in Figure 4-13.

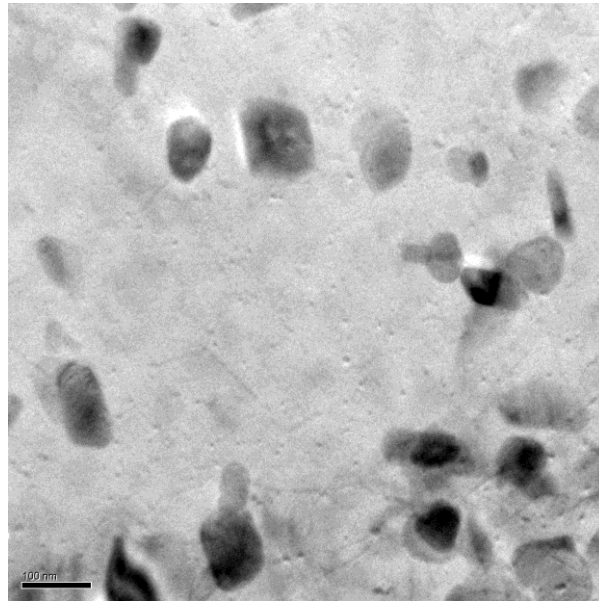


Figure 4-12: Precipitates in 7075-T6 as-received material

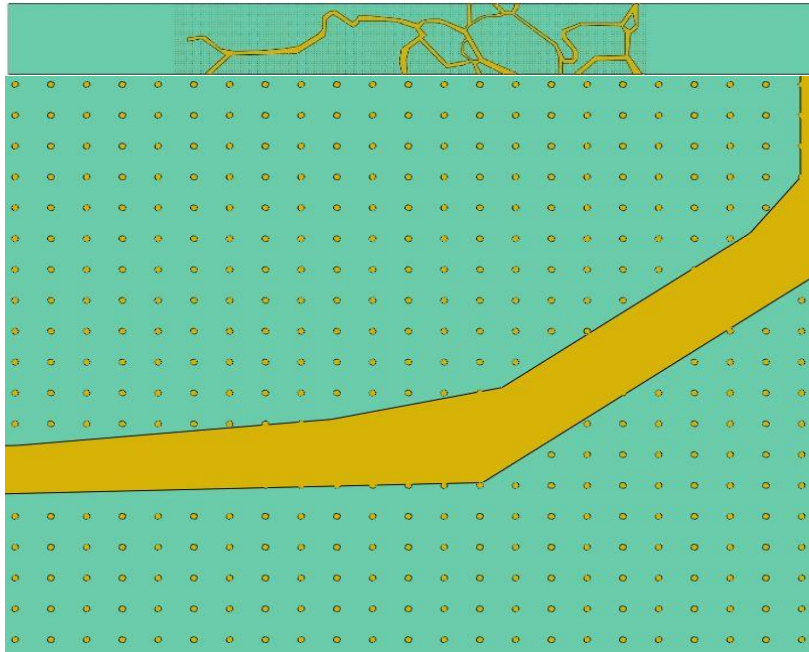


Figure 4-13: (Top) Entire specimen with grain boundaries and precipitates (bottom) zoomed in area to show precipitates

The model was tested with and without precipitates to determine the effect of precipitation on current density and resultant temperature field, the current density results are shown in Figure 4-14. The current density field contours are the same for both models; when precipitates are added there is a small increase in current density of around 1 A/mm^2 . As such, there is no significant effect on resultant Joule heating or temperature distribution as the current density field is not more uniform in the presence of precipitates.

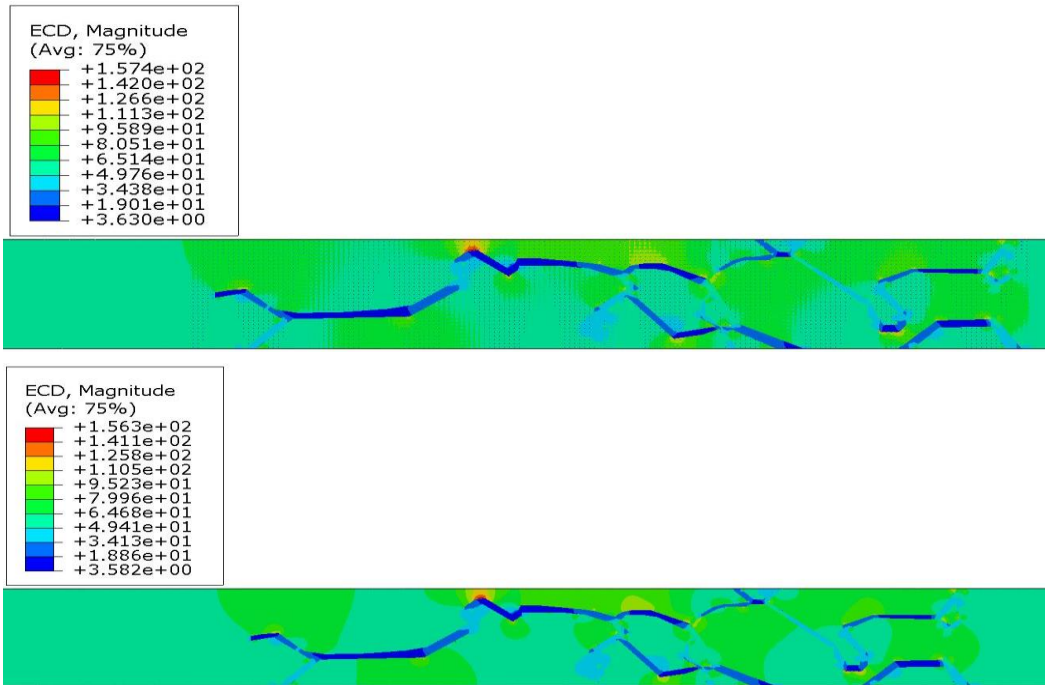


Figure 4-14: Current density results (top) with precipitates (bottom) without precipitates, units are A/mm^2

Grain Boundary Thickness Sensitivity

The scaled model used grains and grain boundaries traced from an EBSD image. However, the grain boundaries from these traced images are likely larger than realistic. As such, the the sensitivity of the scaled model to grain boundary thickness is explored in this section to allow for prediction of the effect of smaller grain boundaries than tested in the previous section on the heterogeneous Joule heating theory. Hexagonal partitioning was used in the place of traced grains for their stackability and ease of patterning in computer aided design software. The grain boundary thickness from the EBSD image was not uniform making a modification of this thickness with a uniform factor difficult. The grains were sized such that the hexagon was incirbed in a 9- μm circle. The shape was then offset to create a grain boundary, followed by patterning across the specimen; an example is shown in Figure 4-15.

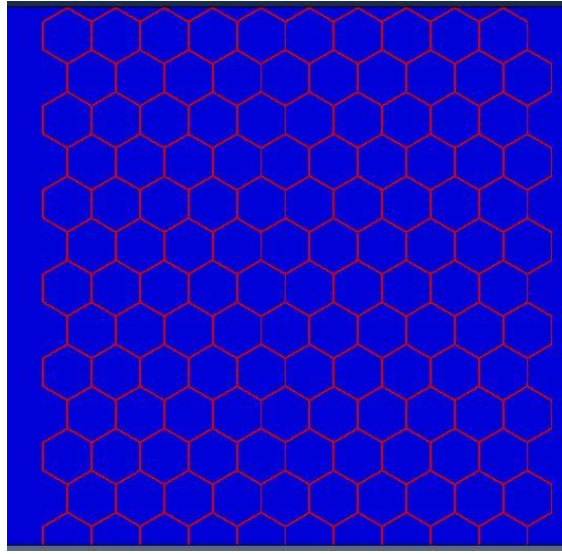


Figure 4-15: Hexagon grains and grain boundaries used in the sensitivity study

The grain boundary thickness (t_{gb}) was determined using Equation 14 [107], where k is a material constant and d_g is the grain size ($9\mu\text{m}$), k was set to a midpoint value equal to 0.125 [11]. Other values of k were created around the midpoint to study the effect of grain boundary thickness, shown in Table 4-3. As shown in the previous section, the dislocation density predicted by the model is outside of reasonable ranges. As such, the temperature-dependent electrical resistivity for grain boundary elements was multiplied by a constant to simulate increased resistivity at grain boundaries. The grain boundary resistivity multiplier constant was found by fitting the flow stress between the scaled model and experiment, the results are shown in Table 4-3.

$$t_{gb} = k \sqrt{d_g} \quad (14)$$

Table 4-3: Material constants and resultant grain boundary thickness for 9 micron hexagon grains

k	t_{gb} (μm)	G_{bd} Resistivity Multiplier
.03125	.0934	230
.0625	0.1875	120
0.125	0.375	75
0.25	0.75	30
.5	1.5	15

Smaller thickness grain boundaries require a higher electrical resistivity in order to predict the flow stress found during the experiment. This is due to the increasing grain/grain boundary size ratio that leads to more heat being taken by the grains from the grain boundaries without significant temperature rise. The grain boundary thicknesses tested are on the order of 100nm, while it is found experimentally that grain boundaries typically are in the 1-9nm range [104]. This makes the likelihood that heterogeneous Joule heating from the microscale model, causing the transient electroplastic effect, small since grain boundaries that are larger than realistic values are unable to predict the transient stress drop with a reasonable electrical resistivity.

A power curve fit model was found to have the best fit of the grain boundary multiplier data shown in Table 4-3; the resultant curve is shown in Figure 4-16.

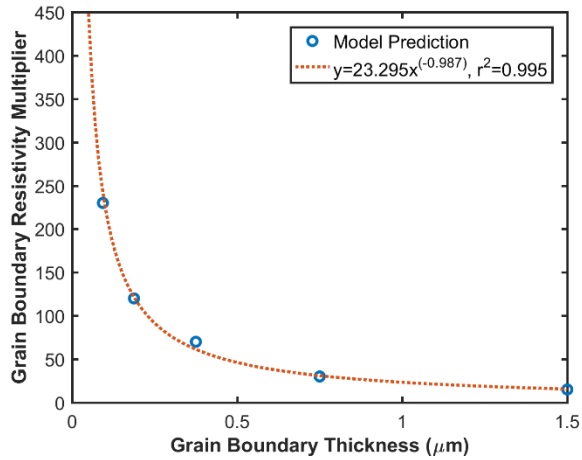


Figure 4-16: Power curve fit for grain boundary multiplier as a function of grain boundary thickness

This model predicts that using a realistic grain boundary thickness of 10nm, the required grain boundary resistivity factor to predict the correct flow stress during the second electrical pulse of the experiment is 4400. This value is extremely unrealistic, and would be even higher if applied to the scaled model with EBSD grains since the current density is much less uniform.

This sensitivity study offers a simplified view of what will happen to the resistivity at the grain boundaries, though the resistivity multipliers seem low compared to the 190 found on the actual grain and grain boundary model shown previously in this paper. The reason for this is caused by the electrical current path. Since the hexagons are a patterned feature, the current density also follows a pattern, shown in Figure 4-17, also more grain boundary area in the hexagon model lead to a lower required resistivity multiplier, yet the multiplier is still too high to be reasonable and the microscale Joule heating theory seems lost. Also, note that high current densities arise at the top of the hexagon part where the least number of grain boundaries and resultant electrical resistance exist.

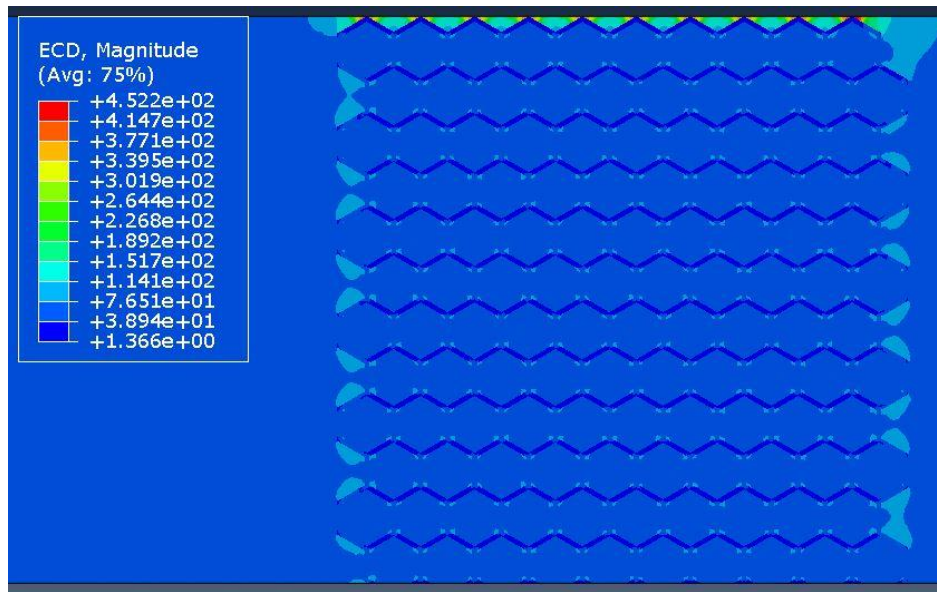


Figure 4-17: Current density results from 0.375 micron grain boundary thickness model, units are A/mm²

Conclusions

The heterogeneous Joule heating theory for explaining the transient electroplastic effect is evaluated in this research through the creation of multi-scale models which model the entire bulk tensile specimen along with a small region of the gage length where grains, precipitates, and grain boundaries are partitioned. Electrical resistivity is modeled as a function of dislocation density and temperature. The following conclusions are drawn:

- With a Joule heat fraction of 1, the correct temperature profile can be predicted using the traditional conservation of energy approach, but this does not allow for the correct prediction of flow stress during an electrical pulse.
- In order to predict the correct stress, drop in the presence of an electrical pulse based on increased resistivity at grain boundaries the bulk temperature of the part must exceed experiment. The resultant resistivity and dislocation density are outside of acceptable ranges. It is found that thinner grain boundaries require a higher electrical resistivity to

produce a required stress drop, meaning the electrical resistivity of grain boundaries are likely higher than what was found in this work. The heterogeneous Joule heating theory cannot fully compensate or explain the transient electroplastic effect.

CHAPTER FIVE

5. THE BULK MODEL, ELECTRICAL RESISTIVITY AND CURRENT DENSITY

The objective of this section is twofold. The first aspect is to evaluate whether current density is a proper quantification of the amount of electricity applied to a metal during deformation. The second is to determine if there are limits to the accuracy of the bulk temperature prediction FEA model presented in Chapter 4.

Current Density Evaluation

Current density has long been the go-to quantification of electricity applied to a metal since the field of EAM was established in the 1950s. The problem with current density is that it is devoid of time. For instance, assume a supplier wants to stamp an aluminum part using electricity. They go to an expert in the field and ask what current density to run. The literature shows that most work on aluminum uses current density between 60 and 100 A/mm². The supplier attempts to stamp the part using the suggested current density and encounters 1 of 3 possible outcomes. First, it may turn out that the current density works properly and the supplier gets the improved ductility that they need and can form the part they desire. Second, they may find that the current density is too high and that the part melted or experienced too much thermal expansion and buckled. Third, the supplier may find that there was no effect at all from the electricity. All three of these scenarios are possible, illustrating the need to take process time into account when prescribing a process. If the process is too short due to high forming rates, the current density described in the literature will not be sufficient and no effect will be found. This is similar to Kinsey's work on high strain rate tension, where at a strain rate of 1000/s there was no effect from electricity [70]. This section will evaluate different ways to quantify

the electricity flowing through a part and see if it results in better prediction of average flow stress, flow stress drop, and average temperature than the traditionally used current density.

To examine the predictability of the electroplastic effect through the bulk model and to find a better quantification of applied electricity, nominally equal energy square wave forms are created. The waveforms had different pulse duration and pulse periods, but contained the same nominal energy as a continuous current electrically-assisted test. First, 7075-T6 ASTM specimens were deformed in axial tension perpendicular to the grain with a continuous current density of 15A/mm² and two different strain rates, 0.001/s and 0.01/s. The specimens were cut from a different sheet than the scaled model testing and as such, new slightly different Johnson-Cook values were found.

Square waves were created with pulse durations of 0.3, 1, or 3sec to match with pulse periods of 60 or 20 seconds for 0.001 and 0.01/s strain rates, respectively. The tests were considered to have a nominal equal energy since the electrical energy applied in the wave form cases was found using Equation 15, assuming room temperature electrical resistivity. Where I is current, ρ_e is room temperature electrical resistivity, L_g is the gage length, t is the total amount of pulsed time through the test duration, and A_c is the cross sectional area in the gage region.

$$E = \frac{I^2 \rho_e L_g t}{A_c} \quad (15)$$

However, different wave forms will reach different temperatures which will influence the total energy of the test. Following each test, the temperature data is used to calculate the temperature dependent electrical resistivity and the actual electrical energy

used during the test, the results are shown in Table 5-1. The reason that the waves were equated nominally rather than following the tests was to match the convention for current density. Current density is not temperature dependent and is an easy number to record for a given test setup and alloy, nominal energy can be used in the same way. Actual energy would require knowing the temperature history of the process to adjust the electrical resistivity. The bulk model was applied to each case shown in Table 5-1.

Table 5-1: Square wave forms to nominally match the electrical energy from a continuous electrical application and the actual energy calculated after experiment for each waveform

0.001/s Strain Rate			
Pulse Period (s)	Pulse Duration (s)	Current Density (A/mm ²)	Actual Energy (J)
continuous		15	1141
60	1	124	1741
60	3	71	1614
60	0.3	226	859
20	1	71	1357
20	3	41	1305
20	0.3	130	1572
0.01/s Strain Rate			
Pulse Period (s)	Pulse Duration (s)	Current Density (A/mm ²)	Actual Energy (J)
continuous		15	155
10	1	49	77
10	3	28	163
10	0.3	89	80
3.5	1	28	136
3.5	3	16	142
3.5	0.3	51	140

It is found that almost every waveform at 0.001/s strain rate used more energy than the continuous case, with the exception of the 226 A/mm² applied for a pulse duration of 0.3 seconds with a pulse period of 60 seconds. This test fractured after the first pulse, where

all the other 60 second period waveforms had 2 pulses before fracture. Almost all of the 0.01/s strain rate cases had less energy than the continuous waveform, most of these specimens fractured before the baseline and did not get all of their required pulses in. Example experimental results for temperature and flow stress from both strain rates are shown in Figure 5-1.

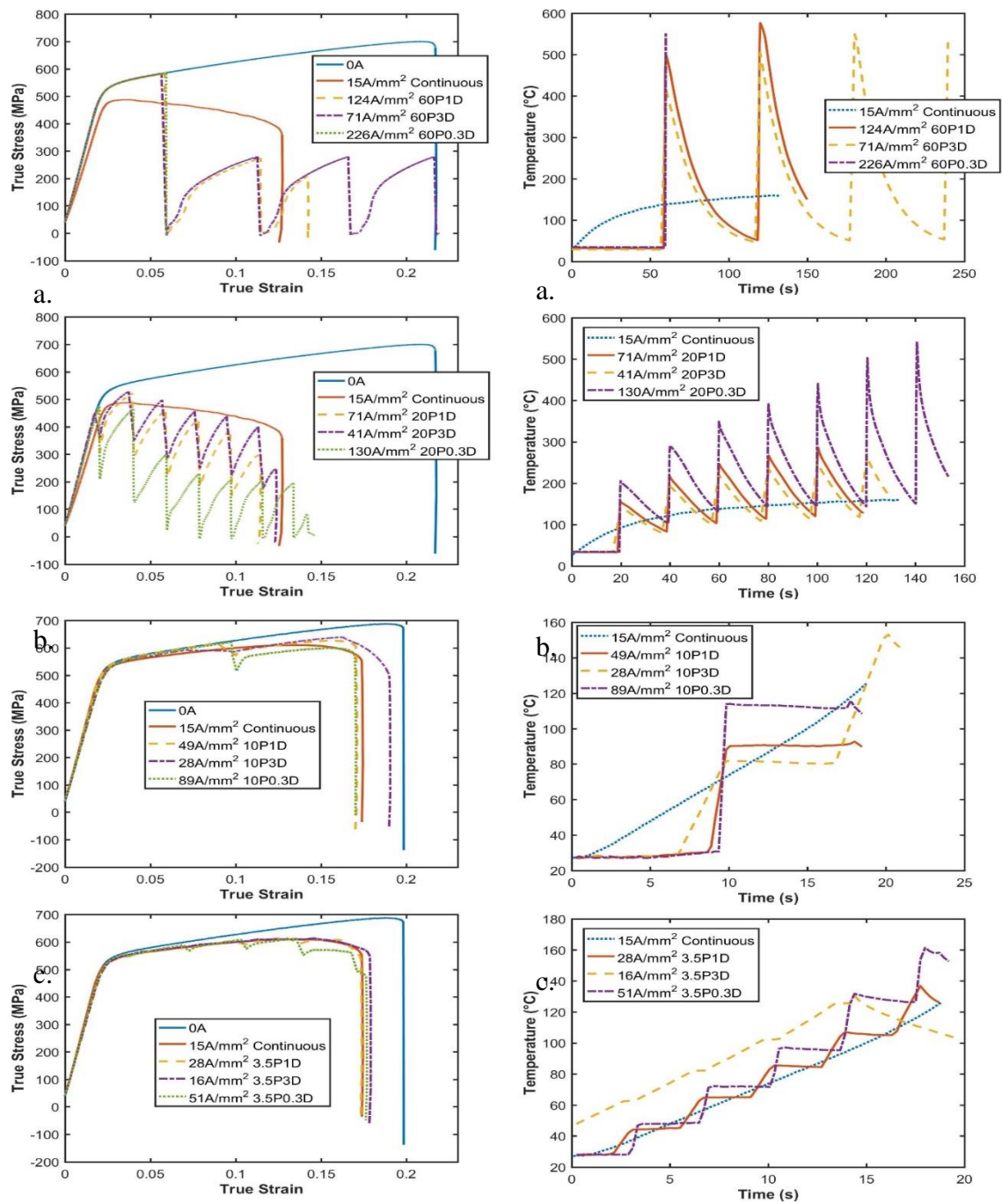


Figure 5-1: Experimental stress (left) and temperature (right) results at 0.001/sec strain rate for (a) 60sec period waves, (b) 20sec period waves, (c) 10sec period waves, (D) 3.5sec period waves

To attempt to find a replacement for current density, the inputs of current density, energy, the average electrical power per pulse, duty cycle current density, and duty cycle power per pulse were correlated with outputs of average stress, ductility, maximum temperature, average temperature, and flow stress after the first electrical pulse. Quadratic and linear fits were used, the goodness-of-fit results are shown in Table 5-2.

Table 5-2: Quadratic and linear regression accuracy between inputs and outputs for use in replacing current density. Values greater than 0.65 are highlighted green.

Quadratic R² Fit Values					
	Avg Stress	Ductility	Max Temp	Avg Temp	1st Pulse Stress
CD	0.42	0.58	0.62	0.33	0.56
Energy	0.95	0.58	0.69	0.69	0.70
Pulse Power	0.29	0.58	0.61	0.33	0.46
DC CD	0.29	0.25	0.59	0.05	0.56
DC Pulse	0.33	0.15	0.22	0.17	0.31
Linear R² Fit Values					
	Avg Stress	Ductility	Max Temp	Avg Temp	1st Pulse Stress
CD	0.17	0.40	0.58	0.00	0.54
Energy	0.93	0.11	0.68	0.65	0.70
Pulse Power	0.04	0.49	0.44	0.03	0.40
DC CD	0.23	0.10	0.16	0.09	0.20
DC Pulse	0.21	0.06	0.36	0.03	0.28

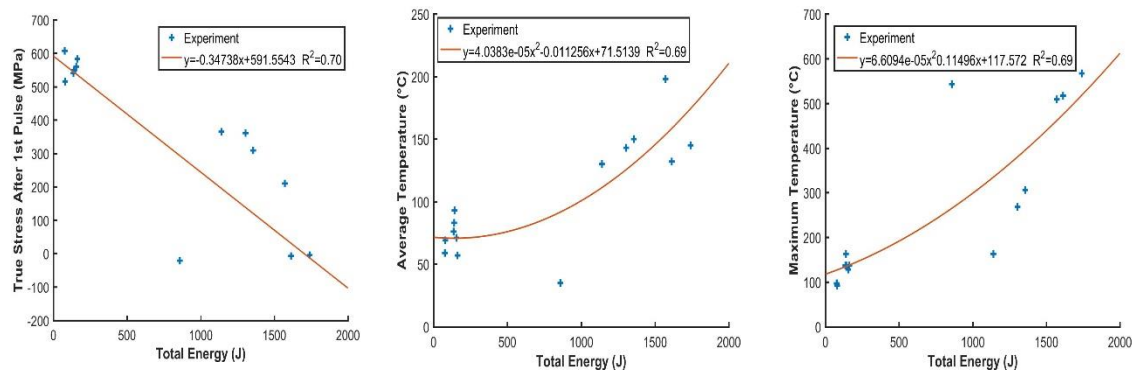


Figure 5-2: Correlation between input of energy and outputs of 1st pulse stress, average temperature, and maximum temperature

It is found that for every output studied, except for ductility, energy is a better predictor of the outcome of the tensile test than current density. Remember that current density does not take into account time and there were 2 different strain rates used to gather data. As such, since energy takes into account time, which allows it to better account for Joule heating effects, it is found that energy can better predict the outcome of the tension test than any other input variable studied. The trends with respect to the input of energy are shown in Figure 5 2. The large outlier that appear at 800 Joules are from the 226A/mm² 60P0.3D test, this test will be examined using the bulk model. If this effect is thought of as entirely thermal, then it would be expected that greater amounts of electrical energy would result in low flow stress and higher temperature. However, the predictor for stress after the first pulse should show better correlation than 70%, suggesting that there are effects other than thermal in play. In addition, the temperature results also show correlation near 70%. Some of this error is caused by inelastic heating, not considered in the energy calculation in order to match the use of current density, which only considers electrical effects. The 0.001/s strain rate case did not experience strain heating and there was no

increase in temperature observed in the 0A testing. However, the 0.01/s strain rate case increased the temperature by 20°C without electricity present. This does not explain the large outlying value at 800 Joules which is evaluated using the bulk model.

Evaluation of the Bulk Model and Comments on Electrical Resistivity Modeling

Most papers in the literature that use a bulk FEA model similar to the bulk model presented in this research only test a single parameter set [7; 54; 65]. In order to further evaluate the bulk model and to determine if limitations exist with respect to its temperature and flow stress drop prediction accuracy the model is used to match experimental results for various square wave electrical applications of varying current density at 2 different strain rates. Each of the tests shown in Table 5-1 is modeled in ABAQUS using the bulk model discussed in Chapter 4. The Johnson-Cook parameters are verified in the same way; their values are slightly different in shown in Table 5-3. This is caused by the use of a different sheet of 7075-T6 cut such that the grain direction is perpendicular to the tensile direction, rather than parallel in the previous case. Since two strain rates are used, one of which is not quasi-static, the strain rate sensitivity term C is used. Though, it is seen that the aluminum is not strain rate sensitive by the low C value and the results without electric current, shown in Figure 5-3.

Table 5-3: Johnson-Cook Parameters for Bulk Model Evaluation Study

A (MPa)	B (MPa)	C	n	m
525	678	0.024	0.61	1.56

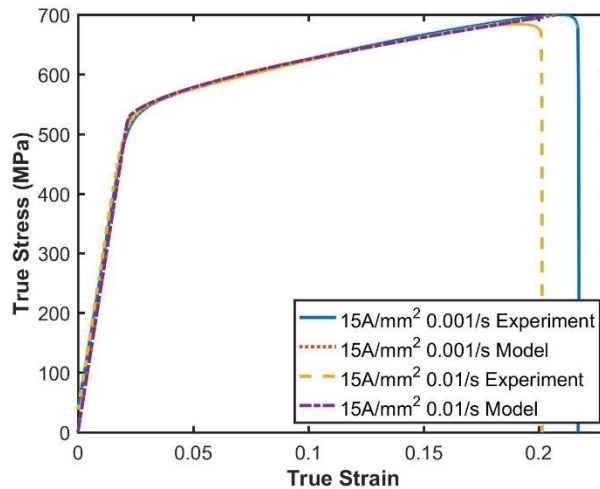


Figure 5-3: Model vs. experiment for OA tension of 7075-T6 at 2 strain rates

A sampling of the results from the bulk model is shown in Figure 5-4. The flow stress result in Figure 5-4a is interesting, and has not yet been studied in the literature. At the 0.001/s strain rate, the electricity causes the strengthening mechanisms of the aluminum to change from strain hardening to strain weakening, something which the model cannot account for using the Johnson-Cook representation. At the 0.01/s strain rate, this effect disappears and the strengthening mechanism returns to strain hardening. This suggests that a time dependent mechanism exists for the aluminum that can change the hardening mechanism even at low temperature. It may be possible that the electricity interacts with precipitates in the aluminum causing them to grow or to return to solution, which would cause a drop in strength. This is known to happen at high temperature and is the reason why some of the square waves, such as 60P3D in Figure 5-4b, do not return to their predicted strength even when at room temperature following an electrical pulse. However, this wave form reaches over 500°C, which is known to cause overaging and with enough time can force precipitates back into solution, which would counteract the strengthening

caused by the precipitates. However, rapid softening should not occur as a thermal mechanism at the low temperature achieved during the continuous current tests (150°C) suggesting there may be a further electrical effect. As such, the effect of electricity on precipitation will be studied in Chapter 7. When examining the accuracy of the temperature model, an interesting trend is found, shown in Figure 5-5. The accuracy of the bulk model's temperature prediction is within 10% for any current density tested under 89 A/mm². Once current densities exceed 89A/mm² the accuracy of the model drastically decreases, reaching a 45% error for a square wave with a current density of 226A/mm² a pulse duration of 0.3 seconds and a period of 60 seconds. In order to exclude model based errors, especially for the short pulse duration tests, the time step is set to 0.001 seconds and the mesh density is doubled. The same results are found, suggesting that the error is not caused by the model setup. In addition, lower current density tests such as 71CD3D60P reached similar temperatures to the 226CD0.3D60P test, both nearing 570°C, yet the 71CD3D60P temperature accuracy is under 10%, suggesting that the thermal properties used are not the cause of the error, this leaves only electrical resistivity to question.

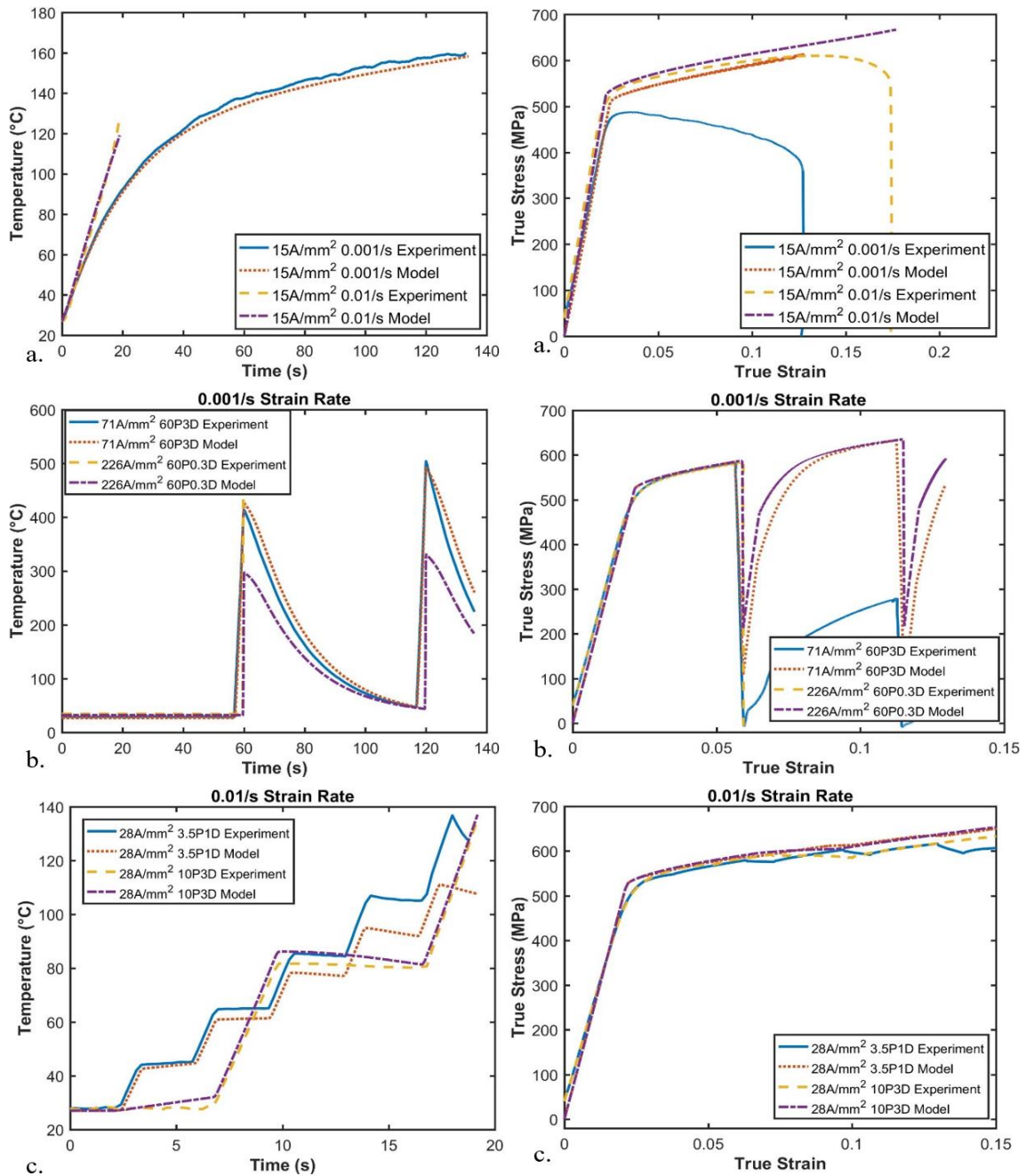


Figure 5-4: Temperature (left) and stress (right) experiment vs. model results for (a) continuous current for both strain rates, (b) 2 wave forms at 0.001/s strain rate, (c) 2 wave forms at 0.01/s strain rate

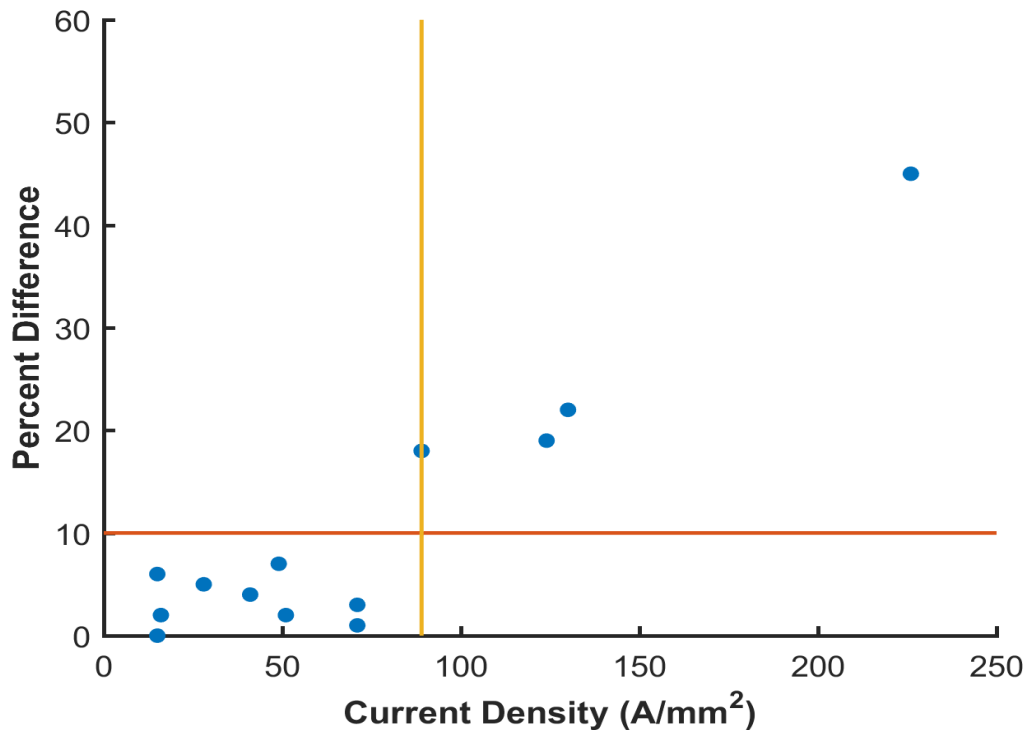


Figure 5-5: Accuracy of the temperature prediction of the bulk model, the yellow vertical line is at 89A/mm², the horizontal line is at 10% accuracy. Note that increasing loss in accuracy as current density increases past 89A/mm².

The sudden loss in accuracy of the temperature model suggests that the electrical resistivity model traditionally used may have flaws. The traditional model assumes a linear relationship with temperature but does not take into account the current density applied to the metal during electrically-assisted operations. Electrical resistivity is a measure of energy lost through electrons collisions as electrons travel through a metal's lattice, colliding with other electrons, ion cores, and other obstacles. Increasing the number of electrons in the lattice by increasing the current density could result in a greater number of collisions and a greater increase in electrical resistance than what can be accounted for by a traditional linear temperature based model. If the tests with a current density of 89A/mm²

or higher are omitted from the trend analysis done in the previous section, then the results in Table 5-4 are obtained. Upon removing the outliers that may be caused by an interaction between electrical resistivity and current density, it is found that the trends strengthen and appear dominantly quadratic. Ductility suddenly appears predictable. Part of this is caused by early fracture from the high current density cases, most of which did not last as many pulses as lower current density wave forms of the same pulse period. As mentioned before, strain heating may play a role in the accuracy of energy being used as a predictor when only electrical energy is considered. However, as shown in the outlier compensated results, the maximum temperature is almost perfectly correlated with energy and average temperature is 90% correlated. The average temperature would experience a greater impact from strain heating than the maximum temperature, since during the electrical pulse, electrical heating will dominate strain based heating, especially if the specimen goes into compression and experiences a temporarily lower strain rate. Energy once again is a much stronger predictor of process performance than current density. However, if electrical resistivity is affected by current density past a threshold point (in this case 89A/mm^2) then the energy prediction can only be used if the metal's threshold current density is known and the applied current density is known to be less. As such, using predictors of process performance for an electrically-assisted manufacturing process will require both energy and current density, but will be more accurate than using current density alone and can compensate for time dependent effects which current density alone cannot account for.

Table 5-4: Linear and quadratic curve fit coefficients to show predictability of the electroplastic effect when high current densities are ignored

Quadratic R² Fit Values under 85 A/mm²					
	Avg Stress	Ductility	Max Temp	Avg Temp	1st Pulse Stress
CD	0.56	0.01	0.67	0.37	0.61
Energy	0.99	0.79	0.96	0.90	0.96
Pulse Power	0.20	0.56	0.28	0.26	0.39
DC CD	0.33	0.01	0.42	0.23	0.34
DC Pulse	0.51	0.14	0.27	0.48	0.35
Linear R² Fit Values under 85 A/mm²					
	Avg Stress	Ductility	Max Temp	Avg Temp	1st Pulse Stress
CD	0.40	0.01	0.51	0.18	0.35
Energy	0.98	0.11	0.71	0.87	0.83
Pulse Power	0.06	0.45	0.02	0.19	0.00
DC CD	0.16	0.01	0.24	0.03	0.11
DC Pulse	0.30	0.08	0.16	0.20	0.19

Conclusions

The use of current density as a predictor of process performance for electrically-assisted manufacturing processes was examined using a linear and quadratic trend analysis of nominally equal energy wave forms. The same waveforms were used to evaluate the accuracy of the bulk model's temperature prediction accuracy across a range of current densities varying from 15 to 226A/mm². The following conclusions are drawn:

- Electrical energy used during an electrically-assisted manufacturing operation is a better predictor of flow stress, ductility, and temperature than current density. However, in order to use electrical energy, the temperature of the part during the test has to be known or predictable using conventional modeling techniques to allow for the calculation of temperature dependent electrical resistivity.

- The bulk model can be used as a temperature predictor to allow for calculation of electrical energy, so long as the current density applied is less than the threshold current density, at which point the temperature model loses accuracy.
- Electrical resistivity is likely correlated to both temperature and current density, as seen as the bulk temperature model lost accuracy past 89A/mm^2 ; any current density less than this level was within 10% of experimental results. Further research is required to create models to predict electrical resistivity as a function of current density and temperature.

CHAPTER SIX

6. A NEW THEORY: ELECTRON STAGNATION

It was shown in Chapter 4 that none of the testing existing theories for predicting the electroplastic effect are adequate. The only theory remaining was the dissolution of bonds theory which lacks detail for explaining the electroplastic effect. This section presents a new theory termed the *electron stagnation theory*, which focuses on better explaining the dissolution of bonds theory, its applicability and limitations for describing the electroplastic effect. Chapter 5 suggested that electrical resistivity could correlate with current density; this is theoretically studied in this chapter.

The 5 Criteria of an Electroplastic Effect Theory

This section will present a revised version of the dissolution of bonds theory to explain various phenomena associated with the electroplastic effect. It is the authors view that a proper electroplastic effect theory must be able to explain 5 major phenomena which show distinct differences between conventional bulk heating deformation and electroplastic methods. First, the general theory will be explained and then each of the 5 points below will be addressed.

1. **Flow Stress Difference:** The transient stress drop caused during pulsed tension which cannot be predicted using Joule heating and thermal softening [7; 54]. Along with the difference between furnace heated and electroplastic deformation (electroplastic has a lower flow stress) [11; 14; 60; 62].
2. **Deformation Mechanisms and Grain Boundary Melting:** A shift in deformation mechanisms, most often observed in magnesium through elimination or reduction of twinning in the presence of electricity [108].

3. **Threshold Effect:** Some metals will not have a reaction to electricity during electrically-assisted deformation until a threshold current density is reached, after which, a large benefit is found, often observed as a large reduction in flow stress [25].
4. **Cold Work and Grain Size Dependency:** The influence of strain hardening and grain size on the electroplastic effect, smaller grains and larger degrees of strain hardening increase the stress reduction from the electroplastic effect [15; 69]
5. **Time Dependency:** The absence of an electroplastic effect at high strain rate during the short time period tension testing [70]. There must be a time dependency on the proposed electroplastic mechanisms.

The Electron Stagnation Theory

The application of electric current to a metal will result in an increased number of electrons in the electron cloud proportional to the applied current density. The electrons will move at a drift velocity with emphasized directionality towards ground. As the electrons move through the metal they will encounter precipitates, grain boundaries, dislocations, and other obstacles, all acting as impediments to electron flow. To further explain the electron stagnation theory, a case study for precipitate effects is presented.

Electrons flowing towards a precipitate of increased electrical resistivity will be forced to flow around the precipitate, similar to water flowing around a rigid body within its flow. At the central point where the water contacts the rigid body there is a stagnation point, where the velocity of the water reaches 0 and water behind it slows. A similar phenomenon may happen with electrons moving past obstacles. However, electrons do not flow in a straight line, instead, they move about in random patterns until colliding with

an obstacle or other electrons which redirect their path. Due to the applied current's resultant electrical potential, the motion vectors of the electrons point towards the ground, unless deflected for a brief period of time due to the collision. This will result in electron stagnation points on the precipitate resulting in increased electron density, likely with an emphasis on the upstream side of the obstacle, as shown in Figure 6-1.

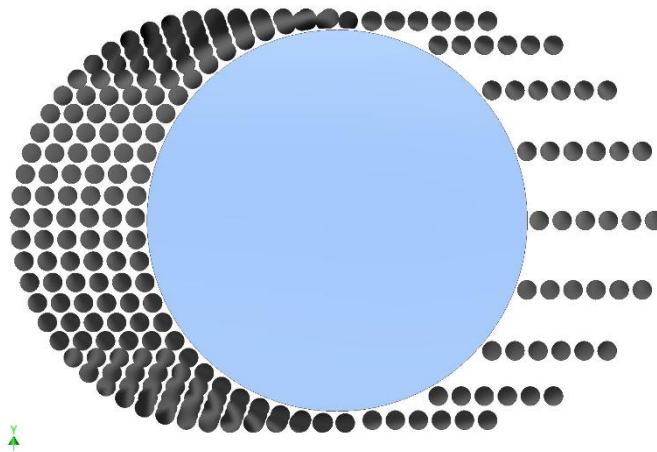


Figure 6-1: Increased electron density at an obstacle due to electron stagnation, the large blue dot is an obstacle, the smaller black dots are electrons

This increased electron density will reduce sharing of electrons by ion cores near the impeding edges of the precipitate. If there is an electron near the stagnation point it will be hit with continuous collisions of electrons as they reach the stagnation point and slow, resulting in a momentum transfer. The momentum transfer, coupled with weakened bonds and temperature rise from Joule heating will allow dislocations to move past the obstacle with lower resistance. In addition, the increased electron density will lead to an increased electrical resistivity near the precipitate causing a slight increase in temperature rise and an increase in energy state for ion cores whose bonds are already weakened through dissolution. A similar reaction would occur when electrons encounter dislocations or other

small obstacles, the increased electrical resistivity will force the electrons to move around the obstacle causing stagnation points on the obstacle and increased electron density.

As dislocations encounter voids, interstitials, and precipitates, dislocation loops may form around the obstacle leading to an effectively larger stagnation zone around the obstacle.

This effect would be magnified at grain boundaries, as increased dislocation tangles and lattice misalignment will lead to increased electron stagnation and a greater electron density on the impeding side of the grain boundary. Due to the length of grain boundaries, the stagnation regions will be larger, resulting in a greater electron density than a single obstacle such as precipitate. As such, it is expected that dislocation motion resistance will be lowest at grain boundaries.

Analogy of the Electron Stagnation Theory

The electron stagnation theory can be thought of using the following analogy. Think of sports fans (electrons) trying to leave a sporting event at a large stadium. There are a large number of fans that want to move towards the parking lot (electrical ground) from the main seating (grain region) when the game has ended. To get to the parking lot they must move through a limited number of exits from the seating area (passable areas within the grain boundary). When everyone tries to leave the game, the constriction of the exits leads to a backup and congestion of people behind the exit area and into a portion of the seating area. This is coupled with a decrease in the movement speed of the people due to the large number and close proximity of the people in the exit area. The same thing may happen at grain boundaries in a metal. Dislocations tangles and lattice misalignment at grain boundaries reduce the number of free paths (exits) for electrons to flow through the

metal resulting in excess electrons that are slowed down near these exit points, similar to people slowly leaving a sporting event. This analogy will be used to address the 5 major phenomena presented earlier.

Satisfaction of the 5 Criterion

Flow Stress Differences

Dislocation motion is assisted through bond dissolution due to an increased electron density near electron stagnation points on an obstacle. This would result in easier dislocation motion, leading to a stress drop beyond what is explainable through thermal softening and a lower flow stress in the presence of electricity compared to equivalent temperature furnace heated specimens.

Deformation Mechanisms

If a large enough electron density due to electron stagnation appears near grain boundaries, the resultant weakening or dissolution of bonds may lead to localized changes in slip mechanisms from crystal slip to grain boundary sliding. This phenomenon may explain why magnesium does not twin as significantly in the presence of electric current [108].

If the dissolution of bonds and increased energy state is high enough at the grain boundaries, then it may be possible to witness grain boundary melting below the normal melting temperature of a given metal, similar to what was observed in [14]. With more of the bonds near the grain boundary already dissolved or weakened, the remaining bonds that must be broken through thermal application to achieve melting would be decreased. This would result in a lower melting temperature and the potential for grain boundary melting, though restricted to areas of elevated electron density, such as grain boundaries.

Threshold, Grain Size, and Cold Work Effect

The threshold effect occurs when a metal does not react to electricity until a large enough current density is applied, after which, the effect of electricity is significant. This is typically observed as a large reduction in flow stress in tension or compression compared to current densities under the threshold value. However, not all metals experience a threshold effect [25].

Using the stadium analogy, assume a stadium has 10 exits and 100 people in the stands. There will not be any traffic when the game ends and the people leave. If there are 1 million people in the stands at the end of the game, then suddenly there is going to be a large amount of traffic and a backlog of people near the exits. The traffic at the exits will be a function of the total number and size of the exits. However, local obstacles (precipitates and dislocations) in exit areas or in the seating area that must be passed to get to the exits will require fewer people to cause congestion at the exits and a backlog due to less straight paths to the exits.

In order for the electroplastic effect to be activated, there must be electron stagnation, theorized to be the most significant at the grain boundaries. If there are not enough electrons pushed through the metal to cause significant stagnation, then the electroplastic effect will be weak or absent. While a threshold current density has not been found for all metals, it is likely possible to experience a threshold on all metals, based on the treatment of the metal. Siopis *et al.* showed that increasing grain size increased the threshold current density in copper [69]. Larger grains have a lower grain boundary-grain area ratio (more exits for a given area), resulting in less electron stagnation across the metal for a given current density. As such, a larger current density is required to reach the

required electron stagnation for dissolution of bonds to take significant effect. Size and density of precipitates, prior cold work will also affect the threshold current density and electroplastic effect.

A large number of precipitates will result in more localized electron stagnation allowing for localized dissolution of bonds aiding in dislocation motion near these objects. A metal with a large number of precipitates would be expected to possess a lower or absent threshold current density compared to a similar metal with the same grain size and fewer precipitates. Cold work would present a similar effect, both through smaller localized regions where dislocations are present, along with grain boundaries where dislocation tangles tend to form. A metal that is heavily cold worked will have a lower threshold current density than the same metal absent cold work [15].

Time Dependency

Using the stadium analogy, a camera watching the exits of a stadium as a game is ending will be able to see the progression and creation of traffic near the exits. If the camera only films for a couple of seconds after the end of the game, then it will not observe the traffic that will build up as more of the crowd of people begins to leave. However, if the camera films for a long period of time, it will observe a buildup of people near the exits, assuming there are enough people in the stadium to cause traffic at the exits. If there is not enough time given to create significant electron stagnation, it is unlikely that the electroplastic effect will be observed. In addition, time is needed to allow for Joule heating and thermal softening; this additional energy to stagnation zones will allow for easier dislocation motion than what could be achieved with weakening or dissolution of bonds alone. Therefore with short test times, such as the high strain rate testing in [70], there is

likely a lack of an effect due to low-temperature rise and an inadequate amount of time for electron stagnation to develop. However, this could be countered in the future by testing with a much higher current density.

CHAPTER SEVEN

7. EFFECT OF ELECTRICITY ON PRECIPITATES IN 7075-T6 ALUMINUM

This section examines the effect of electricity on precipitates in 7075-T6 aluminum in an attempt to explain the bulk model inaccuracies and transition from strain hardening to strain weakening for low strain rate continuous current application found in Chapter 5.

Precipitation Measurement and Microscopy

Traditional optical microscopes work by focusing light onto a specimen through a magnifying lens to make the specimen appear larger [109]. Transmission Electron Microscopes (TEM) work in a similar fashion, except that instead of a light source an electron beam is used. The specimen is held in vacuum to both protect the specimens from corroding due to its thickness and exposure to air, as well as allowing easier passage for electrons, which struggle to move in air. The lenses in a traditional microscope are replaced by electromagnets which are used to control the electron beam. When the beam passes through the specimen, it strikes a screen at the base of the microscope allowing for the creation of an image. TEM microscopes are the strongest magnifying microscopes available, able to see to a resolution of 1 nm.

Precipitate size and distribution was measured using a Hitachi H9500 high resolution TEM operated at 300kV. TEM specimens were prepared using Focused Ion Beam Milling (FIB) on a Hitachi NB5000 nanoDUE'T Double Beam Microscope. TEM specimens are milled down to a thickness of near 100nm and are square in size with width of approximately 5 microns. Precipitate size was determined by measuring the vertical and horizontal spans of each precipitate and then averaging them together; an example

measurement is shown in Figure 7-1. In 7075 aluminum, the precipitates are hexagonal Laves phase $MgZn_2$.

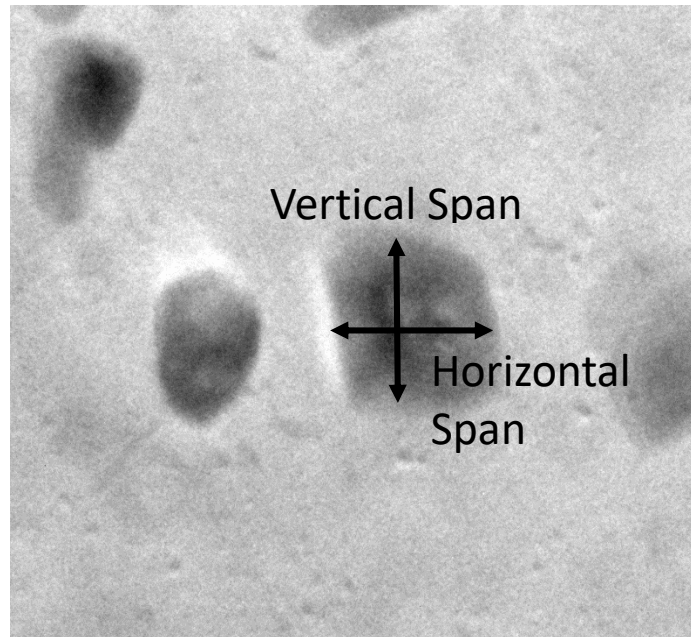


Figure 7-1: Precipitate measurement, the dark spots are precipitates. The precipitate size is found by averaging the vertical and horizontal spans

The Effect of Current Density on Precipitation

Specimens were selected from the testing used in Bulk Model Evaluation study conducted in Chapter 5, as shown in Table 7-1. TEM films were created using FIB and imaged on an H9500 TEM, and measurements were made as described by the previous section. Each sample was imaged and the precipitates measured in 5 different locations. Samples of the TEM images captured are shown in Figure 7-2 for 0.001/s strain rate and Figure 7-3 for 0.01/s strain rate. Figure 7-4, shows a plot of precipitate size and distribution with errors bars for comparison between different current densities for each strain rate.

For the 0.001/s strain rate case, it is found that the precipitate size for the $15A/mm^2$ case is not different from the base material, meaning that the electricity and temperature

increased caused by Joule heating did not affect the precipitate size. However, precipitate density at 15A/mm^2 is less than the base material. Since there are not significant differences between the 15A/mm^2 continuous case and the as-received material, the conversion from strain hardening to strain weakening noticed in Chapter 5 is likely not caused by changes to the precipitates and instead may be related to continuously building electron stagnation, as explained in Chapter 6. The precipitate size is greater (40% larger for 71CD and 55% larger for 226CD, using the mean value) than the base material at both 71 and 225A/mm^2 . Since the error bars overlap on these 2 specimens, a conclusion on which has larger precipitates cannot be drawn. Both specimens reached near the same max temperature near 570°C but the 71CD3D60P test was predicted with good accuracy by the model while the 226CD0.3D60P had the largest error at 45% using the bulk model. Both current densities have lower precipitate density with a decrease in precipitate density of 67% and 89%, respectively.

For the $0.01/\text{s}$ strain rate cases, the size of the precipitates was not significantly affected, there is no size difference between the 3 cases and the base material. However, precipitate density saw a more significant impact with a 40% decrease in precipitate density in the 28CD1D3.5P case. These impacts will be studied using a trend analysis, similar to the one conducted in Chapter 5.

Table 7-1: Average precipitate size and density comparison of electrically-assisted tensile specimens

Current Density (A/mm ²)	Pulse Period (s)	Pulse Duration (s)	Strain Rate (1/s)	Avg Precipitate Size (nm)	Avg Precipitate Density (1/μm ²)	Avg Temperature (°C)	Max Temperature (°C)
As-Received, Undeformed				47	28	-	-
15	Continuous		0	45	25	130	163
71	60	3	0	66	9	132	517
225	60	0.3	0	73	3	35	543
15	Continuous		0.01	44	20	71	128
28	4	1	0.01	52	13	76	137
89	10	0.3	0.01	50	17	69	92

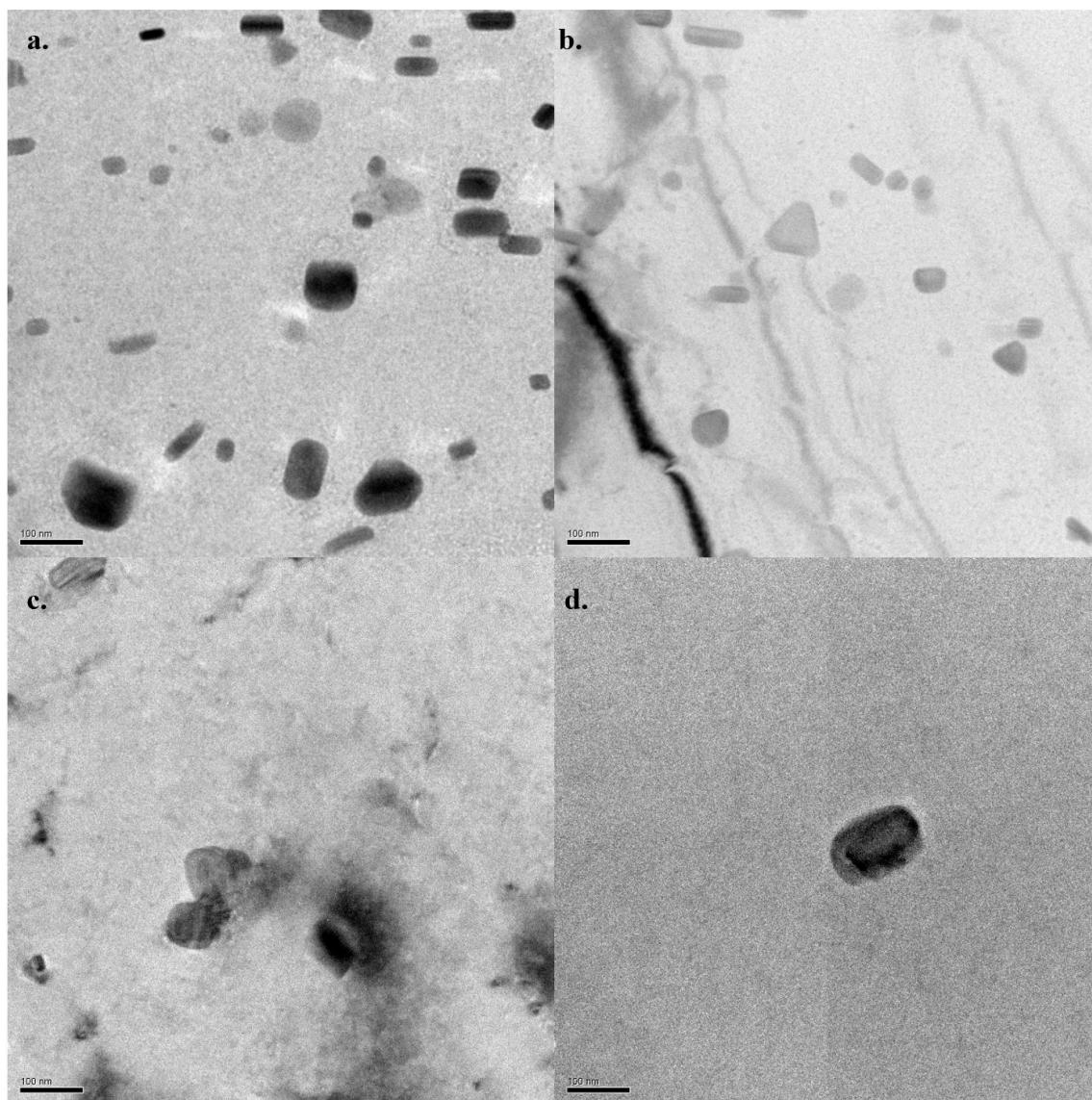


Figure 7-2: TEM images of precipitates from electrically-assisted tension conducted at a strain rate of 0.001/s, (a) as received, no deformation, (b) 15 A/mm² continuous, (c) 71CD3D60P, (d) 226CD0.3D60P

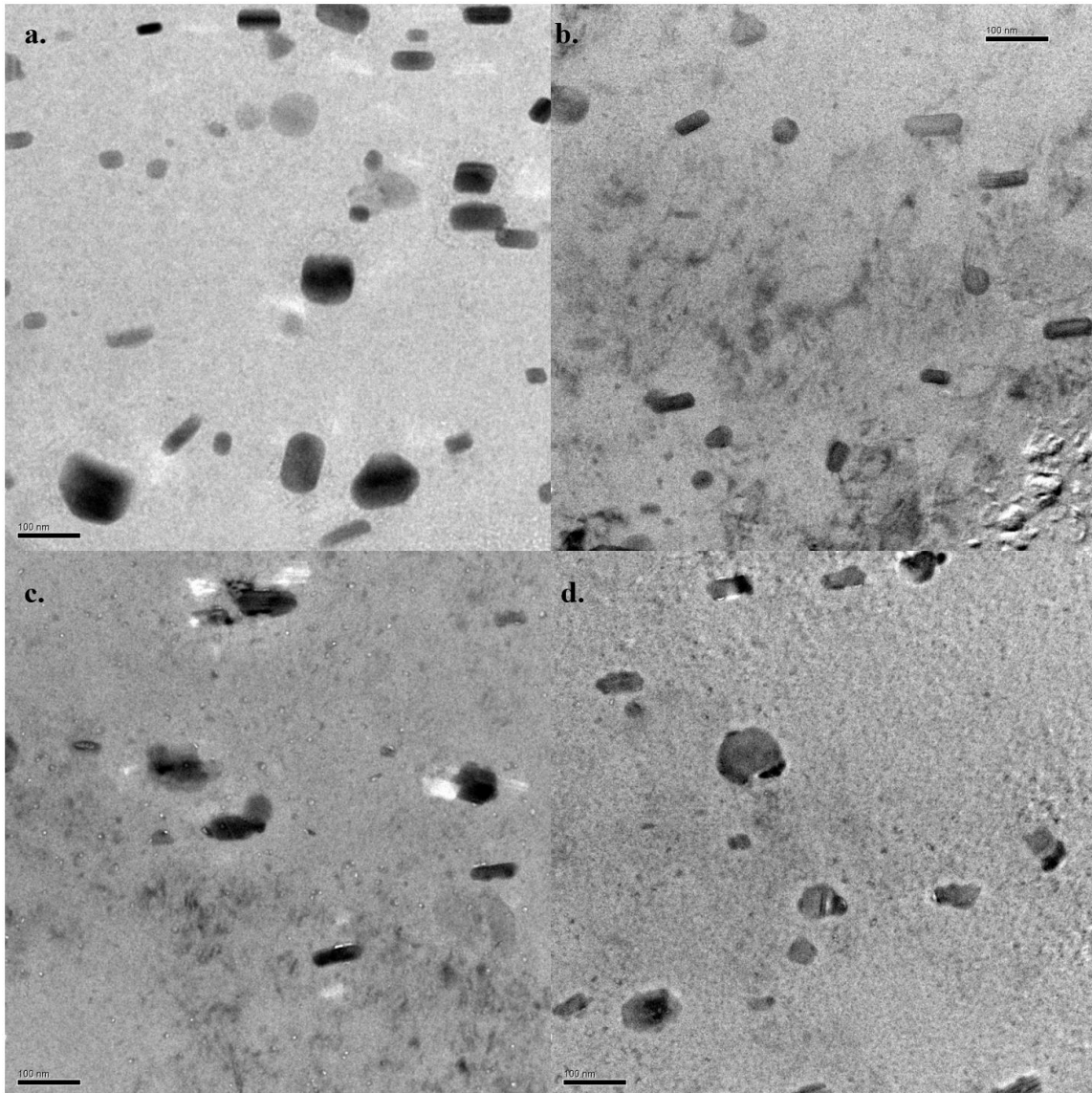


Figure 7-3: TEM images of precipitates from electrically-assisted tension conducted at a strain rate of 0.01/s, (a) as received, no deformation, (b) 15 A/mm² continuous, (c) 28CD1D3.5P, (d) 89CD0.3D10P

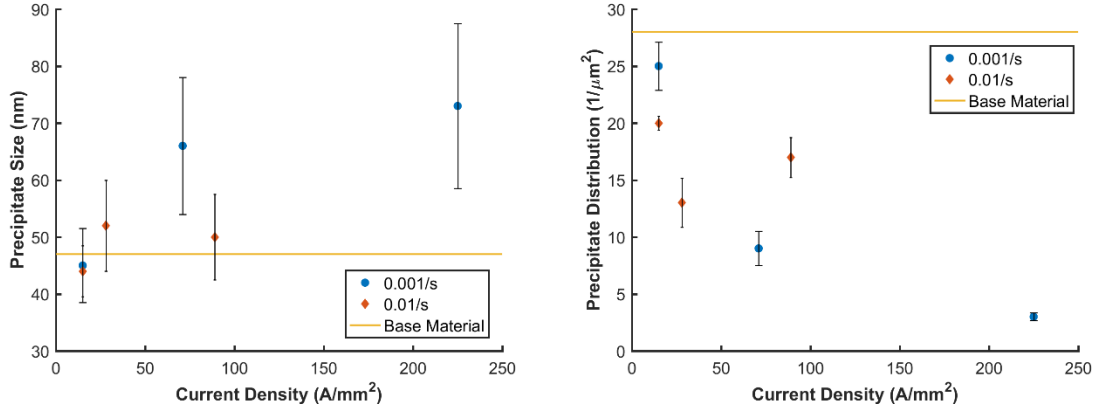


Figure 7-4: Precipitate size and distribution vs. current density, error bars represent 1 standard deviation

In order to determine if the effects of precipitate size and density change can be linked to other test results such as ductility, temperature, and stress, a trend analysis for linear and quadratic trends is conducted. The inputs of current density, energy, average temperature, and maximum temperature are correlated to outputs of precipitate size and density in Table 7-2.

Table 7-2: Correlations between inputs and process results on precipitate size and density, green highlight is applied to $R^2 > 0.65$

Linear R ² Fit Values		
	Precipitate Size	Precipitate Density
Current Density	0.73	0.68
Energy	0.31	0.16
Avg Temperature	0.00	0.01
Max Temperature	0.86	0.73
Quadratic R ² Fit Values		
	Precipitate Size	Precipitate Density
Current Density	0.74	0.74
Energy	0.33	0.20
Avg Temperature	0.00	0.16
Max Temperature	0.92	0.73

There is little difference between linear and quadratic fitting for the input variables studied, but interestingly, current density is better correlated to precipitate effects than energy; the complete opposite was true for predicting process results such as stress and temperature. Furthermore, energy had a good correlation with maximum temperature, and in Table 7-2 it is found that max temperature has the best correlation with precipitate effects, even though energy does not have a significant correlation. The linear result plots for precipitate size and density are shown in Figure 7-5. The trends match expectations: increasing maximum temperature will cause either overaging or solution of the precipitates, which in turn reduces the precipitate density and increases the size of remaining precipitates.

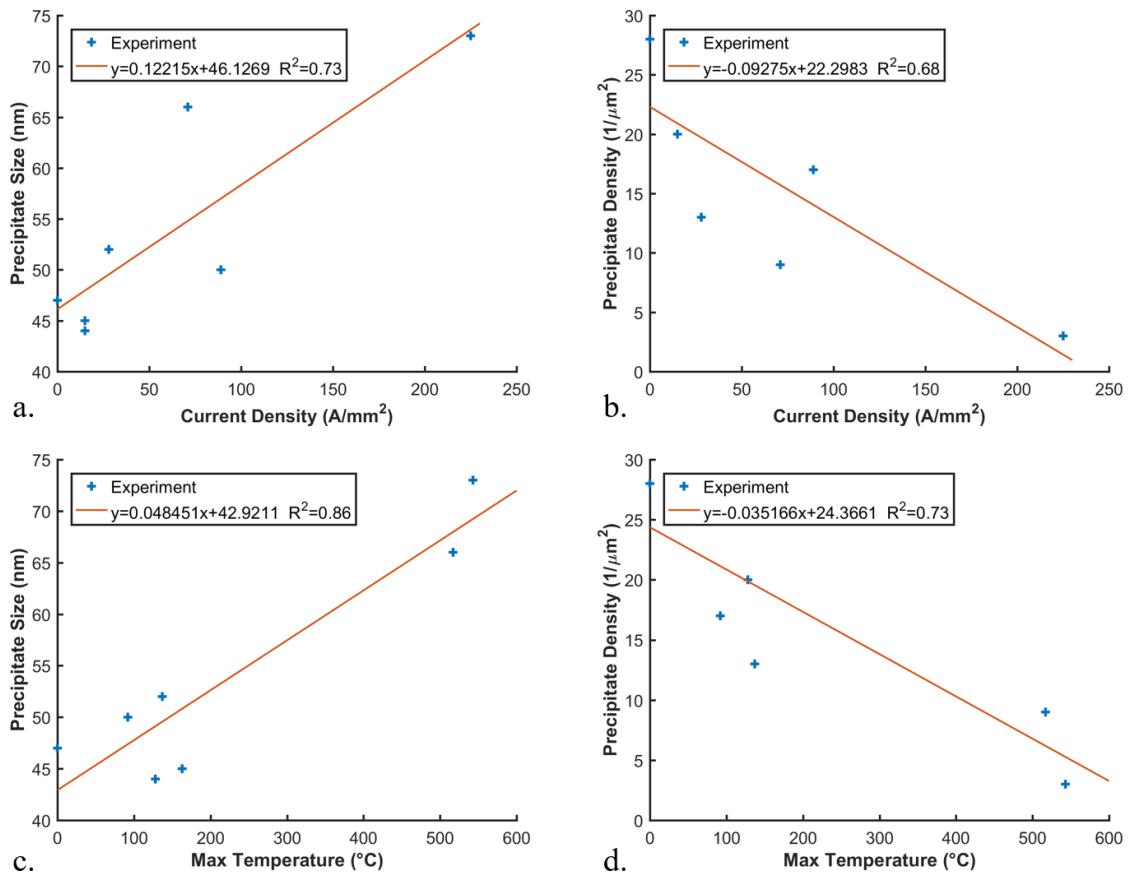


Figure 7-5: Correlation plots from trend analysis for precipitate size and density vs maximum temperature and current density

However, this analysis does not supply an answer to identify the differences between the 226CD and 71CD case, which had near the same temperature but different precipitate density. While both reached the same temperature and had near the same precipitate size (10% larger for 226CD), the precipitate density for the 226CD case was 67% lower than the 71CD case. As such, it is concluded that current density has an additional non-thermal impact on precipitate density while the precipitate size is likely thermally governed. The high temperature achieved by these two cases can cause solution or melting of the zinc-magnesium precipitates back into the solid solution of the aluminum.

This is likely why precipitate size and distribution showed the greatest correlation with maximum temperature. At high temperatures the precipitates melt, reducing the precipitate density. While current density may cause higher temperatures, this will only occur if the pulse duration is long enough to generate the required heat. However, the rate at which precipitates solutionized with the 226CD case is much faster than what is industrially accepted/used. For the 7075 alloy, solutionization is done at 465-490°C with a soak time of 30 minutes for a 1mm thick plate [110]. While the 226CD case did not achieve full solutionization (there were still precipitates) it did drastically accelerate the process, removing almost all precipitates with a 0.3 second pulse. As such, electrically-assisted pulsing may be able to reduce solutionization time and energy consumption in the aluminum manufacturing industry. Ideally this would be done by using a large current density initial pulse, such as a 226A/mm² pulse for 0.3 seconds. After the 0.3 seconds, the current density would be drastically reduced, to roughly 15A/mm² or lower to maintain the elevated temperature from the initial pulse without causing melting. In addition, this research has shown that higher current density pulses tend to deviate more from thermal response, meaning that a higher current density will likely dissolve precipitates at a higher rate than a low current density test that relies heavily on thermal effects.

In Chapter 5, it was suggested that the solution of precipitates may account for the error seen in the bulk model. As the precipitates dissolve back into solution, the matrix becomes over-saturated with alloying elements. In aluminum, these are substitutional alloys, meaning they take the spots of aluminum atoms in the lattice. This places more ion cores and obstacles in the lattice which impede electron flow, resulting in increased

electrical resistivity. However, since the 71CD test was accurately predicted and it had a lower precipitate density than the as-received or lower current density tests, it is concluded that precipitate effects cannot fully account for the loss of accuracy in the bulk model. It may instead be linked to the number of electrons attempting to move through the lattice. If there is a large current density, then the drift velocity and amount of electrons moving towards ground is greater which will result in more collisions and energy loss, resulting in increased electrical resistivity.

Conclusions

This section examined the effect of electricity on precipitation in the 7075-T6 alloy/temper. Various electrical treatments are studied and their precipitates measured using a TEM to determine if non-thermal precipitate effects exist. The following conclusions were drawn:

- Precipitation effects do not appear to be fully responsible for the transition from strain hardening to strain weakening in 15A/mm² continuous current application at a 0.001/s strain rate; the precipitate size and density was similar to the as-received undeformed material.
- Electricity has a larger impact on the density of precipitates whereas the size is thermally dominated. Two electrical tests, 225CD0.3D60P and 71CD3D60P reached approximately the same maximum temperature and had similar precipitate size, but the 225CD test had 67% lower precipitate density, suggesting that electricity reduces precipitate density beyond what is explainable using thermal mechanisms.
- Electricity shows promise for reducing solutionization time in aluminum alloys. The conventional furnace heating process requires heating 7xxx alloys to near 500°C for 30

minutes. Near full solutionization was found using 225CD0.3D60P. An industrial viable method would use a high current density to maximize electrical effects up until near 500°C, at which points the current density would be reduced to maintain the elevated temperature without melting the part.

- Precipitate effects are likely not solely accountable for the loss of accuracy of the bulk model due to a theorized increase in electrical resistivity

CHAPTER EIGHT

8. THE ELECTROPLASTIC EFFECT AT ELEVATED STRAIN RATE

Kinsey *et al.* determined that there was an absence of the electroplastic effect in steel and titanium at high strain rate (1000/s) [70]. Most work in the field of EAM focuses on quasi-static strain rates. This section examines the electroplastic effect at elevated strain rate, 0.001-1/s for 7075-T6 aluminum.

Experimental Setup and Control

A 50kN Instron 8801 servo-hydraulic tension/compression machine is used to deform 7075-T6 aluminum ASTM E8 specimens at varying strain rates ranging from 0.001-1/s, shown in Table 8 1, 3 replications are conducted for each parameter set. The specimens are deformed parallel to the roll direction. The specimens were painted black for thermal imaging with a FLIR A8201sc thermal camera. This camera is much higher resolution than the A40 used in previous sections, a comparison between the cameras is shown in Table 8 2. The A40 is an older technology known as a microbolometer, this technology works similar to thermal couples. Each pixel has a thermal response time constant which puts a limit on how fast the camera can sample, the maximum for this technology is 30Hz, though the A40 used in this research was maxed at 25Hz. The A8201 uses photon counting technology, as photons are received by the lens, each pixel releases an electron to a capacitor bank, the voltage across the capacitor is read to determine temperature, this technology can sample upwards of 4kHz when windowed down (using only a portion of the resolution). The end result is a crisper picture with more data points

due to higher sampling rate, with this technology, it was possible to capture thermal images at the onset of arcing, shown in Figure 8 1.

Table 8-1: Current density used for each strain rate tested

Current Density (A/mm ²)	Strain Rates Tested		
200	1	0.01	-
125	1	0.01	-
85	0.01	-	-
50	1	0.01	0.001
35	0.01	-	-
20	0.01	0.001	-

Table 8-2: Thermal camera comparison

	A40	A8201sc
Max Frame Rate Used (Hz)	25	135
Resolution (pixels)	320x240	1024x1024
Max Temperature (°C)	580	650

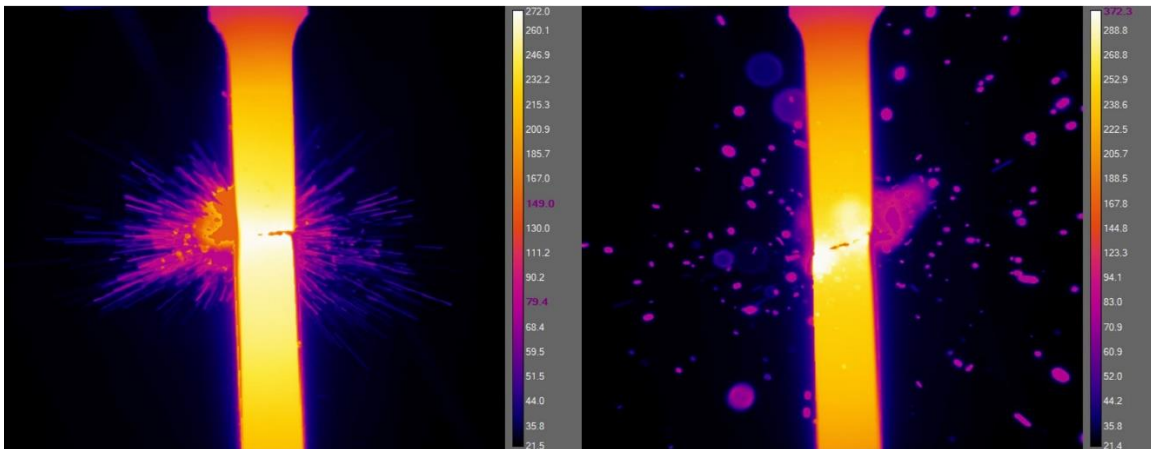


Figure 8-1: Images captured at the onset of arcing due to specimen fracture, A8201sc

The Existence of the Electroplastic Effect at High Strain Rate

Experimental stress/strain results for each of the 4 strain rates tested are shown in Figure 8-2. The same trend as found in the literature is found for the 0.001 and 0.01/s strain rates [24; 26; 59], continuous current application leads to reduced ductility due to overheating of the necking zone; an example image of this is shown in Figure 8-3. In the cases of 0.1 and 1/s strain rates, the large currents used had the potential to cause spectacular failure when cracks propagated; sample images are shown in Figure 8-4. However, due to the test time of the 1/s strain rate (0.2 seconds), the power supply was not able to react fast enough, resulting in late application of electric current and a limit to the effectiveness of the electrical pulse. This can be observed in Figure 8-2, where the electricity seems to have started near 15% strain, whereas in each other case the electricity was started before 5% strain. At 200 A/mm² and 125 A/mm² a ductility increase of 2% was observed, showing that there is an electroplastic effect at elevated strain rate (see Table 8-3); if the electric current had fired earlier the effect may have been more beneficial. The 0.1/s strain rate had the greatest impact from current. The short test time (2 seconds) coupled with the higher current densities resulted in ductility improvements of 6% over the baseline, a 30% improvement in ductility, once again showing that the electroplastic effect exists at elevated strain rate. Many of the electrical pulses pushed the temperature to near the melting point of the aluminum; many exceeded the melting point at the instant of arcing.

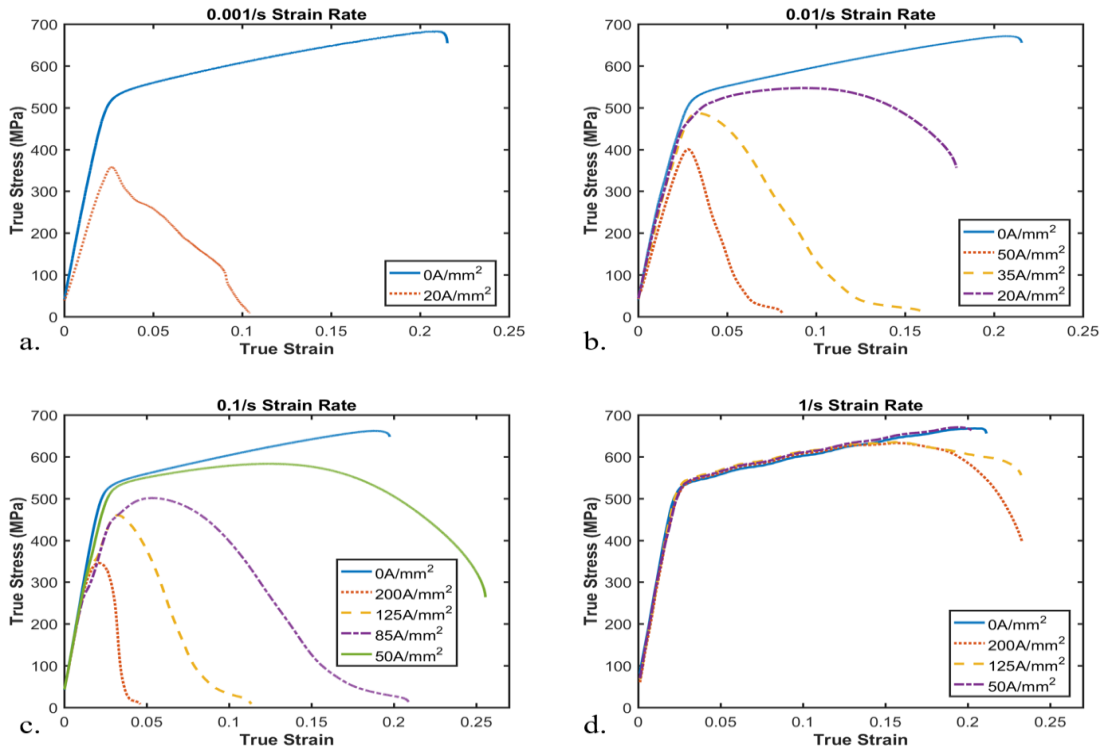


Figure 8-2: Stress-strain results from elevated strain rate testing (a) 0.001/s, (b) 0.01/s, (c) 0.1/s, (d) 1/s

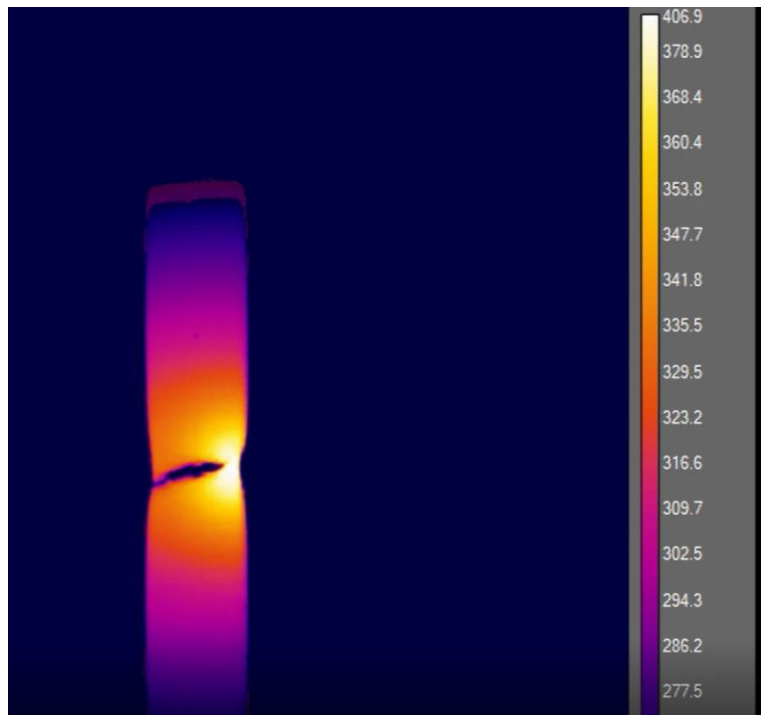


Figure 8-3: Overheating of the necking/fracture zone at 0.001/s strain rate

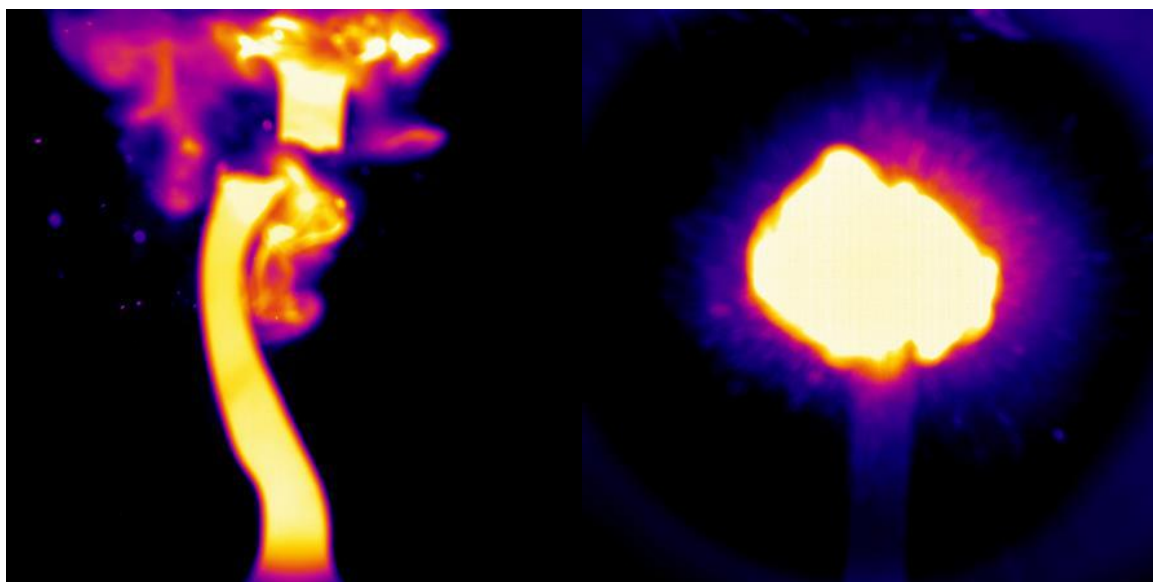


Figure 8-4: Explosive arcing during specimen failure, (left) 200A/mm² 0.1/s, (right) 200A/mm² 1/s

Table 8-3: Tabular results from elevated strain rate tensile testing

1/s Strain Rate			
Current Density (A/mm ²)	Average Stress (MPa)	Max Temperature (°C)	Ductility (%)
0	582	57	21
200	561	645	23
125	572	640	23
50	583	376	20
0.1/s Strain Rate			
Current Density (A/mm ²)	Average Stress (MPa)	Max Temperature (°C)	Ductility (%)
0	571	55	20
200	219	641	5
125	230	637	11
85	216	615	21
50	501	316	26
0.01/s Strain Rate			
Current Density (A/mm ²)	Average Stress (MPa)	Max Temperature (°C)	Ductility (%)
0	571	48	21
50	181	635	8
35	214	618	16
20	475	210	18
0.001/s Strain Rate			
Current Density (A/mm ²)	Average Stress (MPa)	Max Temperature (°C)	Ductility (%)
0	587	33	23
20	222	537	10

Kinsey *et al.* stated that the electroplastic effect did not exist at high strain rate (1000/s) through Kolsky bar electrically-assisted tension of 304 stainless steel and Ti-6Al-4V titanium with current densities of up to 90 and 100 A/mm², respectively [70]. However, for the 7075 aluminum discussed in this chapter, a current density of 125 A/mm² or higher was required to see a positive electroplastic effect at a strain rate of 1/s, which is 1000 times lower than what was used by Kinsey. However, aluminum is less resistive than both steel

and aluminum. If compared to current densities used in the quasi-static range (0.001/s) then aluminum for continuous current would be near or less than 20 A/mm². As such, a linear relationship can be described using the 0.001/s quasi-static case and the 1/s elevated strain rate case (125 A/mm²). This predicts that a current density of 105kA/mm² is required to see an effect at a strain rate of 1000/s. This is 5250 times higher than the quasi static current density. If this similar factor is used for steel, which would have a quasi-static current density closer to 10A/mm², then the required current density at 1000/s strain rate for a positive effect would be on the order of 52kA/mm², much higher than what was tested by Kinsey. The electric current requires time to build up an effect, as explained using the theory presented in Chapter 6. It is also worth noting that a current density of 50A/mm² at a strain rate of 1/s did not have any effect (Figure 8-2), showing that too low of a current density could erroneously lead to the conclusion of a lack of the electroplastic effect. The author conjectures instead that the electroplastic effect does exist at high strain rate assuming a large enough current density is used.

Conclusion

This chapter examined the electroplastic effect at elevated strain rates to compare with work from the literature that claimed there was no electroplastic effect at high strain rate. Current densities ranging from 0-200A/mm² were applied to 7075-T6 aluminum deformed at strain rates ranging from 0.001-1/s. The following conclusions were drawn:

- The electroplastic effect does exist at a high strain rate, so long as a large enough current density is used to cause an effect. A 30% increase in ductility was observed at 0.1/s strain rate, and a 10% increase in ductility was observed at 1/s strain rate.

- It is essential that the power supply be able to react fast enough to apply current at an early strain in high strain rate cases, the 1/s strain rate case suffered from late electrical application, near 15% strain, resulting in reduced effects
- It is likely that the literature showing no electroplastic effect at 1000/s strain rate did not use a high enough current density; a maximum of 100A/mm² was used on grade 5 titanium.

CHAPTER NINE

9. ELECTRICALLY-ASSISTED DRILLING

Electrically-assisted Machining

Only a few papers exist on the topic of electrically-assisted machining. The first work was a theoretical study of an electroplastic drilling process [111]. It was proposed that an electroplastic drilling process could reduce the friction force by upwards of 30%, a number which is conservative compared to existing experimental papers. Jones *et al.* showed that cutting forces could be reduced by up to 60% in orthogonal cutting of A2 steel with a continuous current ranging between 800- 900A [112]. Similar results were found by Ulutan *et al.* in electroplastic turning of grade 5 titanium and Inconel 718, where up to 70% force reduction was achieved, however, they showed that if enough electric current was applied to the workpiece, the cutting force would increase compared to the no electrical assistance condition [8]. Egea *et al.* were the first researchers to test a pulsed current (a technique typically used in tensile deformation to avoid overheating a necking region) in electrically-assisted machining [113]. A 90A square wave with a pulse duration ranging from 50-200 μ sec and a frequency of 100-300 Hz was applied to SAE 1020, 1045, and 4140 steels. In this case it was found that the specific cutting energy and hardness decreases accompany an increase in surface quality.

The objective of this work is to offer the first in-depth experimental investigation of electroplastic drilling through the use of a generalized factorial design of experiments (DoE) study conducted on low-carbon 1008 CR steel. The knowledge from this DoE is applied to high feedrate drilling of 1500MPa Press Hardened Steel (PHS1500) often used in the automotive industry, where extreme strength is required (*e.g.*, B-pillar inner layer

material). A simple force and temperature prediction model based on Merchant's machining model for electroplastic drilling are presented, and its performance evaluated in different drilling conditions to show its limitations and areas for future improvement.

Experimental Setup

All testing in this work was conducted using 6.35mm twist drill bits. Black oxide steel bits with 135° point angle were used for drilling 1008CR steel with workpiece dimension of 31.75×63.5×1.4mm, while tungsten carbide-tipped steel bits with a point angle of 117° were used for drilling PHS1500 steel (since the black oxide is unable to cut the PHS1500). The top surface of each workpiece was painted black prior to cutting to replicate a black body for temperature acquisition via a FLIR A40 thermal camera thermal camera, sampling at 12-25 Hz. A knee mill was used with a servomotor to control feedrate during the drilling process. Electricity was applied via a Darrah 4kA power supply controlled through LabVIEW software, and tool wear was measured using a Dino-lite microscope with 40× magnification.

The axial force was recorded using a 1kN Interface loadcell. The electricity was started and stopped using a load trigger. When the force from the load cell was greater than 66N for 1008 steel or 333N for PHS1500, electricity was applied, and when the force fell below these values, the electricity was stopped. A higher force was used for the PHS1500 to ensure sufficient tool contact area to avoid arcing for the steeper tipped tool and stronger material. Temperature and force data were filtered using a 10-point moving average prior to plotting and analysis. The experimental setup is shown in Figure 9-1.

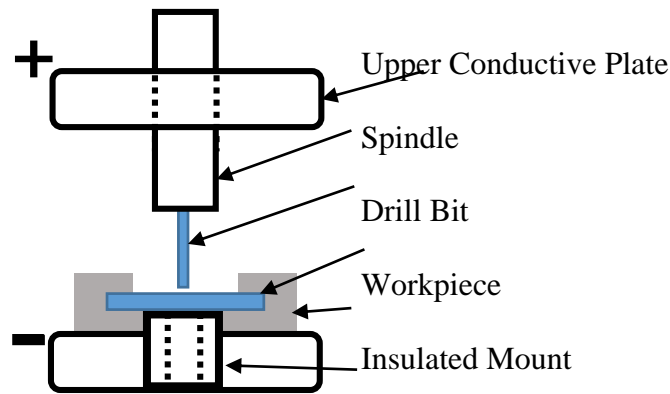


Figure 9-1: Schematic of an electrically-assisted drilling setup

Design of Experiments for 1008CR Steel

A 4-factor generalized DoE was used to determine the impact of the input process parameters on electrically-assisted drilling of 1008CR steel. The inputs used were spindle speed (RPM), feedrate (mm/min), current (A), and the number of holes made. Both current and number of holes have 3 levels for their given factors, while both spindle speed and feedrate have 2 levels, shown in Table 9-1. The DoE resulted in 36 individual parameter sets, each replicated 3 times, for a total of 108 tests. The outputs studied were maximum part temperature ($^{\circ}\text{C}$), average flank wear (mm), and maximum axial force (N).

Table 9-1: Inputs and outputs for DoE for 1008CR steel

Factors	Level 1	Level 2	Level 3
Feedrate (mm/min)	12.5	25.4	-
Current (A)	0	150	300
Spindle RPM	350	560	-
Number of Holes	1	2	3
Experimental Outputs			
Maximum Temperature ($^{\circ}\text{C}$)			
Maximum Axial Drilling Force (N)			
Average Flank Wear (mm)			

Axial Force

The primary effects plot (see Figure 9-2), shows that electric current level has the strongest impact on the axial force observed during the drilling process of 1008CR Steel. However, the effect of current magnitude shows a nonlinear behavior. At a current of 150A, a slight force reduction is found, while at a current of 300A a large axial force increase of 41% is observed compared to the no-current condition. This is caused by arcing at the initial application of electricity, suggesting that the 66N preload was not sufficient for the 300A 1st cut test. The arcing dulls the tool by removing the chisel edge (top cutting edge) as well as damaging the helix cutting edge, which can be seen in the tool wear images shown in Table 9-2. The underlying reason for arcing can be explained by considering the voltage of the (current driving) power supply, which is determined based on the requested current. Therefore, for each of the 300A tests, a higher voltage was supplied than the 150A tests, which gives a greater potential to overcome air and contact resistance and therefore induce arcing.

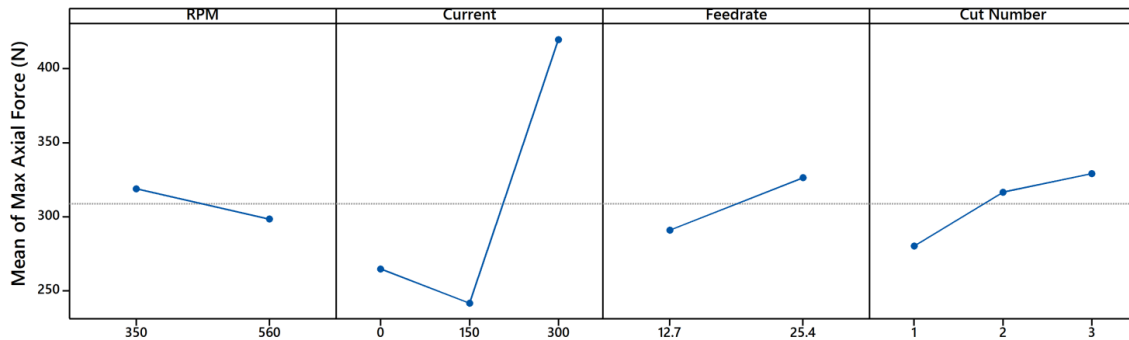

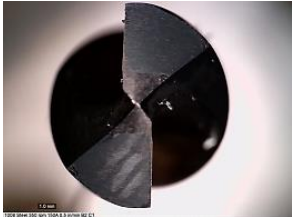

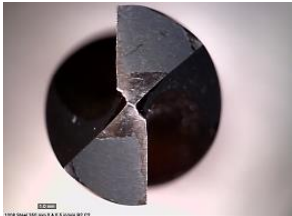
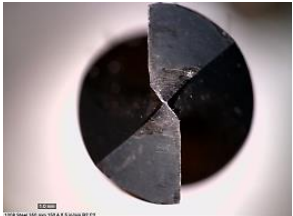
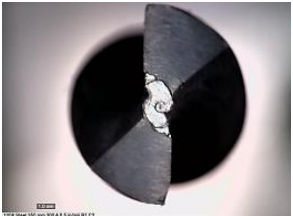
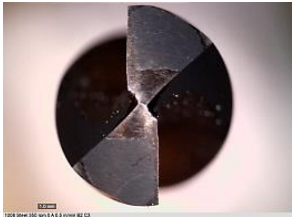
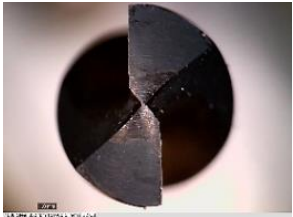



Figure 9-2: Main effects plot for axial force during EA drilling of 1008CR steel

Table 9-2: Tool wear images for EA drilling of 1008CR steel at 350RPM and 12.7mm/min

Cut Number	Electric Current (A)		
	0	150	300
1			
			
			

Increasing feedrate will increase the cutting force, while increasing the rotational surface speed will decrease the cutting force. This can be explained by examining the shear area (discussed in the modeling section of this chapter), where increasing the rotational speed decreases the chip thickness, resulting in a smaller shear area. Increasing feedrate will increase the chip thickness, and higher force will be observed as more material is removed per rotation of the tool. Increasing the number of cuts per tool increases the forces as the cutting edges start to wear out during each cut. An example is shown in Figure 9-3 for a 300A test. The temperature is the highest in the first cut since the tool is still sharp,

leading to a smaller contact area and higher current density, coupled with arcing at the initial application of current.

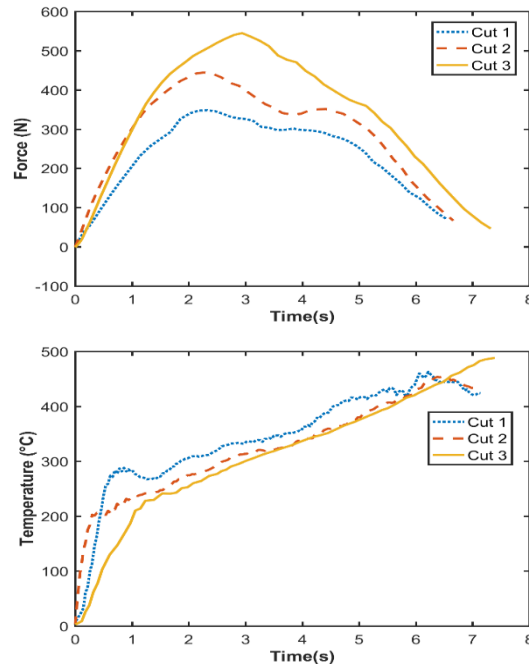


Figure 9-3: Axial force and temperature comparison for 3 sequential drilling operations conducted at 300A, 350RPM, and 25.4mm/min

Maximum Temperature

Similar to force, current is the dominant input parameter affecting maximum temperature, as shown in Figure 9-4. The effect is nonlinear, as current is increased from 0A to 150A, an average temperature increase of 100°C is observed. However, when the current is raised to 300A, the temperature rises to around 400°C. A large portion of the nonlinearity is likely due to arcing in the 300A tests. The difference in temperatures between parameter sets is shown for the 1st cut comparisons in Figure 9-5. Without electricity, feedrate appears as the dominant heating parameter (0A test). However, with current, higher temperatures is observed from lower feedrates due to smaller shear area

resulting in a higher current density. It is worth mentioning that when current is present, all other parameters have a negligible effect on the process temperature.

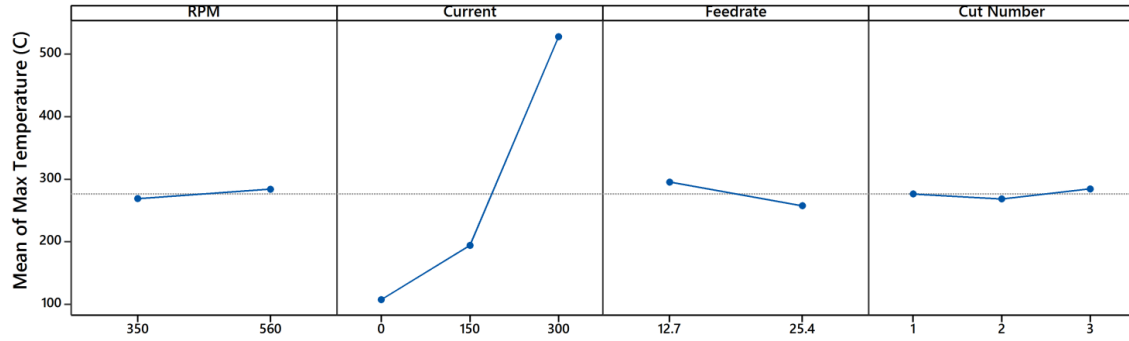


Figure 9-4: Main effects plot for maximum temperature in EA drilling of 1008CR steel

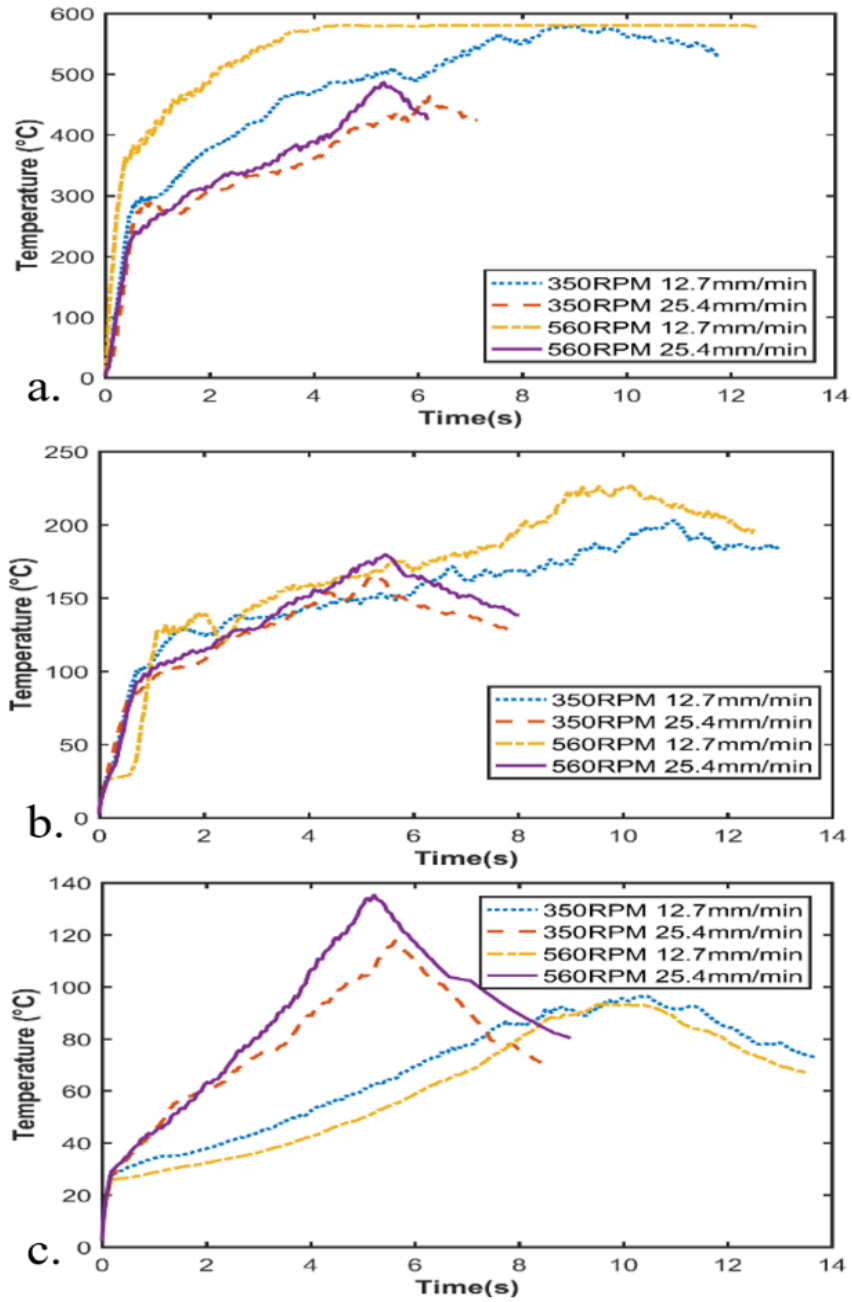


Figure 9-5: Temperature comparison for (a) 300A, (b) 150A, and (c) 0A in different drilling conditions of 1008CR steel

Average Flank Wear

Flank wear is measured at 5 locations on each cutting edge and then averaged to obtain the reported flank wear value. According to Figure 9-6, electric current is the dominant factor in determining average flank wear.

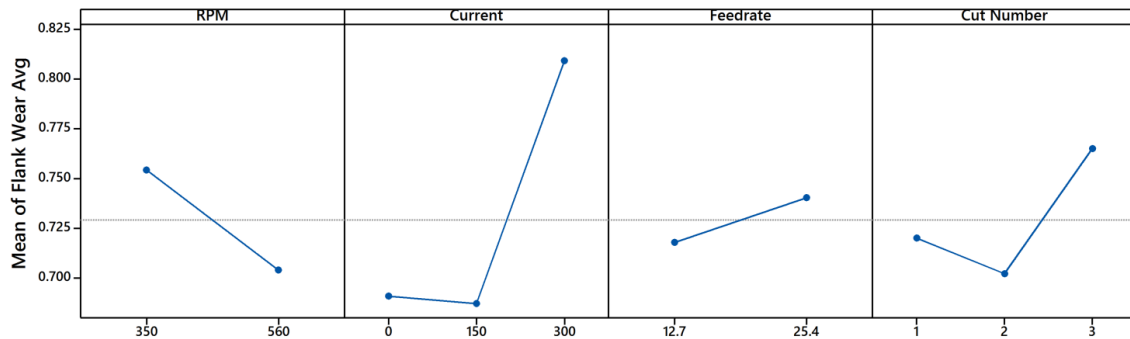


Figure 9-6: Main effects plot for average flank wear in EA drilling of 1008CR steel

Here, the conclusions are similar to force: increasing the electric current to 150A yields a small decrease in flank wear while using 300A electric current causes a large increase, due to softening and arcing effects. However, a potential error exists in the measurement of flank wear. As shown in Table 9-2 for some tests it is difficult to determine the worn area of the flank face, especially on sequential cuts in the 300A test. The error appears in the cut number results where flank wear decreases from cut 1 to cut 2, which is not physically possible. The effect of electricity on tool life is explored later in this paper through testing-to-failure on PHS1500 steel.

Model of Electrically-assisted Drilling

Merchant's model [114] is used to compute axial cutting forces for comparison with experiment. First, the shear force is computed using the Johnson-Cook plasticity model, which is strain rate and temperature dependent. Strain rate is computed through the material

models found in the literature [115], and temperature is computed via a 2D finite volume heat transfer model. The formulation and integration of these models are described as follows.

To predict temperature a 2D explicit finite volume heat transfer model was constructed with a time step of 0.01s, less than the required 0.0375s step time for stability calculated using the Fourier number. A nodal spacing of 1.5mm is used in both the x and y directions to mesh a workpiece with dimensions of 63.5×31.8mm, as shown in Figure 9-7.

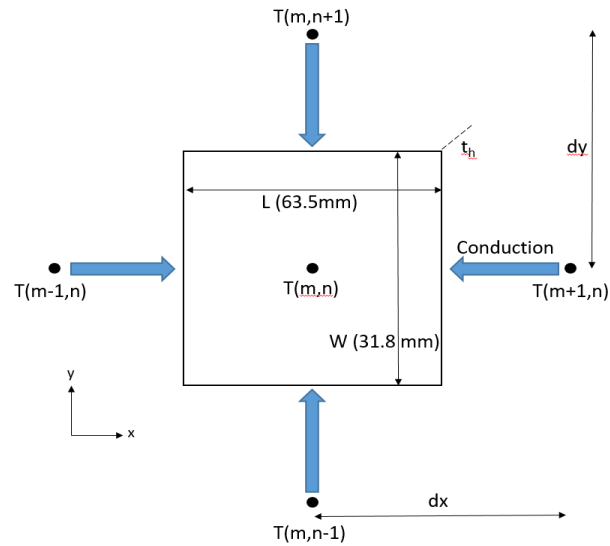


Figure 9-7: Example of nodal setup for a single element in 2D explicit finite volume heat transfer model, viewed from the top

Convection conditions are placed on the top face and outside width edges of the workpiece, and a convection coefficient of 25 W/m²K is applied, while the bottom and length edges of the workpiece are insulated due to contact with a Delrin plastic fixture. An energy

balance is used to calculate the temperature of the workpiece, with a point heat source composed of 3 heating terms applied at the center of the workpiece.

The 3 sources of heat are shear deformation, friction, and Joule heating. The Joule heat energy (Q_{elec}) added to the system is given by Equation 16, where I is electric current, t is time, T is temperature, and R is temperature dependent electrical resistance given in Equation 17, where ρ_e is electrical resistivity, L is the conduction length which is a length that electricity flows through for a given cross sectional area assumed equal to the shear area, A_{shear} .

$$Q_{elec} = I^2 R(T) t \quad (16)$$

$$R(T) = \frac{\rho_E(T)L}{A_{shear}(t)} \quad (17)$$

The frictional heating energy ($Q_{friction}$) model is shown in Equation 18, where μ is the coefficient of friction, τ_{FSS} is the fracture shear stress, r is radius of the tool in contact with the workpiece, λ is the percentage of heat that goes into the workpiece (assumed 50%) and ω is the angular velocity.

$$Q_{friction} = \lambda \mu \tau_{FSS}(T) \omega r A_{shear} t \quad (18)$$

The shear deformation energy (Q_{shear}) model is shown in Equation 19, where F_s is the shear force, and V_s is the shear velocity. The shear velocity is a function of average velocity (v) of the shear face found through the midpoint radius multiplied by the angular velocity and the shear plane angle (ϕ), as in Equation 20. The shear plane angle is a

function of friction angle (β) and the rake angle (α) assumed to be the helix angle for the drill bit, and is shown Equation 21. The friction angle is found using Equation 22. The shear force is found using the fracture shear stress and the shear area, Equation 23. The fracture shear stress is assumed equal to the half of the calculated fracture tensile stress using the Johnson-Cook plasticity model using Equation 24, where A is the yield stress, B is the strength coefficient, $\epsilon_{fracture}$ is the fracture strain, n is the strain hardening exponent, C is strain rate sensitivity coefficient, $\dot{\epsilon}$ is the strain rate, $\dot{\epsilon}_0$ is the reference strain rate, T^* is the homologous temperature and m is the temperature sensitivity exponent. The Johnson-Cook parameters for mild steel from the literature are given in Table 9-3 [116].

Table 9-3: Johnson-Cook plasticity model parameters for mild steel

Parameter	Value (units)
A	217 MPa
B	233 MPa
C	0.0756
n	0.6428
m	1

$$Q_{shear} = \lambda F_s V_s t \quad (19)$$

$$V_s = \frac{v}{\cos(\phi)} \quad (20)$$

$$\phi = \frac{90 + \alpha - \beta}{2} \quad (21)$$

$$\beta = \arctan(\mu) \quad (22)$$

$$F_s(t) = \tau_{FSS} A_{shear}(t) \quad (23)$$

$$\sigma = (A + B\varepsilon_{fracture}^n) \left(1 + C \ln \left(\frac{\dot{\varepsilon}}{\dot{\varepsilon}_0} \right) \right) (1 - T^{*m}) \quad (24)$$

The shear strain rate ($\dot{\gamma}$) was calculated using Equation 25, where a_h is the hyperbola curvature constant found using Equation 26, with C_{sr} as a material constant [115].

$$\dot{\gamma} = \frac{v}{(4\sqrt{a_h} \sin^2(\phi) [\tan(\alpha) + \cot(\phi)]^{1.5})} \quad (25)$$

$$a_h = \frac{t_1^2}{(16C_{sr}^2 \sin^4(\phi) [\tan(\alpha) + \cot(\phi)])} \quad (26)$$

The shear face area is found using Equation 27, which represents the area of contact between the bit's cutting edges and the workpiece [117; 118], where a is the uncut chip thickness, D is the tool diameter in contact with the workpiece at a given time, d_0 is the chisel edge diameter and ϕ is half of the bit point angle. The chip thickness is found using Equation 28, where f is the feed (mm/rev).

$$A_{shear}(t) = \frac{a(D(t) - d_0)}{\cos(90 - \phi) \sin(\phi)} \quad (27)$$

$$a = \frac{f \sin(\phi)}{2} \quad (28)$$

This paper examines the drilling of thin sheets (1.5mm) as such the contact between the bit and workpiece is continually changing and can be broken into 4 segments for the given bit and workpiece thickness combination, which is outlined in Figure 9-8.

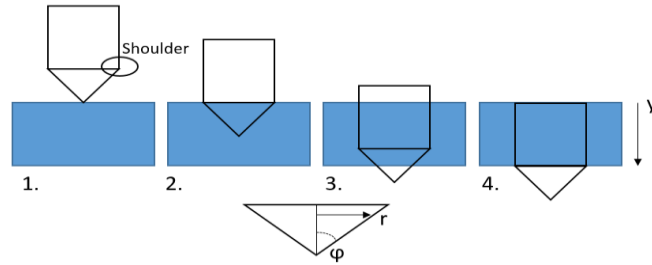


Figure 9-8: Contact segments for drilling of thin sheets where tapered bit length is less than the sheet thickness

The 1st segment is when the tapered portion of the bit is in contact with the workpiece but the shoulder has not yet touched, the 2nd segment has shoulder contact but the tip of the bit has not yet left the workpiece, the 3rd segment is when the tip of the bit leaves the bottom of the workpiece but the shoulder continues cutting, and the 4th segment is the end of the cut when the bit shoulder penetrates through the bottom of the sheet. If the tapered portion of the bit is longer than the thickness of the sheet, then the 2nd segment would be skipped.

The diameter in contact with the workpiece for the first segment is shown in Equation 29, where f_r is feedrate. The second segment uses the nominal bit diameter since the shoulder and cutting edges are both fully in contact. The third segment subtracts the protruding diameter from the nominal diameter. The protruding diameter is calculated using Equation 30, where *thick* is the thickness of the workpiece. Finally, the fourth segment has no diameter contact as the cut is complete.

$$D(t) = 2r(t) = 2f_r t * \tan(\varphi) \quad (29)$$

$$D_{protrude} = 2r_{protrude} = 2(f_r t - thick) \tan(\varphi) \quad (30)$$

The axial force relation, shown in Equation 31, is calculated using angular relations of the bit and shear zone from Merchant's model [114] with the shear force calculated plugged in from Equation 23.

$$F_{axial} = \frac{F_{shear}}{\cos(\beta - \alpha + \phi)} \quad (31)$$

The assumptions for solving the model are listed below:

- Constant friction coefficient, not a function of temperature, pressure, or velocity
- Conduction length of electricity remains constant
- Electricity flows uniformly through the shear area
- 50% of heat generated by mechanical shearing and friction goes to the workpiece and the other 50% to the tool, and steel on steel contact
- 100% of electricity goes to Joule heating
- Fracture shear stress can be approximated as 50% of the fracture tensile stress for 1008CR steel
- Hyperbola shape constant, $C_{sr}=6$
- Rake angle=helix angle=30°
- Point angle=135°, based on manufacturer specification
- No tool deformation, and no tool wear

The model has the following tuneable parameters:

1. Friction coefficient found to be 0.6 by fitting model to 0A tests
2. Fracture strain varied between 1-9 for Johnson-Cook model, fit to 0A tests, found to be within 1-10 range given by [103]

3. Conduction length of electricity at tool-workpiece interface assumed to be 0.5mm through the shear area, derived based on fitting model to 150A tests

Electroplastic Drilling Model Evaluation, Limitations, and Suggestions

The formulated model is used to predict temperature and axial force during the first cut of an electrically-assisted drilling process. Comparisons between model and experiment are shown for each parameter set on the 1st cut for both axial force (see Table 9-4) and temperature (see

Table 9-5).

Table 9-4: Model accuracy results for maximum axial force during drilling of 1008CR steel across all parameter sets, underlines tests experienced arcing

Current (A)	RPM	Feedrate (mm/min)	Average Max Force (N)	Predicted Max Force (N)	Percent Error (%)
0	350	12.7	245	235	4%
0	350	25.4	312	304	3%
150	350	12.7	190	217	15%
150	350	25.4	260	295	14%
<u>300</u>	<u>350</u>	<u>12.7</u>	<u>331</u>	<u>76</u>	<u>77%</u>
<u>300</u>	<u>350</u>	<u>25.4</u>	<u>348</u>	<u>110</u>	<u>68%</u>
0	560	12.7	174	159	9%
0	560	25.4	264	243	8%
150	560	12.7	174	147	16%
150	560	25.4	242	236	3%
<u>300</u>	<u>560</u>	<u>12.7</u>	<u>400</u>	<u>42</u>	<u>89%</u>
<u>300</u>	<u>560</u>	<u>25.4</u>	<u>289</u>	<u>120</u>	<u>59%</u>

Table 9-5: Model accuracy results for maximum temperature during drilling of 1008CR steel across all parameter sets, underlines tests experienced arcing

Current (A)	RPM	Feedrate (mm/min)	Average Max Temp (°C)	Predicted Max Temp (°C)	Percent Error (%)
0	350	12.7	96	103	7%
0	350	25.4	118	117	1%
150	350	12.7:	203	198	3%
150	350	25.4	166	153	8%
<u>300</u>	<u>350</u>	<u>12.7</u>	<u>578</u>	<u>1044</u>	<u>81%</u>
<u>300</u>	<u>350</u>	<u>25.4</u>	<u>463</u>	<u>940</u>	<u>103%</u>
0	560	12.7	93	110	18%
0	560	25.4	135	146	8%
150	560	12.7	227	209	8%
150	560	25.4	180	183	2%
<u>300</u>	<u>560</u>	<u>12.7</u>	<u>580</u>	<u>1259</u>	<u>117%</u>
<u>300</u>	<u>560</u>	<u>25.4</u>	<u>487</u>	<u>1064</u>	<u>119%</u>

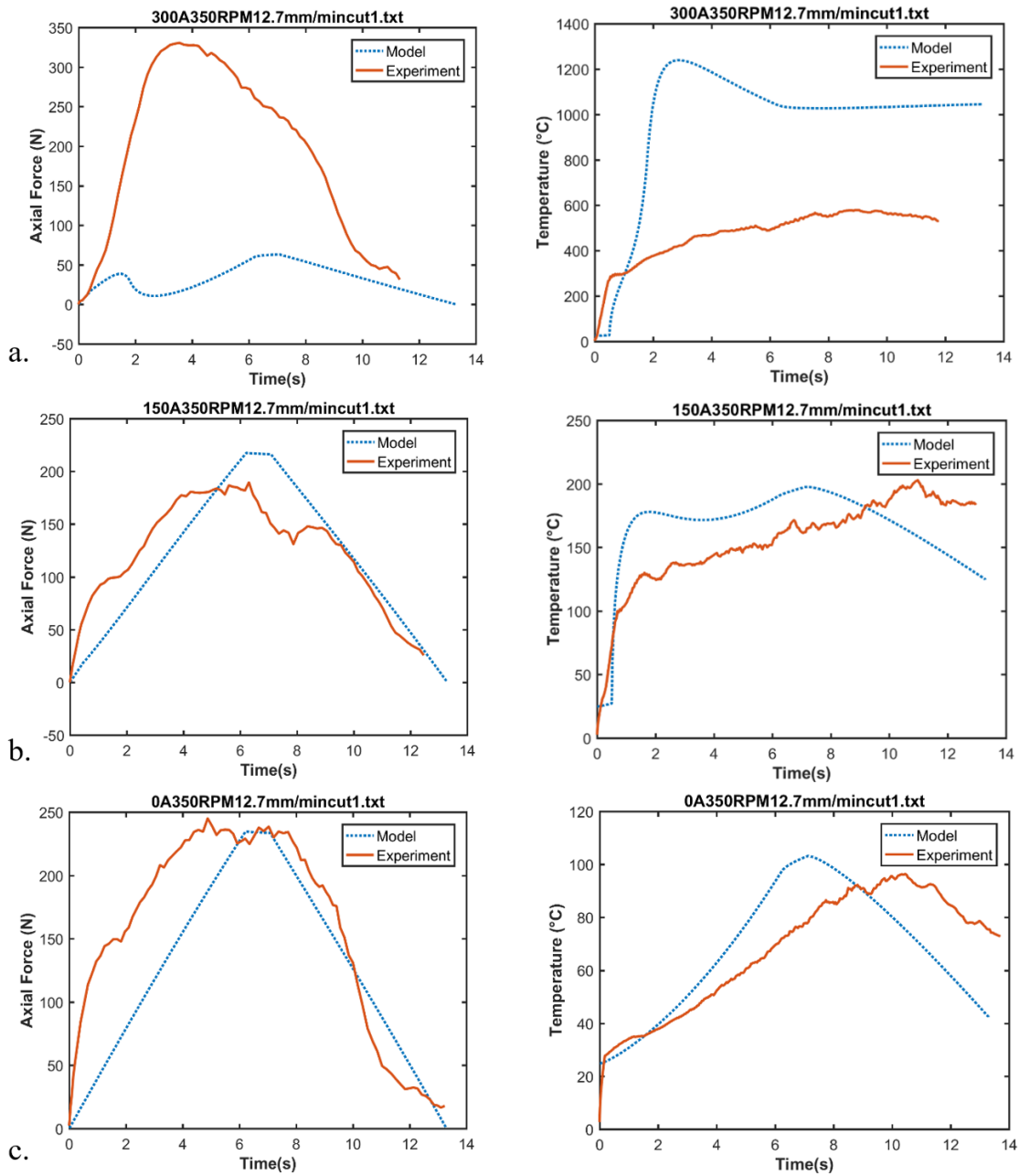


Figure 9-9: Model vs. experiment for maximum temperature and axial force during EA drilling process of 1008CR steel at 350RPM and 12.7mm/min for (a) 300A, (b) 150A, and (c) 0A

The temperature and axial force models' prediction is within 20% of experimental results of the 0A and 150A tests. However, the model deviates significantly for the 300A tests,

due to arcing. Arcing occurs at the onset of electric current and drastically changes the contact area between the workpiece and tool, Figure 9-9.

The model assumes an undeformed tool, but the 300A cases are severely deformed tools, even for the first cut; this deviation leads to a greater contact area between tool and workpiece in the experiment than predicted in the model. This resulted in a current density in the model higher than experiment, leading to a higher predicted temperature, correlated to a low axial force through a low material strength from the Johnson-Cook model. A large deviation between the shape of the model and experimental curves exists in Figure 9-9. This is from the electrical augmentation of the knee mill, which requires an electrical contact carrier to be held against the spindle using springs. The fixture slides along 4 guide rails but has a large copper cable connected to one side of the fixture resulting in eccentric rotation which transfers to the bit potentially causing the abnormal behavior. A comparison between the contour temperature plot results from the temperature prediction model and thermal camera data collection is shown in Figure 9-10. The given image is shown at the

end of drilling process, and it is found that the contours and magnitudes from the model are reasonable and resemble the experiment.

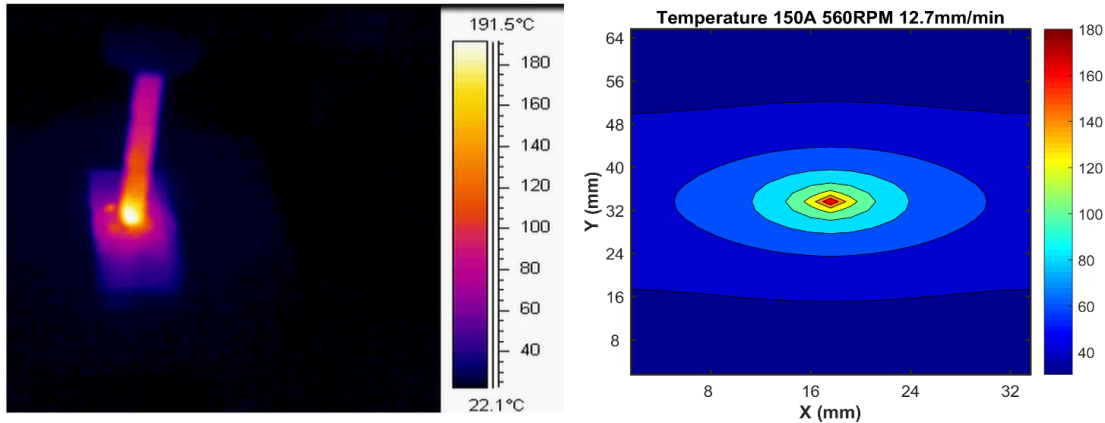


Figure 9-10: Temperature contour comparison between model and thermal camera experimental data for 1008CR steel

Most models are created with the potential promise of being used as predictors such that less experimentation is necessary to determine process parameters for a given process, in this case electroplastic drilling. However, this model cannot be used for prediction of process parameters and was unable to predict force and temperature for a parameter set outside of the tested parameter range used in this paper even without arcing. There are 3 main reasons conjectured, attributed to limitations in knowledge and technology that require further advancement before the proposed model could be used as a process output predictor.

1. The first factor is friction modeling. The current model took a simplified approach to friction and assumes a constant friction without dependency on temperature and pressure. While some temperature and pressure friction models exist, they are empirical in nature. The interaction between electricity and friction has not yet been

studied, making it difficult to use existing empirical models with any degree of certainty. In addition, a slight change to the friction coefficient has a significant effect on the model output since the shear plane angle which is used to calculate shear area and axial force is a function of friction angle which is derived from the friction coefficient, making the model highly sensitive to friction modeling.

2. The second issue is with the temperature measurement and model fitting (once again an issue with friction). The resolution of the thermal camera used in this work plays an important role in the accuracy of the temperature reading (see Figure 10(a)) compared to what the true maximum temperature is. The thermal camera works by dividing the given picture into a series of small regions, each captured by a pixel with average temperature of each as measurement results. However, even a high resolution thermal camera cannot clearly resolve the temperature at the tool-material interface, which essentially introduces a temperature reading error in the model. This error subsequently affects curve-fitting parameters for the drilling model. Please note that the temperature results can be used to compare different tests but finding the true maximum temperature in the drilling process is prone to error.
3. The third issue lies with the electrical conduction length, path, and current density resulting from the electrical flow. In this work, electricity flows through the tool, then into the workpiece, and grounds at an aluminum ring underneath the workpiece. A constant conduction length value was assumed for simplifying the model, however it will continually change. Determining the conduction length and resultant current density with good degree of accuracy would require a finite element simulation.

However, this too presents challenges. Per authors knowledge the commercialized finite element explicit solvers do not support thermal-electrical-structural elements which is traditionally used for machining simulation or high strain rate processes.

Effect of Electricity on Tungsten Carbide and its Implications on EA Machining

For 1008CR steel, black oxide steel drill bits were used, however, using a steel drill bit for electrically-assisted drilling of steel has some issues. The current density will have the same effect on both the part and drill bit since both will experience the same thermal softening mechanism and have about the same working temperature. This section examines the effect of electricity on tungsten carbide to determine if it is a better fit for EA drilling. Tungsten carbide's strength as a function of current density is examined in compression to see if there is a significant strength drop in the presence of electric current.

Methodology

Tungsten carbide (WC) specimens were cut from a single 4.7mm diameter rod to a length of 6.35mm using electro discharge machining. An Instron 1332 servo hydraulic machine was used to compress the specimens at a platen velocity of 1.5mm/min until fracture. A preload of 4.4kN was used to prevent arcing due to contact resistance as the electric current was turned on. Continuous current was applied to the specimens using a 4kA Darrah power supply. The current densities tested were 20, 30, 40, and 50 A/mm². Three trials of each test were conducted to ensure repeatability of the data. Hardened A2 steel dies with a hardness of 60 HRC were used for this testing. The dies had replaceable cylindrical inserts made from the same hardened steel. The strength of the WC required continual change out of the dies due to damage from both temperature and from

compression of the WC into the steel platens. The test setup and dies are shown in Figure 9-11; a summary of testing is shown in Table 9-6.

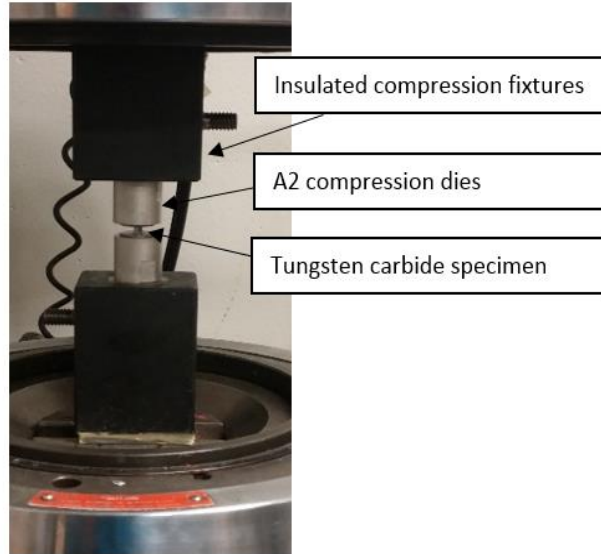


Figure 9-11: Compression dies used during testing

Table 9-6: Summary of testing

Test #	Current Density (A/mm ²)	Current
1-3	0	0
4-6	20	356
7-9	30	534
10-12	40	713
13-15	50	891

A high speed camera was used to capture fracture during the process for some of the tests, shown in Figure 9-12. Pictures of the specimens for testing are not possible due to the fracture shown in Figure 9-12. The compression fixtures and electrical leads were enclosed in a Plexiglas box to stop the chips from the extreme brittle fracture. Since the box had to be completely closed for safety purposes, thermal data was not gathered, as the thermal camera would only read the reflection off of the glass and the use of a thermocouple

would require reading the die rather than the part (part would melt the bead of the thermocouple at temperatures reached during testing).

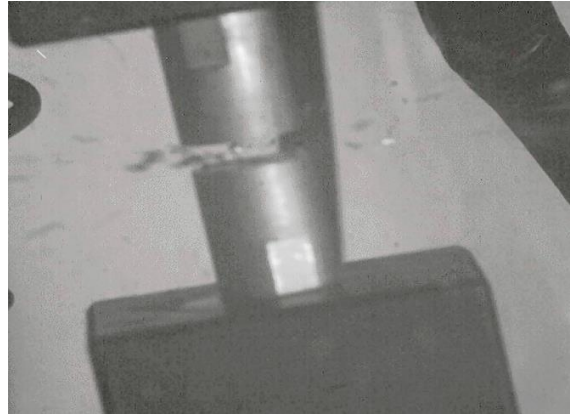


Figure 9-12: Brittle fracture of WC in compression

Results

Figure 9-13 is a plot of true stress, true strain curves for the compression tests conducted in this paper. As the current density increased from 20 to 40 A/mm², there was not much of a change with respect to flow stress, as there was little flow stress reduction. When the current density approached 50 A/mm², the tungsten carbide became red hot as shown in Figure 9-14. The specimens did not turn red hot at lower current densities. The curve shown for the current density of 50 A/mm² was stopped when the dies began to melt. This is the threshold current density for this compression testing, at this current density; the tungsten carbide is hot enough to melt the steel dies. For this current density, the test was stopped once a stress drop was seen to prevent damage to the dies.

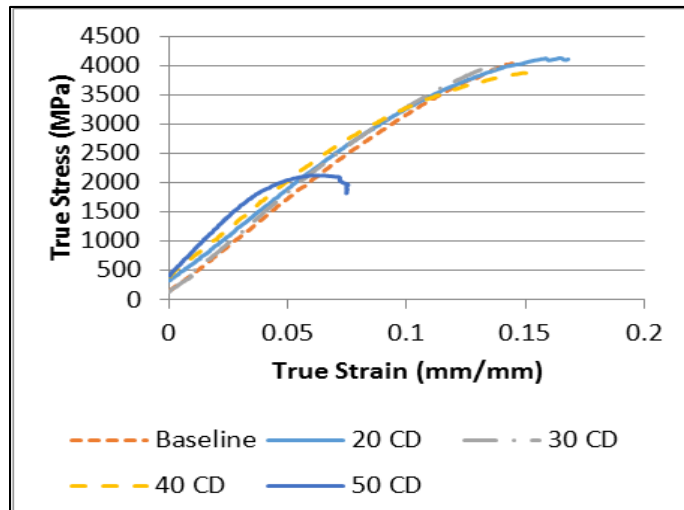


Figure 9-13: True stress/strain curves for EA compression of WC at various current densities



Figure 9-14: WC with a current density of 50A/mm², note the color change due to heat

The threshold current phenomenon has only been seen in compression to date and has been shown in various different metals ranging from aluminums to steels [25]. There is still not an understanding of why some metals exhibit threshold behavior while others do not. However, the threshold phenomenon is the same in most materials that exhibit it, there will be little effect of electrical current up until the threshold, past the threshold, maximum stress reductions can be seen, sometimes accompanied with large formability gains.

Since the specimen exhibited no stress drops at current densities less than 50 A/mm², and a clear temperature rise was seen at 50 A/mm², it can be assumed that a large

proportion of the effect of electricity on tungsten carbide is based on macro scale joule heating. Using the color shown in Figure 9-14, an approximate temperature can be assumed based on color emissions of metals at elevated temperature [119]. Using this approach, it would be assumed that the carbide was between 800-1000 °C. This temperature is hot enough to melt many commonly machined metals and may lead to reduced surface quality and part finish. However, while the WC softened due to the high current density, continuation of the test resulted in significant damage to the steel dies, showing that a tungsten carbide bit would outlast a steel bit in a drilling operation.

IMPLICATIONS ON ELECTRICALLY-ASSISTED MACHINING

When tungsten carbide is used for electrically-assisted milling and turning operations as replaceable tool inserts, problems could arise due to the data presented in this paper. Depending on the depth of cut and tool engagement, the current density running through the tool could be greater than the threshold value of 50 A/mm², shown in this paper. At this point the tool itself is softened (evident by less brittle fracture) which could lead to increased tool wear and decreased tool life. If the current density is large enough, it may lead to tool failure and fracture. Even if the tool is not damaged, the increased tool temperature when at the threshold value could cause altered material properties of the object being machined where the tool is making contact or could melt the material away rather than cutting it. This may result in a deteriorated surface finish.

The tools from Ulutan *et al.* [8] are shown in Figure 9-15. As is visible from the tools, the effect of electricity greatly accelerated tool wear but reduced cutting force. This damage may be a result of exceeding the threshold current density of WC for a prolonged period of time.

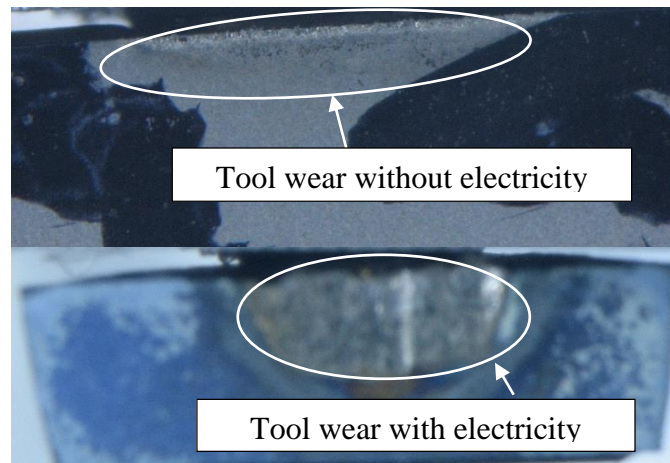


Figure 9-15: Tool wear from EA turning [8]

WC has a higher working temperature than steel, even when the current density in the carbide was 4x higher than the steel platen that was used to form it, the steel still failed. This shows that WC may have a better use in EA drilling than steel bits, though this comes with a cost penalty of about 7x. WC tools are examined for drilling high strength steel in the next section.

Elevated Feedrate Drilling of 1500MPa Steel

This section examines the feasibility of augmented drilling in aggressive cutting conditions to determine the effect of electricity on tool life and to evaluate the potential of electric augmentation to overcome limitations of traditional drilling, namely through a process time and feedrate study in drilling high strength steel. PHS1500 steel was used here and was prepared using the setup as explained in the experimental setup section.

A DoE study similar to what was used for 1008CR steel is conducted with input parameters shown in Table 9-7. Spindle speed is held constant at 560 RPM, current is varied between 0A and 600A. Feedrates of 50.8 and 101.6 mm/min are used, and 3 holes are made per bit with 2 replications per parameter set. Following the DoE, each parameter

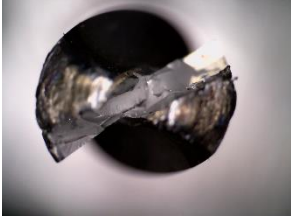

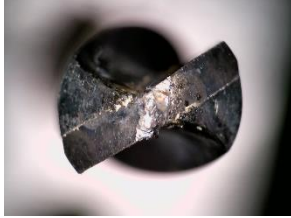
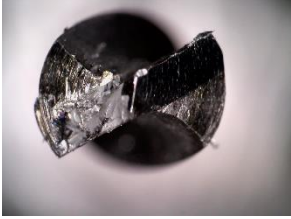
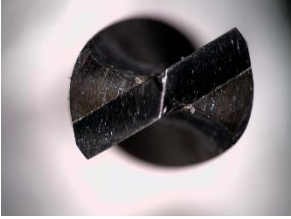

set was tested until bit failure to determine potential tool life increase in the presence of electric current.

Table 9-7: DoE for PHS1500 Steel

Factor	Level 1	Level 2	Level 3
Feedrate (mm/min)	50.8	101.6	-
Current (A)	0	300	600
Spindle (RPM)	560	-	-
Number of Holes	1	2	3
Experimental Outputs			
Maximum Temperature (°C)			
Maximum Axial Drilling Force (N)			
Average Flank Wear (mm)			

In the 0A test in both 50.8 and 101.6mm/min feedrate, catastrophic failure of the bit was observed within the 3 cuts, resulting in unreliable force data (following tool failure, the limit of the load cell was reached). As shown in tool flank face images in Table 9-8, the 0A case bits are broken. However, in the 300A test, drill bits showed near sharp condition after 3 cuts. In the 600A test drill bits experienced arcing and softening of the chisel edge, but it could retain sharp cutting edges. As such, the output of the DoE is set to 2 current values (300 and 600A) to allow for proper evaluation of the effect of electricity.

Table 9-8: Tooling images after 3 cuts in drilling PHS1500 steel for 2 different feedrates and 3 different currents

Feed (mm/min)	Electric Current (A)		
	0	300	600
50.8			
101.6			

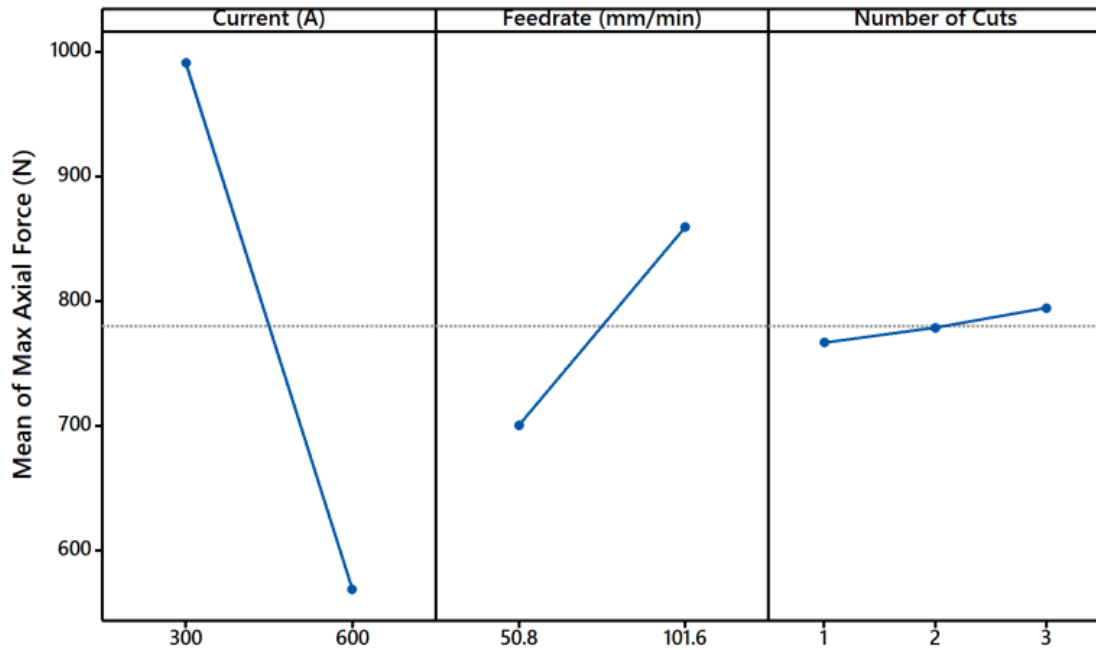


Figure 9-16: Main effects plot for maximum axial force during EA drilling of PHS1500 steel

The main effects plot for maximum axial force during electroplastic drilling of PHS1500 is shown in Figure 9-16. The feedrate and number of cuts show trends similar to the 1008CR steel. However, 1008CR steel had 150N difference between the mean results of all parameter sets, while PHS1500 has a 500N difference, showing that the effect of electric current is much greater on the PHS1500. The 1008CR steel had a force rise at 300A, while for both 300A and 600A tests the force decreases for PHS1500. This is due to the strength of the steels; PHS1500 is roughly 5 times stronger than 1008CR. Therefore, increasing the temperature through increased current will have a greater effect. In addition, the WC-tipped tool has a higher working temperature than the black oxide steel tool, allowing for greater temperatures without significant softening. However, too great of a temperature rise can lead to thermal expansion of the steel portion of the bit, allowing the

carbide tip to separate, resulting in tool failure. The experimental results at 50.8 and 101.6mm/min tests at various electric current inputs for the first and third cuts are shown

in

Figure 9-17 and given in

Table 9-9.

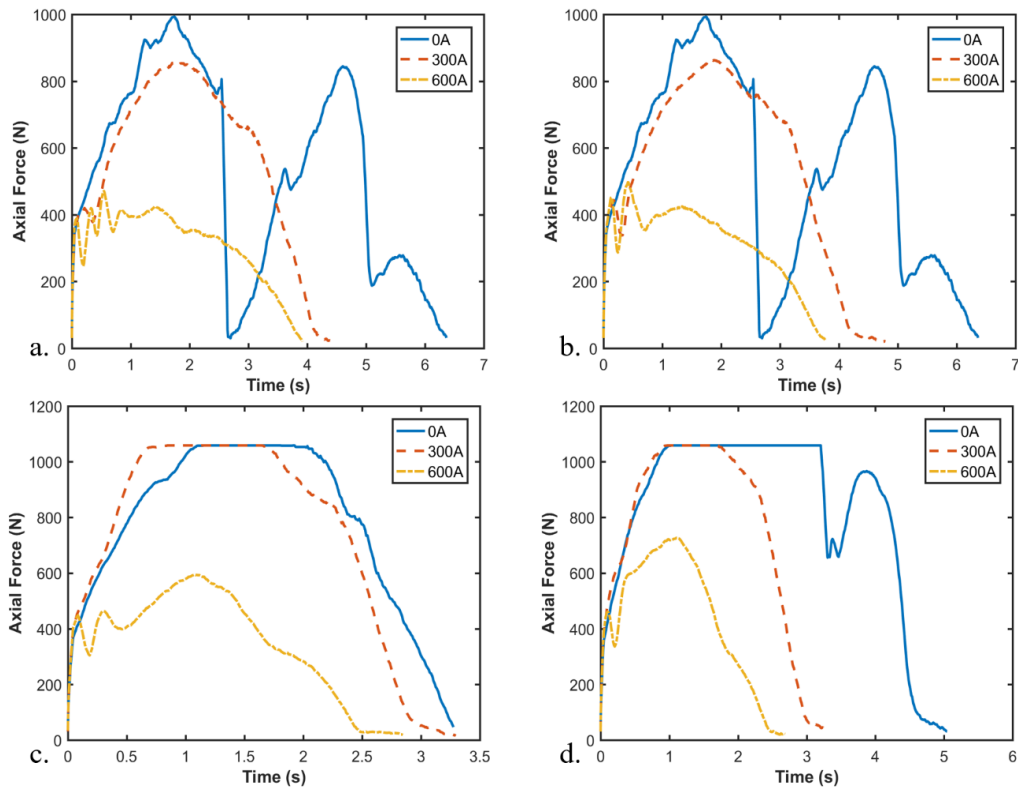


Figure 9-17: Axial force comparison for different current magnitudes (a) 50.8 mm/min 1st cut, (b) 50.8 mm/min 3rd cut, (c) 101.6 mm/min 1st cut, and (d) 101.6 mm/min 3rd cut. Cut 1 shown for the 1st and 3rd cuts for 50.8 mm/min due to failure. Cut 2 shown for 0A 3rd cut at 101.6mm/min due to bit failure on the 2nd cut.

Table 9-9: Maximum force and temperature results from high feedrate drilling of PHS1500 steel

Axial Force Results (N)						
Feedrate (mm/min)	Current (A)	Cut Number	Trial 1	Trial 2	Average	STD. Dev.
50.8	0	1	993	1059	1026	47
50.8	0	2				
50.8	0	3			Bit Failure	
101.6	0	1	1059	1043	1051	11
101.6	0	2	1059	1059	1059	0
101.6	0	3			Bit Failure	
50.8	300	1	855	1001	928	103
50.8	300	2	851	978	915	90
50.8	300	3	863	995	929	94
101.6	300	1	1059	1059	1059	0
101.6	300	2	1059	1059	1059	0
101.6	300	3	1059	1059	1059	0
50.8	600	1	471	456	463	11
50.8	600	2	459	486	472	19
50.8	600	3	497	494	496	2
101.6	600	1	594	641	618	33
101.6	600	2	644	694	669	35
101.6	600	3	727	663	695	45
Temperature Results (°C)						
Feedrate (mm/min)	Current (A)	Cut #	Trial 1	Trial 2	Average	STD. Dev.
50.8	0	1	137	158	148	15
50.8	0	2				
50.8	0	3			Bit Failure	
101.6	0	1	269	244	256	18
101.6	0	2	296	285	290	8
101.6	0	3			Bit Failure	
50.8	300	1	281	404	342	87

50.8	300	2	297	414	355	83
50.8	300	3	305	416	360	78
101.6	300	1	259	377	318	84
101.6	300	2	274	367	320	66
101.6	300	3	268	373	321	74
50.8	600	1	580	580	580	0
50.8	600	2	580	580	580	0
50.8	600	3	580	580	580	0
101.6	600	1	580	580	580	0
101.6	600	2	578	577	577	1
101.6	600	3	580	580	580	0

The large force drops for the 0A cases indicate where the tool failed. The 101.6 mm/min feedrate at 0A and 300A reached the maximum of the loadcell, resulting in the plateau. The oscillation in the beginning of the cutting process in the 600A test of

Figure 9-17 is caused by thermal softening and its resultant cutting force reduction. The load cell reaches 333N, triggering the electric current, which then causes the load to drop back below 333N, turning the current off until the load exceeds 333N again. The force reductions for the PHS1500 are much greater than 1008, at 600A tests, the resultant axial force reduction compared to the 0A case for 50.8mm/min is 54, 55, 51% for the 1st-3rd cut, respectively. The force reduction for 101.6mm/min is 47, 44, 51% for the 1st-3rd cut, respectively. While the 600A case had the lowest cutting force, it also suffered more wear than the 300A case due to arcing or excessive softening at the onset of electric current, which is shown in Table 9-8. The main effects plot for maximum temperature is shown in Figure 9-18, with the maximum temperature of each test in

Table 9-9.

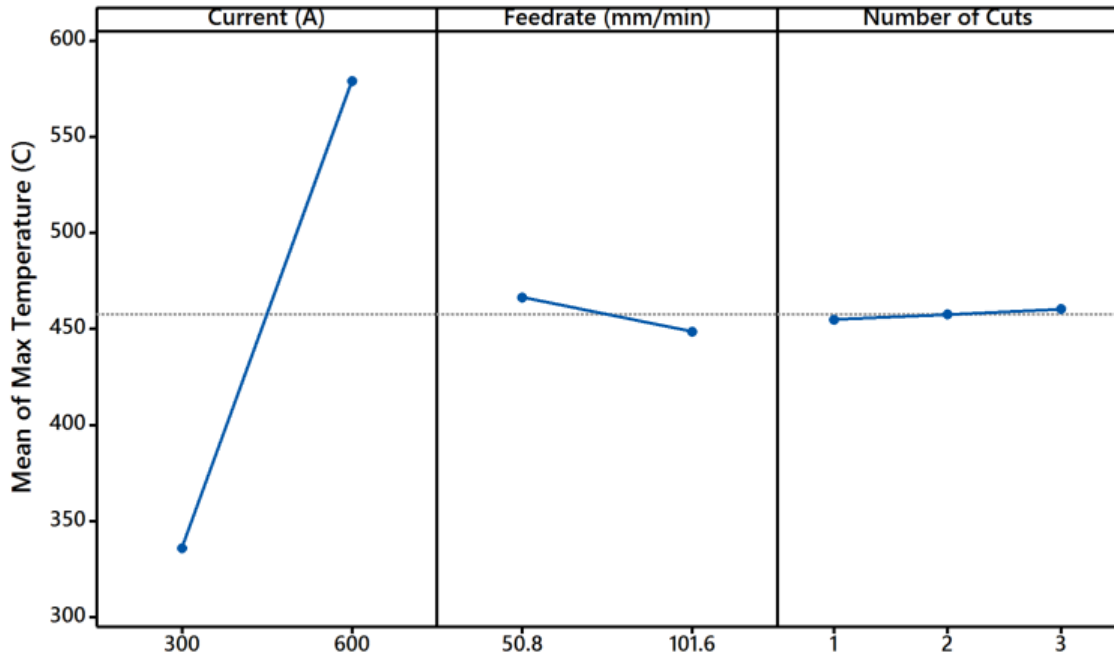


Figure 9-18: Main effects plot for maximum temperature during electroplastic drilling of PHS1500

The trends are similar to 1008CR steel, except that the difference between the means with respect to current is lower for PHS1500 with a spread of 250°C versus a difference of 400°C for 1008CR steel. This is caused by the differences in process time and lack of 0A tests in the DoE. Since the 1008CR steel was processed at 12.7 and 25.4 mm/min feedrates, it resulted in more time for Joule heating and a higher resultant temperature. In contrast, a higher feedrate used in drilling PHS1500 requires a higher electric current to achieve the same temperature. It may be possible to predict this if a current density could be calculated, though as shown in the modeling section, this presents some problems based on friction assumptions. The temperature results for both feedrates for the first and third cuts are shown in Figure 9-19. There is a temperature increase from

the first to the third cut for both feedrates. However, the difference is greater in the 50.8 mm/min test.

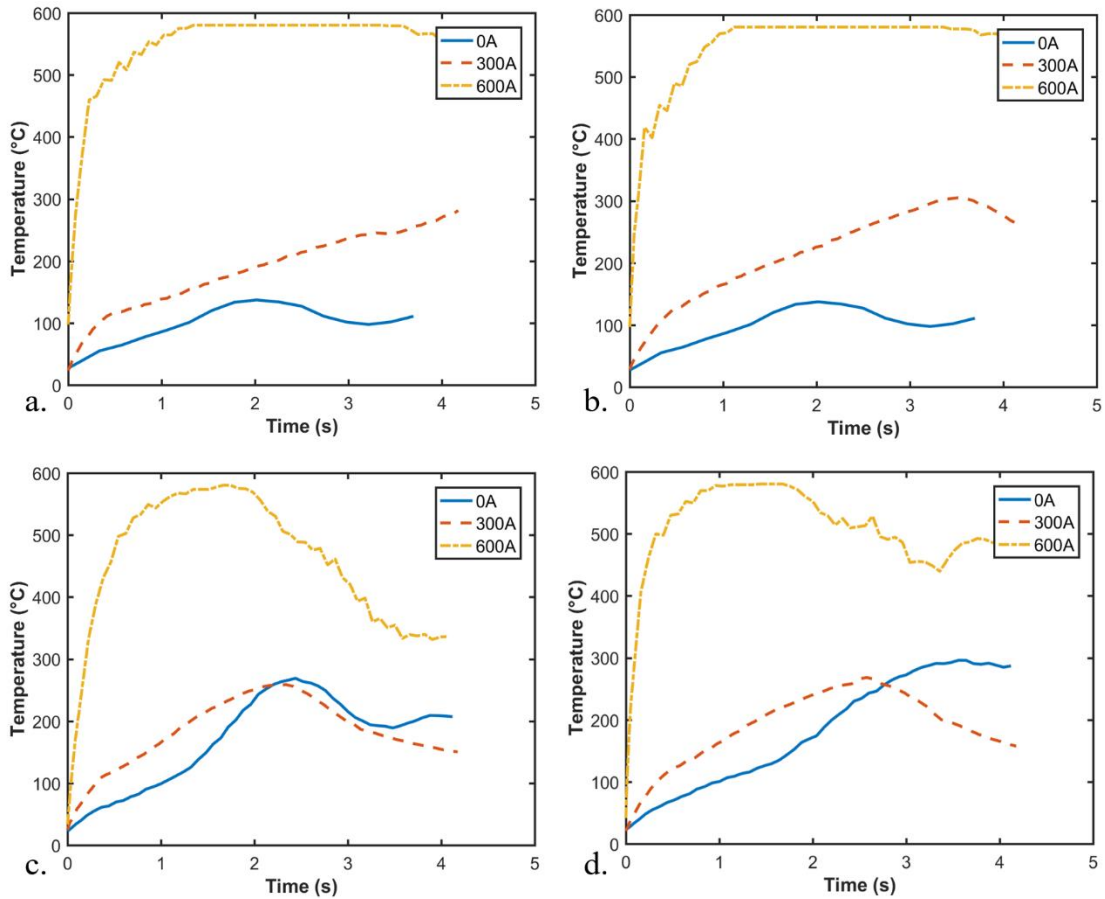


Figure 9-19: Temperature comparison for different current magnitudes (a) 50.8 mm/min 1st cut, (b) 50.8 mm/min 3rd cut, (c) 101.6 mm/min 1st cut, and (d) 101.6 mm/min 3rd cut. Cut 1 shown for the 1st and 3rd cuts for 50.8 mm/min due to failure. Cut 2 shown for 0A 3rd cut at 101.6mm/min due to bit failure on the 2nd cut.

To evaluate the potential for tool life savings, the first bit for each parameter set is tested until failure. In the 0A tests for both 50.8 and 101.6 mm/min, the drilling bit reached catastrophic failure mode after 3 initial cuts and therefore are not tested further. In the

101.6mm/min test, the drill bit fails after the second cut in both replications, while in the 50.8mm/min test, the drill bit fails after the first cut in both replications. This is likely due to the vibration of the fixture coupled with the slower penetration of the lower feedrate. The vibration of the spindle from the connected large electrical leads can cause the bit to grab the part more than it would without the excess vibration, therefore leading to high stresses on the bit and early failure. The results for 3 sequential cuts are shown in Figure 9-20. The force increases with each cut on the 0A and 600A cases. However, at the 300A test, no significant change observed in force between 3 sequential cuts. The force results from the run-until-failure testing are shown in Figure 9-21.

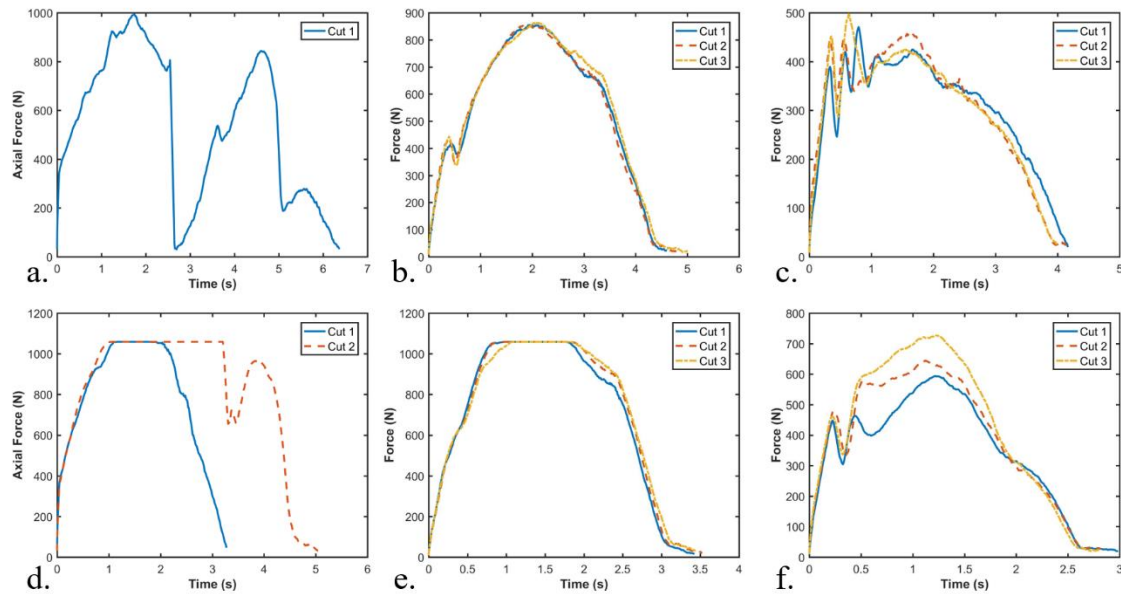


Figure 9-20: Axial force results for 3 sequential cuts for (a) 0A 50.8mm/min, (b) 300A 50.8mm/min, (c) 600A 50.8mm/min, (d) 0A 101.6mm/min, (e) 300A 101.6mm/min, (f) 600A 101.6mm/min

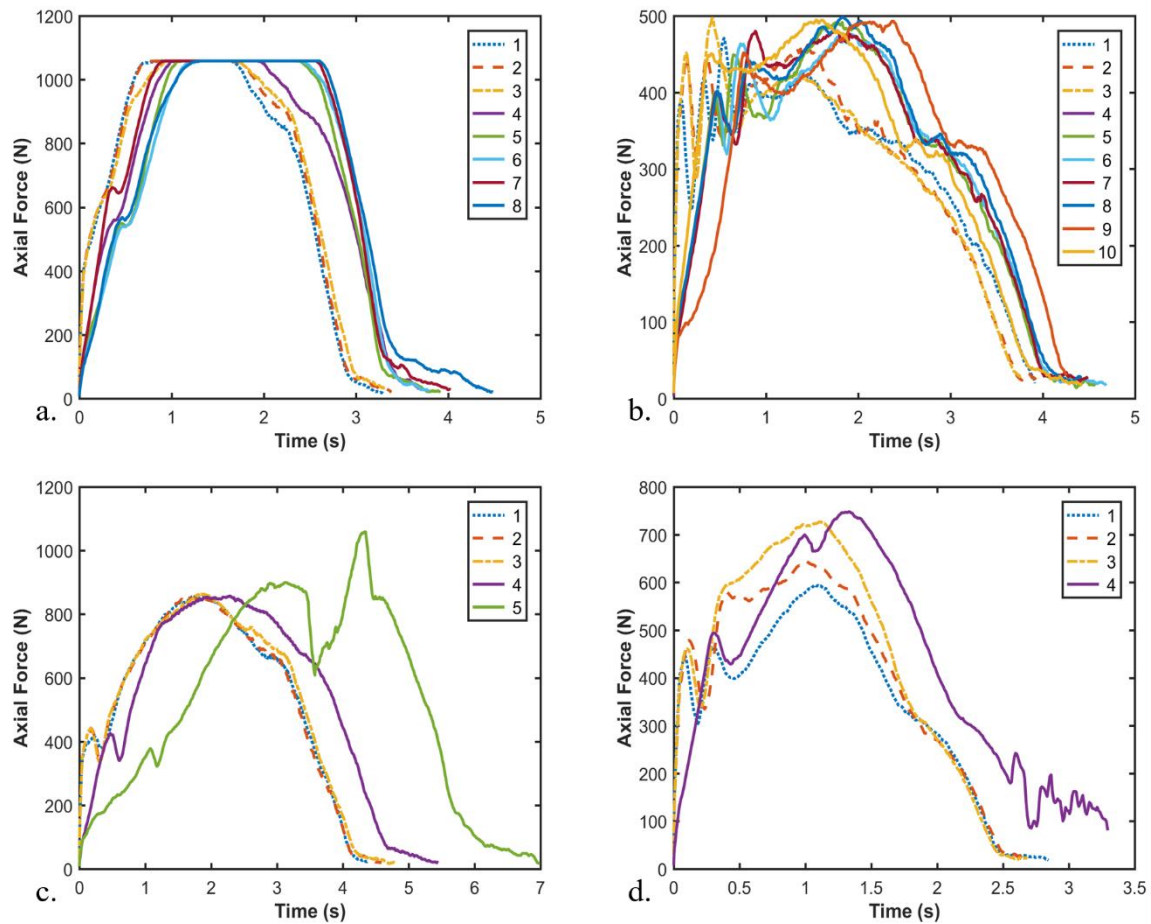
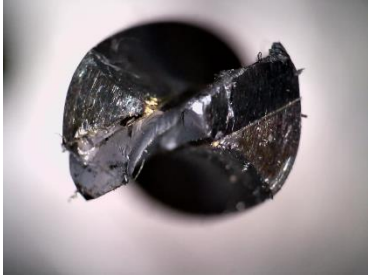





Figure 9-21: Axial force results for cutting to failure for (a) 300A 50.8mm/min, (b) 600A 50.8mm/min, (c) 300A 101.6mm/min, (d) 600A 101.6mm/min

For the 101.6mm/min tests, bits failed after 5 and 4 cuts in 300A and 600A respectively. Electric current was only able to extend the life of the tools for the 101.6mm/min case by 3 and 2 cuts for 300A and 600A, respectively. However, this does show that electricity has the potential to allow for higher feedrates in the presence of electric current as the electrically applied bits outlasted the 0A bits. A higher current magnitude and load trigger may lead to more desirable results. Tool images following the endurance testing are shown in Table 9-10.

Table 9-10: Tooling after failure testing, all bits are failed except for 600A at 50.8 mm/min. 300A at 101.6mm/min has chips and a large crack through the carbide portion of the bit.

Feedrate (mm/min)	Electric Current (A)	
	300	600
50.8		
101.6		

In the 50.8 mm/min tests a significant tool life improvement in the presence of electric current was observed. The drill bit in 0A tests failed during the first cut for both feedrates. However, in 300A, 8 cuts could be completed before tool failure. The drill bit in the 600A lasted for 10 cuts and did not fail. Due to material restrictions, the testing was stopped at 10 cuts. Comparing the tool wear image for this case at 10 cuts, in Table 9-10, to the wear images after 3 cut wear shown in Table 9-8, there appears to be insignificant difference with respect to the tool wear area. The chisel edge is more worn, which resulted in an extra 100N of force throughout the testing but failure was not observed. This shows

that electric current has the ability to drastically improve tool life and allows for drilling at a higher feedrate than what is possible without an electric current.

Hole Quality and Heat Affected Zone

This section examines the effect of electricity on the heat affected zone (HAZ) and hole quality during elevated feedrate drilling of PHS1500. This will help to evaluate if the pros of increased tool life are outweighed by hole quality or softening of the part.

The heat generated by the electricity, friction, and deformation energies led to softening of the base steel material. If the temperature approached the plasticity zone for the metal, the metal could flow like a fluid while remaining a solid. This technique is often used in solid state forming and joining operations such as flow drilling, flow drill screwing, and friction stir welding. However, in a drilling process, this creates an extrusion on the back of the part, if this extrusion is tall enough it may present problems if the sheet metal is to be mated to other components.

Figure 9-22 shows the extrusion height for the first 3 cuts from each of the parameter sets studied. As the 0A case at 50.8mm/min bit failed on the 1st cut, the 2nd and 3rd cuts both show 0 for extrusion height, as a hole was not created. The same is true for cut 3 at 101.6mm/min. At 50.8mm/min, both applied current caused an extrusion height increase of 0.13mm on the first cut. The extrusion height continued to increase for the subsequent cuts. The 300A case resulted in taller extrusions even though it produced a lower temperature (280°C vs >580°C). This was caused by the resultant softening that accompanied the higher temperature of the 600A case. At 600A the steel softened and was easier to shear, resulting in lower axial force values. The lower axial force values reduced

the extrusion forming force, resulting in smaller extrusions than the 300A case. The 3rd cut caused an extrusion height of 0.62mm at 300A, 41% of the sheet thickness. The 600A case resulted in an extrusion height of 0.45mm after the third cut, 30% of the sheet thickness. If either of these parts need to mate to another part with direct contact, then post process machining would be required. However, if there is clearance or a gap then the extrusion would not be a problem.

At 101.6mm/min, a similar trend is observed. The 300A case produced taller extrusions than the 600A case, but overall, the extrusion heights are lower on the second and third cut but higher on the first. Both of the current cases show a decrease in extrusion height from the first to second cut followed by an increase between the second and third cut. This could be caused by initial dulling of the chisel edge of the drill bit. When the current is initially applied, arcing may occur which will result in a rapid localized increase in temperature resulting in taller extrusions.

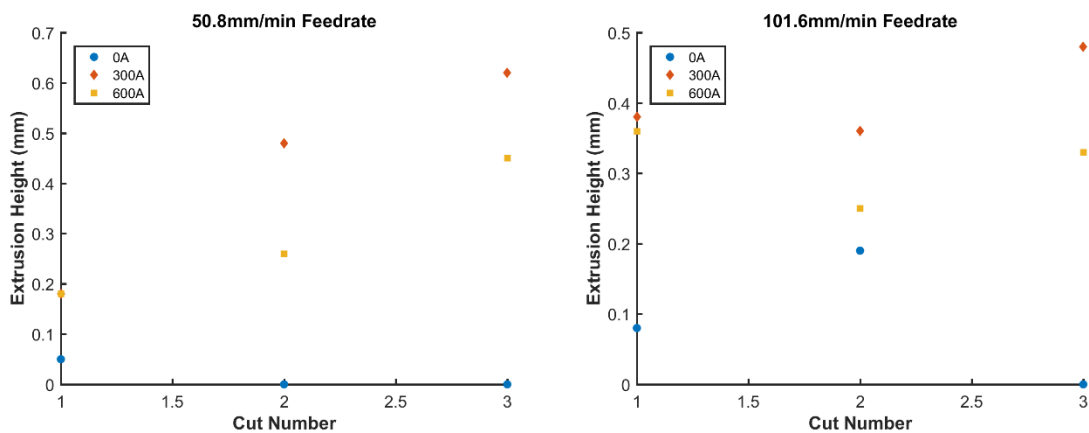


Figure 9-22: Extrusion height for first 3 cuts over all parameter sets tested. At 50.8mm/min the 300A and 600A cases produced the same result on the first cut.

It has been shown that the extrusion height from electroplastic drilling could be a problem if direct mating of surfaces is required. Next the HAZ of the parts was examined using Vickers hardness measurements. The idea behind electroplastic drilling is that it could cause localized softening near the drill but such that the bulk sheet properties are mostly unaltered. Figure 9-23 shows Vickers hardness comparison after the first cut between the base material and electroplastic drilling operations at each of the parameters tested. In the 0A case, the spot closest to the hole shows a lower hardness than the remaining points. This is where most of the heat is concentrated, it is expected that this region would be softened more than the other spots which are further from the heat source (drill bit). For the 101.6mm/min case, the first hole is 2% lower hardness than the base material. For the 50.8mm/min case, the first hole is 6% lower hardness than the base material, the remainder of the metal is 4% lower hardness. In the 0A case, the hardness is only slightly decreased for both parameter sets, this is not a concern for drastically changing the properties of the sheet. However, the softening is not localized near the hole and extends more than 10.5mm from the edge of the hole.

In the 300A case at 101.6mm/min, each of the points has the same hardness. The part's hardness has been decreased by 3%, an increase in softening over the 0A case but not significant. In the 600A case at 50.8mm/min the entire part had a uniform decrease in hardness of 4% compared to the base metal, once again not a significant decrease.

In the 600A case at 101.6mm/min the entire part has a uniform hardness decrease of 8% compared to the base metal, the greatest softening observed in the tests conducted. The 600A case at 50.8mm/min had a softer first point near the edge of the drilled hole,

similar to the 0A case. The remainder of the part had a near uniform hardness with a decrease of 4%.

For the 0A and 300A cases, the 101.6mm/min case is harder than the 50.8mm/min case. This reverses at 600A, the 101.6mm/min is softer than the 50.8mm/min case. Both of these tests maxed out the thermal camera. It is possible that they both reached a phase transformation temperature which could influence the resultant hardness but a clear conclusion cannot be drawn. However, overall, with a maximum decrease in hardness of only 8%, the drilling process does not have a large influence on the resultant part strength. Hardness is correlated with strength, as such, if it is assumed that an 8% decrease in hardness matches an 8% decrease in strength. The softened steel would still have tensile strength near 1380MPa.

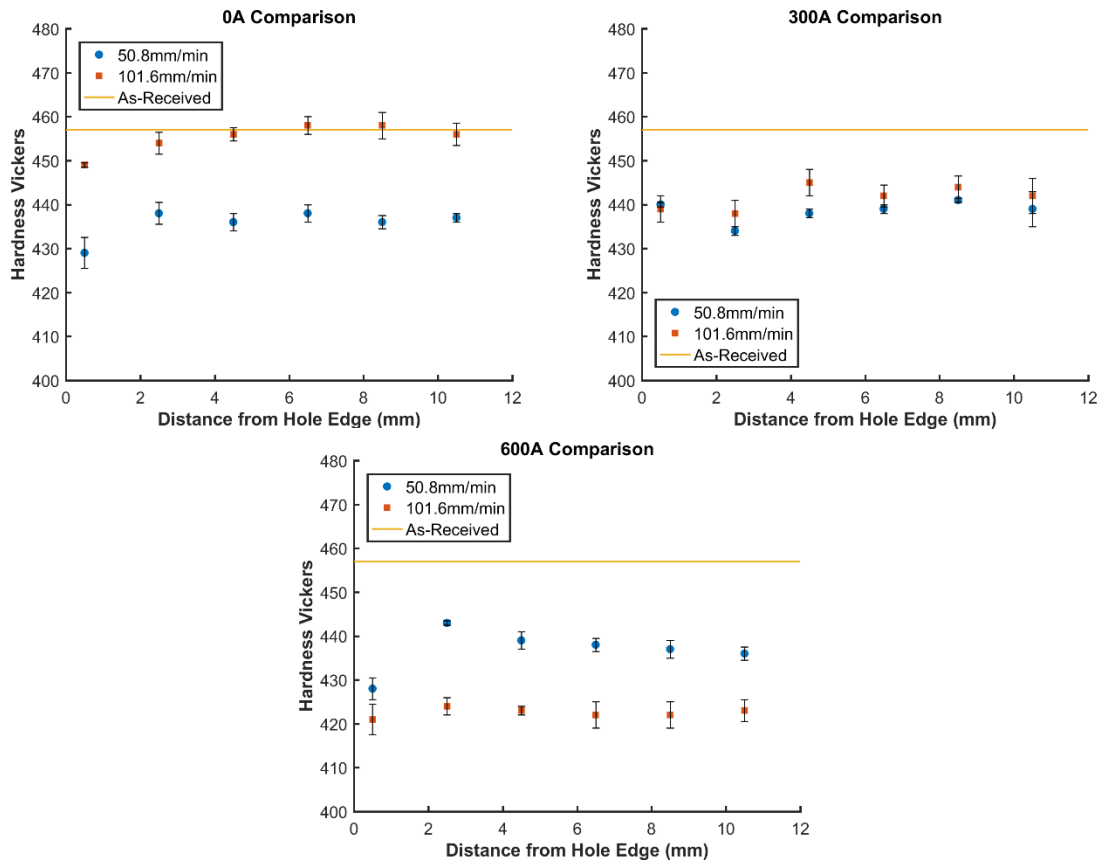


Figure 9-23: Vickers hardness measurements taken radially from the drilled hole for each parameter set after the 1st cut

Conclusions

This objective of the paper was to examine the electroplastic drilling of mild 1008CR steel and high strength PHS1500 steel through experimentation and modeling. The following conclusions were found:

- Electric current has a larger effect on axial force and temperature than feedrate or spindle RPM on drilling.

- Electric current can result in a reduction of cutting forces and tool wear. The higher the strength of the base material, the higher the force reduction (up to 50% for PHS1500).
- Electric current allows for improved tool life and the ability to cut at higher feedrates. At 600A, the bit lasted 10 cuts in comparison with the 0A tests where the tool failed at the 1st cut.
- In the presence of electricity, the part softens uniformly with a maximum hardness decrease of 8%. Assuming strength is also reduced by only 8% the tensile strength would remain near 1380MPa.
- Due to elevated temperature, the drilling operation may act as a flow drilling or flow forming operation, resulting in extrusion formation on the back side of the part. This can range up to 60% of the sheet thickness and could present problems for part mating.
- Tungsten carbide (WC) bits can handle electric current better than traditional black oxide steel bits and allow for higher current magnitudes with less damage.
- An electroplastic drilling model, the first of its kind to predict cutting forces and temperatures in the presence of electricity was formulated and evaluated. The model formulation itself is sound but it requires advancement in the fields of friction modeling, electrical conduction length modeling, and temperature acquisition in machining to reach its predictive potential. For these reasons and the lack of a published material model for PHS1500 steel.

CHAPTER TEN

10. SUMMARY AND CONCLUSIONS

Intellectual Merit

This research evaluated the leading theory to predict the transient electroplastic effect stress drop, the microscale Joule heating theory. This theory suggested that localized hot spots exist in a metal near areas with high electrical resistivity such as grain boundaries, precipitates, and dislocation chains. This research created the first thermal-electrical-structural model with grains, grain boundaries, and precipitates to create a heterogeneous electrical resistivity field. It was determined that in order for the microscale Joule heating theory to represent the electroplastic effect the grain boundary to grain resistivity ratio was much higher than experimental values in the literature. As such it was concluded that the electroplastic effect is not governed by microscale Joule heating. As most of the leading theories were dismissed based on research conducted in this paper as well as in the literature a new theory based on electron stagnation was created to further explain the dissolution of bonds theory and address differences between electrical and thermally equivalent testing.

It was shown that electricity has effects beyond thermal mechanisms on precipitation in aluminum alloys through furnace and electrically treated specimen comparison. The literature stated that there was an absence of the electroplastic effect at high strain rate. This research showed that this conclusion was likely caused by the use of too low a current density to notice an effect at the literature reported strain rate of 1000/s. Elevated strain rate testing was conducted up to 1/s and there was found to be an

electroplastic effect, though the applied current density applied had to increase with increasing strain rate.

The first electrically-assisted machining model was created to predict process temperature and axial force. While the creation and formulation of the model is valid, the current limits on technology and knowledge prevent the drilling model from being used in a predictive capacitance. Further knowledge is required on the electrical path and friction modeling. The electrical path could be modeled using an FEA software if dynamic explicit solvers were available for thermal-structural-electrical models. Friction is typically a curve fit variable in manufacturing and the effect of electricity on friction remains unknown.

Broader Impacts

This research showed that electricity can be used to accelerate solutionization in aluminum alloys. This can be commercialized to drastically reduce process time for solutionization from the conventional 30 minutes to closer to 5 minutes or less. Near-full solutionization was achieved from a T6 temper with $225\text{A}/\text{mm}^2$ applied for 0.3 seconds. An industrial application would apply a higher current density to maximize electrical precipitate interactions following by a reduced current density to act as a “hold/soak” and maintain the elevated temperature from the high current density pulse.

The first large scale study of electrically-assisted machining was conducted. It was determined that electricity could improve tool life by 1000% in electroplastic drilling of high strength steel parts, while allowing for increase in feedrate and decrease in process time beyond what was obtainable without electrical augmentation. This opens the door for electrically-assisted machining to reduce cutting forces and process time while improving

tool life in hard to machine materials, allowing for cost savings both on the process time front as well as the tooling cost front.

Future Work and Recommendations

The electron stagnation theory should be evaluated using Atomic Force Tunneling microscopy, which is capable of tracking the movement of ion cores. Electricity should be applied in an isothermal manner (use large heat sinks or forced cooling) to track the motion of ion cores or dislocation chains to determine if the electron stagnation theory is valid. From the modeling side, the effect of current density on bond strength should be evaluated.

The effect of electricity on precipitation in aluminum alloys should be further explored with an end goal of industrial application. Electrical application methodologies should be created to regress an aged aluminum back to an annealed aluminum or back to a solutionized state. As mentioned, a high current density pulse to quickly remove precipitates while rapidly increasing temperature should be followed by a lower electrical pulse to maintain high temperature without melting the part. The current densities and times required to minimize process time should be determined. In addition, the effect of electricity on an annealed aluminum alloy should be explored to see if artificial aging times can be reduced in the presence of electricity.

Electrically-assisted machining should be extended to other operations beyond drilling. Milling will present challenges as the tool is not always engaged during the cut and may result in arcing, but also presents the greatest usefulness to industry for milling hard to machine materials. Other tool materials should be studied to determine if a low electrical resistance high strength material can further improve electroplastic machining. Tool coatings and their interactions with the electroplastic effect requires further research.

CHAPTER ELEVEN

11. APPENDICES

ABAQUS Subroutine

```
SUBROUTINE USDFLD(FIELD,STATEV,PNEWDT,DIRECT,T,CELENT,  
1 TIME,DTIME,CMNAME,ORNAME,NFIELD,NSTATV,NOEL,NPT,LAYER,  
2 KSPT,KSTEP,KINC,NDI,NSHR,COORD,JMAC,JMATYP,MATLAYO,  
3 LACCFLA)
```

```
INCLUDE 'ABA_PARAM.INC'
```

```
INTEGER, PARAMETER :: gbfact=17000  
INTEGER, PARAMETER :: dislocres=3.3D-25
```

```
CHARACTER*80 CMNAME,ORNAME  
CHARACTER*3 FLGRAY(15)  
DIMENSION FIELD(NFIELD),STATEV(NSTATV),DIRECT(3,3),  
1 T(3,3),TIME(2)  
DIMENSION ARRAY(15),JARRAY(15),JMAC(*),JMATYP(*),COORD(*)
```

```
C Get Z direction stress
```

```
CALL
```

```
GETVRM('S',ARRAY,JARRAY,FLGRAY,JRCD,JMAC,JMATYP,MATLAYO,LACC  
FLA)
```

```
S11 =ARRAY(1)
```

```
C Get Nodal Temp
```

```
CALL
```

```
GETVRM('TEMP',ARRAY,JARRAY,FLGRAY,JRCD,JMAC,JMATYP,MATLAYO,L  
ACCFLA)
```

```
nodeT =ARRAY(1)
```

```
C Field1=axial stress, field2=nodal temp, field3=elastic mod, field4=dislocdens,  
field5=econd-broken due to rounding
```

```
FIELD(1)=S11
```

```
FIELD(2)=nodeT
```

```
FIELD(3)=(-3.596389D-10*nodeT**4+4.313687D-7*nodeT**3-1.918630D-  
4*nodeT**2+2.065581D-3*nodeT+78.81334)*10**9
```

```
FIELD(4)=gbfact*((2.65*S11*1D6)/(FIELD(3)*5.7D-10))**2
```

```
FIELD(5)=1/(dislocres*FIELD(4)+4.1D-8*(1+.0039*(nodeT-293)))
```

```
C Temp dependent elastic modulus
```

```
C ((-3.596389D-10*nodeT**4+4.313687D-7*nodeT**3-1.918630D-  
4*nodeT**2+2.065581D-3*nodeT+78.81334)*10**9)
```

```
C If error, write comment to .DAT file:
```



```

IF(JRCD.NE.0)THEN
  WRITE(6,*) 'REQUEST ERROR IN USDFLD FOR ELEMENT NUMBER ',
1  NOEL,'INTEGRATION POINT NUMBER ',NPT
ENDIF
RETURN
END

```

Matlab Code for Creating Subroutine Data

```

clear

clc

clf

%this is set for 7075-t6

%Define grain boundary dislocation density factor
GBfactor=17500;
maxstress=700; %max stress in MPa for alloy
Tinc=100; %increment of temperature for interpolation
stressinc=50; %increment on stress for interpolation
%elec resistivity of aluminum at room temp and 0 stress
resist0=4.1*10^-8;
%ambient temperature (K)
Tamb=300;
%Resistivity change factor for aluminum
alpha=.0039;
%Specific resistivity of a dislocation ohm-m3
specresist=3.3*10^-25;% 1.2-3.3
%Burger vector for aluminum
bergeral=5.73*10^-10; %m
mmprops=1; %if 1 then result divided by 10^6, 0 then normal

c=0;%matrix location variable
c2=0; %counting var
for T=Tamb:Tinc:893 %Kelvin
  if T<=773
    Emod=-3.596389*10^-10*T^4+4.313687*10^-7*T^3-1.918630*10^-
4*T^2+2.065581*10^-3*T+78.81334;
  else
    Emod=36.98;
  end
  c2=c2+1;
  c3=0;
  Tsave(c2)=T;
  Emodsave(c2)=Emod;
  for stress=0:stressinc:maxstress %MPa, cycle through 0-max stress of metal

```

```

stress2=stress*10^6; %Pa
c=c+1;
c3=c3+1;
shearmod=Emod*10^9/2.65;
%calculate dislocation density
dislocdens=((stress2/(shearmod*bergeral))^2)*GBfactor;
%calculate dislocation density based resistivity
dislocresist=specresist*dislocdens;
%calculate thermal based resistivity
thermalresist=resist0*(1+alpha*(T-Tamb));
%sum thermal and disloc resistivity to get total elec resistivity
totalresist=dislocresist+thermalresist;
%take reciprocal of elec resistivity to get elec conductivity
econd=1/totalresist;
%Output to ABAQUS format (Econd, T, field var 1 (stress))
results(c,2)=T;
if mmprops==1
    results(c,1)=econd/10^6;
    results(c,3)=stress2/10^6;
    plotsave(c2,c3)=econd/10^6;
else
    results(c,1)=econd;
    results(c,3)=stress2;
    plotsave(c2,c3)=econd;
end

end

end
% Stress=0:stressinc:700;
% Tplot=0:Tinc:893;
%
% figure(1)
% plot(Tsave,Emodsave)

% figure(2)
% [r,c]=size(plotsave);
% hold on
% for i=1:r
%     plot(Stress,plotsave(i,:))
%     legend(num2str(Tplot(i)))
% end
% hold off

```

Matlab Code for Drilling Model

```
%This function conducts a 2D heat transfer on an EA drilling test
%Heat is generated using Joule heating and energy input from metal shearing
clear
clc
RPM=350;
feedrate=0.5; %in/min
Current=150; %applied current in amps
Farbodfactor=.5;
mew=0.7;
fracstrain=9;
parheatfraction=0.5; %heat split between chip and part
timedelay=2.7; %2.7 for 0.5in/min
openname=[num2str(Current) 'A' num2str(RPM) 'RPM' num2str(feedrate)
'inmincut1.txt'];
al=fopen(openname);
%Process Parameters
thick=1.5; %mm
feedratem=feedrate*.0254/60; %feedrate in m/s
angveloc=RPM*2*pi/60; %angular velocity of spindle
distperrev=feedratem*60/RPM; %feed or distance per revolution in Z direction

C=6;%hyperbola shape factor

%Johnson-Cook Model Parameters
AJC=217*10^6; %Pa
BJC=234*10^6; %Pa
nJC=0.643;% strain hardening coef for JC
CJC=0.076;% curve fit factor for JC
m=1; %strain rate sensitivity for JC
strainrateref=0.001;% reference strain for JC model
Tmelt=1370+273.15; %melting temp of steel in Kelvin

%%%%%%%%%%%%%%%%%%%%%%%%%%%%%%%%%%%%%%%%%%%%%%%%%%%%%%%%%%%%%%%%%%%%%%%%
%Define specimen size, time step, ambient temperature, and nodal setup
%%%%%%%%%%%%%%%%%%%%%%%%%%%%%%%%%%%%%%%%%%%%%%%%%%%%%%%%%%%%%%%%%%%%%%%%
specwidth=25.4*1.25; %specimen width mm (1.25 inch)
speclength=25.4*2.5; %specimen length mm (2.5 inch)
timestep=0.01; %seconds
Tambient=298; %room temperature in Kelvin
hcomb=25; %combined convection radiation coeff
nlength=41; %number of elements along length of specimen
nwidth=21; %number of elements along width of specimen

%%%%%%%%%%%%%%%%%%%%%%%%%%%%%%%%%%%%%%%%%%%%%%%%%%%%%%%%%%%%%%%%%%%%%%%%
%Define drill bit parameters
```

```

%%%%%%%%%%%%%%%%%%%%%%%%%%%%%%%%%%%%%%%%%%%%%%%%%%%%%%%%%%%%%%%%%%%%%%%%
bitdiameter=.25; %bit diameter in inches
frictionanglerad=atan(mew);
frictionangle=atand(mew);
rakeangle=30; %degrees can range from 24-32 for 1/4 inch bit
rakeanglerad=rakeangle*(pi/180);
pointangle=67.5;%degrees center line of shaft to cutting edge 67.5
pointanglerad=pointangle*(pi/180);
shearplanerad=((pi/2)+rakeanglerad-frictionanglerad)/2;
shearplaneangle=shearplanerad*(180/pi);
chipthick=distperrev*sin(pointanglerad)/2;

%%%%%%%%%%%%%%%%%%%%%%%%%%%%%%%%%%%%%%%%%%%%%%%%%%%%%%%%%%%%%%%%%%%%%%%%
%unit conversions
%%%%%%%%%%%%%%%%%%%%%%%%%%%%%%%%%%%%%%%%%%%%%%%%%%%%%%%%%%%%%%%%%%%%%%%%
bitdiam=bitdiameter*.0254; %bit diameter in meters
taperedlength=bitdiam/(2*tan(pointanglerad));
specwidthm=specwidth/1000; %specimen width in meters
speclengthm=speclength/1000; %specimen length in meters
thickness=thick/1000;% specimen thickness in meters
endtime=(thickness+taperedlength)/feedratem; %process time in seconds
iterations=round(endtime/timestep); %number of iterations to complete solution
chiseledglength=0.2*bitdiam;
Achisel=distperrev*chiseledglength;
%%%%%%%%%%%%%%%%%%%%%%%%%%%%%%%%%%%%%%%%%%%%%%%%%%%%%%%%%%%%%%%%%%%%%%%%
%intialize temperature and properties
%%%%%%%%%%%%%%%%%%%%%%%%%%%%%%%%%%%%%%%%%%%%%%%%%%%%%%%%%%%%%%%%%%%%%%%%
T=ones(nwidth,nlength,iterations)*Tambient;
Ttool=ones(iterations,1)*Tambient;
count1=0; %arbitrary time step variable for assigning temperatures
[K,Density,Cp,Resistivity,CTE,UTS,Yield]=steell1008propsv2(T(:,:,1)); %intialize
matl props
elementlength=speclengthm/nlength; %determine length of elements
elementwidth=specwidthm/nwidth; %determine width of elements
elementthickness=thickness;% element thickness is equal to specimen thickness
for 2D
Acx=elementwidth*elementthickness;%calculate cross sectional area in x
direction
Acy=elementlength*elementthickness; %cross sectional area in y direction
dx=elementlength; %define nodal space in x
dy=elementwidth; %define nodal space in y
count2=1; %counting variable for new time step
count3=0; % counting variable for current time step
time=0;%initialize time to 0
thermaldiffusivity=5.2*10^-5;
distance=0; %initalize screw travel distance
rt=.25; %convergence criteria for 2D conduciton used in dts
dts=rt*dy^2/thermaldiffusivity; %suggested time step

```

```

if timestep> dts %check to see if timestep is acceptable
    disp('Error, time step too large, solution may diverge');
end

%Initialize large matrices
Qcond=zeros(nwidth,nlength,iterations);
Qcond1=zeros(nwidth,nlength,iterations);
Qcond2=zeros(nwidth,nlength,iterations);
Qconv=zeros(nwidth,nlength,iterations);
Qin=zeros(iterations,1);
dT=zeros(nwidth,nlength,iterations);
Tnew=zeros(nwidth,nlength,iterations);
A=zeros(iterations-1,1);
CD=zeros(iterations,1);
distance=ones(iterations,1)*distance;
drillrad=zeros(iterations,1);
drilldiam=zeros(iterations,1);
timesave=zeros(iterations,1);
Resistance=zeros(iterations,1);
Tstar=zeros(iterations,1);
Teststress=zeros(iterations,1);
shearstress=zeros(iterations,1);
Qdeform=zeros(iterations,1);
Fshear=zeros(iterations,1);
shearstrainrate=zeros(iterations,1);
velocity=zeros(iterations,1);
Vshear=zeros(iterations,1);
Qelec=zeros(iterations,1);
shearrate=zeros(iterations,1);
hyperbolacurv=zeros(iterations,1);

%%%%%%%%%%%%%%%%%%%%%%%%%%%%%%%%%%%%%%%%%%%%%%%%%%%%%%%%%%%%%%%%%%%%%%%%
%Main Loop
%%%%%%%%%%%%%%%%%%%%%%%%%%%%%%%%%%%%%%%%%%%%%%%%%%%%%%%%%%%%%%%%%%%%%%%%
while time<=(endtime-timestep) %main loop solution loop stepped by timestep
time
    %step count values and increase time
    count2=count2+1;
    count3=count3+1;
    time=time+timestep;
    %plottable time variables
    timesave(count3)=time;

    %Update Material Properties
    [K,Density,Cp,Resistivity,CTE,UTS,Yield]=steel1008prosv2(T(:, :, count3));
%intialize matl props
%%%%%%%%%%%%%%%%%%%%%%%%%%%%%%%%%%%%%%%%%%%%%%%%%%%%%%%%%%%%%%%%%%%%%%%%
    %Heat Transfer calculation

```

```

%%%%%%%%%%%%%%%%%%%%%%%%%%%%%%%%%%%%%%%%%%%%%%%%%%%%%%%%%%%%%%%%%%%%%%%%
%loop through elements to solve for new temperatures
for x=1:nwidth %loop through rows of temperature matrix
    for xx=1:nlength%loop through columns of active row of temperature
matrix
        if x==1 %determines if element is an upper horizontal edge element,
these have extra convection terms and 1 less conduction term
            if xx==1% top left corner node, these have 2 extra convection
and 2 less conduction terms

Qconv(x,xx,count3)=2*hcomb*elementwidth*elementlength*(T(x,xx,count3)-
Tambient)+hcomb*Acy*(T(x,xx,count3)-Tambient)+hcomb*Acx*(T(x,xx,count3)-
Tambient);

            %grain center x conduction
            Qcond1(x,xx,count3)=K(x,xx)*Acx*(T(x,xx+1,count3)-
T(x,xx,count3))/dx;
            %grain center y conduction
            Qcond2(x,xx,count3)=K(x,xx)*Acy*(T(x+1,xx,count3)-
T(x,xx,count3))/dy;
            %total conduction
            Qcond(x,xx,count3)=Qcond1(x,xx,count3)+Qcond2(x,xx,count3);
            %temperature change

dT(x,xx,count3)=timestep/(Density(x,xx)*Cp(x,xx)*elementlength*elementwidth*ele
mentthickness)*(Qcond(x,xx,count3)-Qconv(x,xx,count3));
            %determine new temperature and save to matrix
            Tnew(x,xx,count2)=T(x,xx,count3)+dT(x,xx,count3);

            elseif xx==nlength %top right corner node

Qconv(x,xx,count3)=2*hcomb*elementwidth*elementlength*(T(x,xx,count3)-
Tambient)+hcomb*Acy*(T(x,xx,count3)-Tambient)+hcomb*Acx*(T(x,xx,count3)-
Tambient);

            %grain center x conduction
            Qcond1(x,xx,count3)=K(x,xx)*Acx*(T(x,xx-1,count3)-
T(x,xx,count3))/dx;
            %grain center y conduction
            Qcond2(x,xx,count3)=K(x,xx)*Acy*(T(x+1,xx,count3)-
T(x,xx,count3))/dy;
            %total conduction
            Qcond(x,xx,count3)=Qcond1(x,xx,count3)+Qcond2(x,xx,count3);

dT(x,xx,count3)=timestep/(Density(x,xx)*Cp(x,xx)*elementlength*elementwidth*ele
mentthickness)*(Qcond(x,xx,count3)-Qconv(x,xx,count3));
            Tnew(x,xx,count2)=T(x,xx,count3)+dT(x,xx,count3);

            else %upper horizontal edge

```

```

Qconv(x,xx,count3)=2*hcomb*elementwidth*elementlength*(T(x,xx,count3)-
Tambient)+hcomb*Acy*(T(x,xx,count3)-Tambient);
    %grain center x conduction
    Qcond1(x,xx,count3)=K(x,xx)*Acx*(T(x,xx+1,count3)+T(x,xx-
1,count3)-2*T(x,xx,count3))/dx;
    %grain center y conduction
    Qcond2(x,xx,count3)=K(x,xx)*Acy*(T(x+1,xx,count3)-
T(x,xx,count3))/dy;
    %total conduction
    Qcond(x,xx,count3)=Qcond1(x,xx,count3)+Qcond2(x,xx,count3);

dT(x,xx,count3)=timestep/(Density(x,xx)*Cp(x,xx)*elementlength*elementwidth*ele
mentthickness)*(Qcond(x,xx,count3)-Qconv(x,xx,count3));
    Tnew(x,xx,count2)=T(x,xx,count3)+dT(x,xx,count3);
end

elseif x==nwidth %determines if element is on lower horizontal edge
    if xx==1 %bottom left corner node

Qconv(x,xx,count3)=2*hcomb*elementwidth*elementlength*(T(x,xx,count3)-
Tambient)+hcomb*Acy*(T(x,xx,count3)-Tambient)+hcomb*Acx*(T(x,xx,count3)-
Tambient);
    %grain center x conduction
    Qcond1(x,xx,count3)=K(x,xx)*Acx*(T(x,xx+1,count3)-
T(x,xx,count3))/dx;
    %grain center y conduction
    Qcond2(x,xx,count3)=K(x,xx)*Acy*(T(x-1,xx,count3)-
T(x,xx,count3))/dy;
    %total conduction
    Qcond(x,xx,count3)=Qcond1(x,xx,count3)+Qcond2(x,xx,count3);

dT(x,xx,count3)=timestep/(Density(x,xx)*Cp(x,xx)*elementlength*elementwidth*ele
mentthickness)*(Qcond(x,xx,count3)-Qconv(x,xx,count3));
    Tnew(x,xx,count2)=T(x,xx,count3)+dT(x,xx,count3);

elseif xx==nlength %bottom right corner

Qconv(x,xx,count3)=2*hcomb*elementwidth*elementlength*(T(x,xx,count3)-
Tambient)+hcomb*Acy*(T(x,xx,count3)-Tambient)+hcomb*Acx*(T(x,xx,count3)-
Tambient);
    %grain center x conduction
    Qcond1(x,xx,count3)=K(x,xx)*Acx*(T(x,xx-1,count3)-
T(x,xx,count3))/dx;
    %grain center y conduction
    Qcond2(x,xx,count3)=K(x,xx)*Acy*(T(x-1,xx,count3)-
T(x,xx,count3))/dy;
    %total conduction

```

```

        Qcond(x,xx,count3)=Qcond1(x,xx,count3)+Qcond2(x,xx,count3);

dT(x,xx,count3)=timestep/(Density(x,xx)*Cp(x,xx)*elementlength*elementwidth*ele
mentthickness)*(Qcond(x,xx,count3)-Qconv(x,xx,count3));
        Tnew(x,xx,count2)=T(x,xx,count3)+dT(x,xx,count3);

        else %bottom horizontal edge

Qconv(x,xx,count3)=2*hcomb*elementwidth*elementlength*(T(x,xx,count3)-
Tambient)+hcomb*Acy*(T(x,xx,count3)-Tambient);
        %grain center x conduction
        Qcond1(x,xx,count3)=K(x,xx)*Acx*(T(x,xx+1,count3)+T(x,xx-
1,count3)-2*T(x,xx,count3))/dx;
        %grain center y conduction
        Qcond2(x,xx,count3)=K(x,xx)*Acy*(T(x-1,xx,count3)-
T(x,xx,count3))/dy;
        %total conduction
        Qcond(x,xx,count3)=Qcond1(x,xx,count3)+Qcond2(x,xx,count3);

dT(x,xx,count3)=timestep/(Density(x,xx)*Cp(x,xx)*elementlength*elementwidth*ele
mentthickness)*(Qcond(x,xx,count3)-Qconv(x,xx,count3));
        Tnew(x,xx,count2)=T(x,xx,count3)+dT(x,xx,count3);
        end

        elseif xx==1 && (x>1 || x<nwidth) % left vertical edge nodes

Qconv(x,xx,count3)=2*hcomb*elementwidth*elementlength*(T(x,xx,count3)-
Tambient)+hcomb*Acx*(T(x,xx,count3)-Tambient);
        %grain center x conduction
        Qcond1(x,xx,count3)=K(x,xx)*Acx*(T(x,xx+1,count3)-
T(x,xx,count3))/dx;
        %grain center y conduction
        Qcond2(x,xx,count3)=K(x,xx)*Acy*(T(x+1,xx,count3)+T(x-
1,xx,count3)-2*T(x,xx,count3))/dy;
        %total conduction
        Qcond(x,xx,count3)=Qcond1(x,xx,count3)+Qcond2(x,xx,count3);

dT(x,xx,count3)=timestep/(Density(x,xx)*Cp(x,xx)*elementlength*elementwidth*ele
mentthickness)*(Qcond(x,xx,count3)-Qconv(x,xx,count3));
        Tnew(x,xx,count2)=T(x,xx,count3)+dT(x,xx,count3);

        elseif xx==nlength && (x>1 || x<nwidth) % right vertical edge nodes

Qconv(x,xx,count3)=2*hcomb*elementwidth*elementlength*(T(x,xx,count3)-
Tambient)+hcomb*Acx*(T(x,xx,count3)-Tambient);
        %grain center x conduction
        Qcond1(x,xx,count3)=K(x,xx)*Acx*(T(x,xx-1,count3)-
T(x,xx,count3))/dx;

```



```

        %grain center y conduction
        Qcond2(x,xx,count3)=K(x,xx)*Acy*(T(x+1,xx,count3)+T(x-
1,xx,count3)-2*T(x,xx,count3))/dy;
        %total conduction
        Qcond(x,xx,count3)=Qcond1(x,xx,count3)+Qcond2(x,xx,count3);

dT(x,xx,count3)=timestep/(Density(x,xx)*Cp(x,xx)*elementlength*elementwidth*ele
mentthickness)*(Qcond(x,xx,count3)-Qconv(x,xx,count3));
        Tnew(x,xx,count2)=T(x,xx,count3)+dT(x,xx,count3);
%%%%%%%%%%%%%%%%%%%%%%%%%%%%%%%%%%%%%%%%%%%%%%%%%%%%%%%%%%%%%%%%%%%%%%%%
%Heat Input Nodes
%%%%%%%%%%%%%%%%%%%%%%%%%%%%%%%%%%%%%%%%%%%%%%%%%%%%%%%%%%%%%%%%%%%%%%%%
        elseif ((x>1 && x<nwidth) && (xx>1 && xx<nlength)) %central point
where heat is applied
            if (x==(round(nwidth/2))) && (xx==(round(nlength/2)))

Qconv(x,xx,count3)=2*hcomb*elementwidth*elementlength*(T(x,xx,count3)-
Tambient);

        %grain center x conduction
        Qcond1(x,xx,count3)=K(x,xx)*Acx*(T(x,xx+1,count3)+T(x,xx-
1,count3)-2*T(x,xx,count3))/dx;
        %grain center y conduction
        Qcond2(x,xx,count3)=K(x,xx)*Acy*(T(x+1,xx,count3)+T(x-
1,xx,count3)-2*T(x,xx,count3))/dy;
        %total conduction
        Qcond(x,xx,count3)=Qcond1(x,xx,count3)+Qcond2(x,xx,count3);
%%%%%%%%%%%%%%%%%%%%%%%%%%%%%%%%%%%%%%%%%%%%%%%%%%%%%%%%%%%%%%%%%%%%%%%%
%Heat Gen Portion
%%%%%%%%%%%%%%%%%%%%%%%%%%%%%%%%%%%%%%%%%%%%%%%%%%%%%%%%%%%%%%%%%%%%%%%%
%Johnson Cook Model for predicting Shear Stress
Tstar(count3)=(T(x,xx,count3)-Tambient)/(Tmelt-Tambient);
%determine drill tip depth and length of tip extending
%from part
bitrad=bitdiam/2;
bitslope=(bitrad-chiseledglength/2)/taperedlength;
%bitslope=taperedlength/(bitrad-chiseledglength/2);
distance(count3)=feedratem*time;
tipdist(count3)=distance(count3)-thickness;

drillradtip(count3)=tipdist(count3)*bitslope+chiseledglength/2;
        if drillradtip(count3)>bitrad
            drillradtip(count3)=bitrad;
        end
        drilldiamtip(count3)=2*drillradtip(count3);
        % tapered drill bit length slope used with distance to
        % find current radius

drillrad(count3)=distance(count3)*bitslope+chiseledglength/2;

```

```

%put limit on drill bit radius to match maximum
%radius/diameter
if drillrad(count3)>(bitdiam/2)
    drillrad(count3)=bitdiam/2;
elseif drillrad(count3)<chiseledglength
end
drilldiam(count3)=2*drillrad(count3);
%Velocities
%velocity(count3)=drillrad(count3)*angveloc/2; %avg
velocity at shear face
velocity(count3)=bitrad*angveloc/2; %avg velocity at shear
face
Vshear(count3)=velocity(count3)/cos(shearplanerad);
%Shear Strain Rate Determination

hyperbolacurv(count3)=chipthick^2/(16*C^2*sin(shearplanerad)^4*(tan(rakeanglerad)+cot(shearplanerad)));

shearstrainrate(count3)=velocity(count3)/(4*hyperbolacurv(count3)^0.5*sin(shearplanerad)^2*(tan(rakeanglerad)+cot(shearplanerad))^1.5);

shearstress(count3)=Farbodfactor*(AJC+BJC*fracstrain^nJC)*(1+CJC*log(shearstrainrate(count3)/strainrateref))*(1-Tstar(count3)^m);
    strainratetest=Vshear*6/(chipthick/sin(shearplanerad));
%
%     if distance(count3)<=thickness
%         conddist(count3)=thickness-distance(count3);
%     if conddist(count3)<0.0005
%         conddist(count3)=0.0005;
%     end
%     else
%         conddist(count3)=.0005;
%     end
%     conddist(count3)=chipthick;
%3 possible stages and equations for drilling, 1st is shoulder has not yet
contacted, second is shoulder is
%in contact but bit has not broken through the bottom yet, final step is bit is
coming out of the bottom
%sheet
%1st step: bit shoulder has not yet touched the top
%surace
A(count3)=(chipthick*(drilldiam(count3)-
chiseledglength))/(cos((pi/2)-pointanglerad)*sin(shearplanerad));
Aelec(count3)=A(count3)+Achisel;
if distance(count3)<taperedlength
    if time>timedelay% electricity turns on after this
delay

Resistance(count3)=Resistivity(x,xx)*conddist(count3)/Aelec(count3);

```

```

        Qelec(count3)=Current^2*Resistance(count3);
        CD(count3)=Current/(Aelec(count3)*1000^2);
        Fshear(count3)=A(count3)*shearstress(count3);

Qdeform(count3)=partheatfraction*Fshear(count3)*Vshear(count3);

Qfrict(count3)=mew*shearstress(count3)*drillrad(count3)*angveloc*A(count3);
        else %no electricity since delay has not expired

Resistance(count3)=Resistivity(x,xx)*conddist(count3)/Aelec(count3);
        Qelec(count3)=0;
        CD(count3)=0;
        Fshear(count3)=A(count3)*shearstress(count3);

Qdeform(count3)=partheatfraction*Fshear(count3)*Vshear(count3);

Qfrict(count3)=mew*shearstress(count3)*drillrad(count3)*angveloc*A(count3);
        end
        %2nd step should is inside workpiece but tip has not
        %left the bottom yet
        elseif distance(count3)>taperedlength &&
distance(count3)<=thickness
        upperlength(count3)=distance(count3)-taperedlength;

Qfrict(count3)=mew*shearstress(count3)*bitrad*angveloc*A(count3);

Resistance(count3)=Resistivity(x,xx)*conddist(count3)/(Aelec(count3));
        Qelec(count3)=Current^2*Resistance(count3);
        CD(count3)=Current/(Aelec(count3)*1000^2);
        Fshear(count3)=A(count3)*shearstress(count3);

Qdeform(count3)=partheatfraction*Fshear(count3)*Vshear(count3);
        %3rd step: drill tip is penetrating through until
        %shoulder leaves the bottom of sheet
        elseif distance(count3)>thickness
                Atop(count3)=(chipthick*(drilldiam(count3)-
chiseledglength))/(cos((pi/2)-pointanglerad)*sin(shearplanerad));
                Abottom(count3)=(chipthick*(drilldiamtip(count3)-
chiseledglength))/(cos((pi/2)-pointanglerad)*sin(shearplanerad));
                A(count3)=Atop(count3)-Abottom(count3);
                upperlength(count3)=distance(count3)-taperedlength;

Qfrict(count3)=mew*shearstress(count3)*bitrad*angveloc*(A(count3));

Resistance(count3)=Resistivity(x,xx)*conddist(count3)/(Aelec(count3));
        Qelec(count3)=Current^2*Resistance(count3);
        CD(count3)=Current/(Aelec(count3)*1000^2);
        Fshear(count3)=A(count3)*shearstress(count3);

```

```

Qdeform(count3)=parheatfraction*Fshear(count3)*Vshear(count3);

    end
    %Temperature change for central element
    %Qin(count3)=Qelec(count3)+Qfrict(count3)+Qdeform(count3);
    Qin(count3)=Qelec(count3)+Qdeform(count3);

dT(x,xx,count3)=(timestep/(Density(x,xx)*Cp(x,xx)*elementwidth*elementlength*th
ickness))*(Qin(count3)+Qcond(x,xx,count3)-Qconv(x,xx,count3));
    Tnew(x,xx,count2)=T(x,xx,count3)+dT(x,xx,count3);
    Fthrust(count3)=Fshear(count3)/cos(frictionanglerad-
rakeanglerad+shearplanerad);

    else
        %middle points

Qconv(x,xx,count3)=2*hcomb*elementwidth*elementlength*(T(x,xx,count3)-
Tambient);

        %grain center x conduction
        Qcond1(x,xx,count3)=K(x,xx)*Acx*(T(x,xx+1,count3)+T(x,xx-
1,count3)-2*T(x,xx,count3))/dx;
        %grain center y conduction
        Qcond2(x,xx,count3)=K(x,xx)*Acy*(T(x+1,xx,count3)+T(x-
1,xx,count3)-2*T(x,xx,count3))/dy;
        %total conduction
        Qcond(x,xx,count3)=Qcond1(x,xx,count3)+Qcond2(x,xx,count3);

dT(x,xx,count3)=(timestep/(Density(x,xx)*Cp(x,xx)*elementlength*elementwidth*el
ementthickness))*(Qcond(x,xx,count3)-Qconv(x,xx,count3));
    Tnew(x,xx,count2)=T(x,xx,count3)+dT(x,xx,count3);
    end
    end
    end
    end

T(:, :, count2)=Tnew(:, :, count2); %assign new temperature to main temperature
matrix and progress to next time step
end %end time stepped main loop
timesave2=timesave(1:end-1);
timesave(end)=timesave(end-1);
for i=1:iterations
    Ttest1(i)=T(round(nwidth/2),round(nlength/2),i)-273.15;
end

%data filtering variables
a=1;

```

```

q=.1;
b=[q q q q q q q q q];

%first data set
aldata=textscan(a1, repmat('%f', [1 4]), 'Delimiter', '\t', 'HeaderLines', 0);
alforcetime=aldata{1};
alforceforce=aldata{2};
altemptime=aldata{3};
altemptemp=aldata{4};
alforcetimeo=alforcetime;
alforceforceo=alforceforce;
altemptimeo=altemptime;
altemptempo=altemptemp;
alforcetime=filter(b,a,alforcetime);
alforceforce=filter(b,a,alforceforce);
altemptime=filter(b,a,altemptime);
altemptemp=filter(b,a,altemptemp);

%comparison plots between experimental data and model
figure(1)
plot(timesave,Ttest1,altemptime,altemptemp)
legend('model','experiment')
% title('350RPM0.5inmin')

figure(2)
plot(timesave2,Fthrust, alforcetime,alforceforce,timesave,Fshear,'--')
legend('model','experiment','shear')
title('350RPM0.5inmin')

fclose('all');

```

REFERENCES

1. National Highway Traffic Safety Administration. Final regulatory impact analysis: Corporate average fuel economy for MY 2012-MY 2016 passenger cars and light trucks. *Office of Regulatory Analysis and Evaluation, National Center for Statistics and Analysis*, (2010).
2. Lightweight materials for cars and trucks. *Office of Energy Efficiency and Renewable Energy*,
3. Dzialo, C., Siopis, M., Kinsey, B., & Weinmann, K. Effect of current density and zinc content during electrical-assisted forming of copper alloys. *CIRP Annals-Manufacturing Technology*, (2010). 59(1), 299-302.
4. Bunget, C., Salandro, W. A., & Mears, L. Tribological aspects in electrically-assisted forming. *MSEC2011-ASME 2011 International Manufacturing Science and Engineering Conference*, 723-730.
5. Golovashchenko, S. F., Krause, A., & Gillard, A. J. Incremental forming for aluminum automotive technology. *ASME 2005 International Mechanical Engineering Congress and Exposition*, American Society of Mechanical Engineers 323-329.
6. Kinsey, B. L., & Cao, J. An analytical model for tailor welded blank forming. *Journal of Manufacturing Science and Engineering*, (2003). 125(2), 344-351.
7. Jones, J. (2012). *Flow behavior modeling and process control of electrically-assisted forming (EAF) for sheet metals in uniaxial tension* (Ph.D.).
8. Ulutan, D., Pleta, A., & Mears, L. Electrically-assisted machining of titanium alloy ti-6Al-4V and nickel-based alloy IN-738: An investigation. *ASME 2015 International Manufacturing Science and Engineering Conference*, Charlotte NC. American Society of Mechanical Engineers V001T02A013-V001T02A013.
9. Magargee, J., Morestin, F., & Cao, J. Characterization of flow stress for commercially pure titanium subjected to electrically assisted deformation. *Journal of Engineering Materials and Technology*, (2013). 135(4), 041003.
10. Andrawes, J. S., Kronenberger, T. J., Perkins, T. A., Roth, J. T., & Warley, R. L. Effects of DC current on the mechanical behavior of AlMg1SiCu. *Materials and Manufacturing Processes*, (2007). 22(1), 91-101.

11. Wang, X., Xu, J., Jiang, Z., Zhu, W., Shan, D., Guo, B., & Cao, J. Size effects on flow stress behavior during electrically-assisted micro-tension in a magnesium alloy AZ31. *Materials Science and Engineering*, (2016). *A 659*, 215-224.
12. Zheng, Q., Shimizu, T., Shiratori, T., & Yang, M. Tensile properties and constitutive model of ultrathin pure titanium foils at elevated temperatures in microforming assisted by resistance heating method. *Materials & Design*, (2014). *63*, 389-397.
13. Kim, M., Vinh, N. T., Yu, H., Hong, S., Lee, H., Kim, M., Han, H. N., & Roth, J. T. Effect of electric current density on the mechanical property of advanced high strength steels under quasi-static tensile loads. *International Journal of Precision Engineering and Manufacturing*, (2014). *15*(6), 1207-1213.
14. Fan, R., Magargee, J., Hu, P., & Cao, J. Influence of grain size and grain boundaries on the thermal and mechanical behavior of 70/30 brass under electrically-assisted deformation. *Materials Science and Engineering: A*, (2013). *574*, 218-225.
15. Siopis, M. S., Kinsey, B. L., Kota, N., & Ozdoganlar, O. B. Effect of severe prior deformation on electrical-assisted compression of copper specimens. *Journal of Manufacturing Science and Engineering*, (2011). *133*(6), 064502.
16. Magargee, J., Fan, R., & Cao, J. Analysis and observations of current density sensitivity and thermally activated mechanical behavior in electrically-assisted deformation. *Journal of Manufacturing Science and Engineering*, (2013). *135*(6), 061022.
17. Pleta, A. D., Krugh, M. C., Nikhare, C., & Roth, J. T. An investigation of anisotropic behavior on 5083 aluminum alloy using electric current. *ASME 2013 International Manufacturing Science and Engineering Conference Collocated with the 41st North American Manufacturing Research Conference*, American Society of Mechanical Engineers V001T01A018-V001T01A018.
18. Xu, Q., Guan, L., Jiang, Y., Tang, G., & Wang, S. Improved plasticity of Mg–Al–Zn alloy by electropulsing tension. *Materials Letters*, (2010). *64*(9), 1085-1087.
19. Roth, J., Loker, I., Mauck, D., Warner, M., Golovashchenko, S., & Krause, A. Enhanced formability of 5754 aluminum sheet metal using electric pulsing. *Trans.North Am.Manuf.Res.Inst.SME*, (2008). *36*, 405-412.
20. Yang, D., & Conrad, H. Exploratory study into the effects of an electric field and of high current density electropulsing on the plastic deformation of TiAl. *Intermetallics*, (2001). *9*(10), 943-947.

21. Cao, W., Lu, X., & Conrad, H. Whisker formation and the mechanism of superplastic deformation. *Acta Materialia*, (1996). 44(2), 697-706.
22. Liu, S., Chen, C., Liu, P., & Chou, T. Tin whisker growth driven by electrical currents. *Journal of Applied Physics*, (2004). 95(12), 7742-7747.
23. Fukuda, Y., Osterman, M., & Pecht, M. The impact of electrical current, mechanical bending, and thermal annealing on tin whisker growth. *Microelectronics Reliability*, (2007). 47(1), 88-92.
24. Ross, C. D., Irvin, D. B., & Roth, J. T. Manufacturing aspects relating to the effects of direct current on the tensile properties of metals. *Journal of Engineering Materials and Technology*, (2007). 129(2), 342-347.
25. Perkins, T. A., Kronenberger, T. J., & Roth, J. T. Metallic forging using electrical flow as an alternative to warm/hot working. *Journal of Manufacturing Science and Engineering*, (2007). 129(1), 84-94.
26. Ross, C. D., Kronenberger, T. J., & Roth, J. T. Effect of dc on the formability of Ti-6Al-4V. *Journal of Engineering Materials and Technology*, (2009). 131(3), 031004.
27. Jones, J. J., Mears, L., & Roth, J. T. Electrically-assisted forming of magnesium AZ31: Effect of current magnitude and deformation rate on forgeability. *Journal of Manufacturing Science and Engineering*, (2012). 134(3), 034504.
28. Bunget, C. J., Salandro, W. A., & Mears, L. Sensitivities when modeling electrically-assisted forming. *ASME 2012 International Manufacturing Science and Engineering Conference Collocated with the 40th North American Manufacturing Research Conference and in Participation with the International Conference on Tribology Materials and Processing*, American Society of Mechanical Engineers 179-187.
29. Jones, J. J., & Mears, L. Constant current density compression behavior of 304 stainless steel and ti-6Al-4V during electrically-assisted forming. *ASME 2011 International Manufacturing Science and Engineering Conference*, American Society of Mechanical Engineers 629-637.
30. Salandro, W. (2012). *Thermo-mechanical modeling of the electrically-assisted manufacturing (EAM) technique during open die forging* (Ph.D.).
31. Egea, A. J. S., Rojas, H. A. G., Celentano, D. J., Travieso-Rodríguez, J. A., & Fuentes, J. L. Electroplasticity-assisted bottom bending process. *Journal of Materials Processing Technology*, (2014). 214(11), 2261-2267.

32. Li, X., Zhou, Q., Zhao, S., & Chen, J. Effect of pulse current on bending behavior of Ti6Al4V alloy. *Procedia Engineering*, (2014). 81, 1799-1804.
33. Jordan, A., & Kinsey, B. L. Investigation of thermal and mechanical effects during electrically-assisted microbending. *Journal of Materials Processing Technology*, (2015). 221, 1-12.
34. Kim, M., Vinh, N. T., Yu, H., Hong, S., Lee, H., Kim, M., Han, H. N., & Roth, J. T. Effect of electric current density on the mechanical property of advanced high strength steels under quasi-static tensile loads. *International Journal of Precision Engineering and Manufacturing*, (2014). 15(6), 1207-1213.
35. Ruskiewicz, B. J., Scriva, C., Reese, Z. C., Nikhare, C. P., Roth, J. T., & Ragai, I. Direct electric current spot treatment's effect on springback of 90 degree bent 2024-T3 aluminum. *ASME 2015 International Manufacturing Science and Engineering Conference*, American Society of Mechanical Engineers V001T02A109-V001T02A109.
36. Salandro, W. A., Bunget, C., & Mears, L. Modeling and quantification of the electroplastic effect when bending stainless steel sheet metal. *ASME 2010 International Manufacturing Science and Engineering Conference*, American Society of Mechanical Engineers 581-590.
37. Green, C. R., McNeal, T. A., & Roth, J. T. Springback elimination for al-6111 alloys using electrically-assisted manufacturing (EAM). *Trans.North Am.Manuf.Res.Inst.SME*, (2009). 37, 403-410.
38. Khal, A., Ruskiewicz, B. J., & Mears, L. Springback evaluation of 304 stainless steel in an electrically assisted air bending operation. *Proceedings of the 11th International Conference on Manufacturing Science and Engineering*, (2016).
39. Troitskii, O. Electromechanical effect in metals. *ZhETF Pisma Redaktsiiu*, (1969). 10, 18.
40. Conrad, H. Electroplasticity in metals and ceramics. *Materials Science and Engineering: A*, (2000). 287(2), 276-287.
41. Tang, G., Zhang, J., Zheng, M., Zhang, J., Fang, W., & Li, Q. Experimental study of electroplastic effect on stainless steel wire 304L. *Materials Science and Engineering: A*, (2000). 281(1), 263-267.
42. Conrad, H. A study into the mechanism (s) for the electroplastic effect in metals and its application to metalworking, processing and fatigue. *North Carolina State University at Raleigh Dept of Materials Science and Engineering*, (1989).

43. Sprecher, A., Mannan, S., & Conrad, H. Overview no. 49: On the mechanisms for the electroplastic effect in metals. *Acta Metallurgica*, (1986). 34(7), 1145-1162.
44. Spitsyn, V., & Troitskii, O. *Elektroplasticheskaya deformatsiya metallov (electroplastic deformation of metals)* Nauka. Moscow, Russia: (1985).
45. Troitskii, O., Spitsyn, N., Sokolov, N., & Ryzhkov, V. *Phys. Stat. Sol.*, (1978). 52(85)
46. Troitskii, O. Effect of the electron state of a metal on its mechanical properties and the phenomenon of electroplasticity. *Strength of Materials*, (1977). 9(1), 35-45.
47. Troitskii, O., & Likhtman, V. The anisotropy of the action of electron and radiation on the deformation of zinc single crystal in the brittle state. *Kokl.Akad.Nauk*, (1963). 148, 332-334.
48. Salandro, W., Jones, J., Bunget, C., Mears, L., & Roth, J. *Electrically assisted forming: Modeling and control*. Springer. (2014).
49. Nabarro, F. R. *Theory of crystal dislocations* Dover Publications. New York: (1967).
50. Spitsyn, V., & Troitskii, O. Simulation of the thermal and pinch effects of pulsed current on the plastic deformation of a metal. *Soviet Physics Doklady*, 132.
51. Okazaki, K., Kagawa, M., & Conrad, H. An evaluation of the contributions of skin, pinch and heating effects to the electroplastic effect in titanium. *Materials Science and Engineering*, (1980). 45(2), 109-116.
52. Kronenberger, T. J., Johnson, D. H., & Roth, J. T. Coupled multifield finite element analysis model of upsetting under an applied direct current. *Journal of Manufacturing Science and Engineering*, (2009). 131(3), 031003.
53. Khalilollahi, A., Johnson, D. H., & Roth, J. T. A comparative multifield FEA and experimental study on the enhanced manufacturability of 6061-T6511 aluminum using dc current. *Journal of Manufacturing Science and Engineering*, (2009). 131(6), 064503.
54. Hariharan, K., Lee, M., Kim, M., Han, H. N., Kim, D., & Choi, S. Decoupling thermal and electrical effect in an electrically assisted uniaxial tensile test using finite element analysis. *Metallurgical and Materials Transactions A*, (2015). 46(7), 3043-3051.
55. Timsit, R. Remarks on recent experimental observations of the electroplastic effect. *Scripta Metallurgica*, (1981). 15(4), 461-464.

56. Molotskii, M., & Fleurov, V. Magnetic effects in electroplasticity of metals. *Physical Review B*, (1995). 52(22), 15829.
57. Krokhin, A., Gumen, L., & Galligan, J. Tilt effect in the electron drag of dislocations in metals. *Philosophical Magazine A*, (1998). 77(2), 497-506.
58. Golovin, Y. I. Magnetoplastic effects in solids. *Physics of the Solid State*, (2004). 46(5), 789-824.
59. Andrawes, J. S., Heigel, J. C., Roth, J. T., & Warley, R. L. Effects of DC current on the stress-strain curve and hardness of 6061 T6511 aluminum. *ASME 2004 International Mechanical Engineering Congress and Exposition*, American Society of Mechanical Engineers 169-178.
60. Heigel, J. C., Andrawes, J. S., Roth, J. T., Hoque, M. E., & Ford, R. M. Viability of electrically treating 6061 T651 aluminum for use in manufacturing processes. *Transactions of the North American Research Institution of SME 2005*, (2005).
61. Gloeckner, J., Chiesa, S., Grimm, T., Ragai, I., & Roth, J. *The effects of rapid heating and compression on material properties. Proceedings of 2016 ASME International Manufacturing Science and Engineering Conference (MSEC2016)*, (2016).
62. Jiang, T., Peng, L., Yi, P., & Lai, X. Analysis of the electric and thermal effects on mechanical behavior of SS304 subjected to electrically assisted forming process. *Journal of Manufacturing Science and Engineering*, (2016). 138(6), 061004.
63. Ruszkiewicz, B., & Mears, L. Temperature controlled forming of 7075-T6 aluminum using linearly decaying direct electric current. *Journal of Manufacturing Science and Engineering*, (2016).
64. Bunget, C., Salandro, W., Mears, L., & Roth, J. T. Energy-based modeling of an electrically-assisted forging process. *Trans.North Am.Manuf.Res.Inst.SME*, (2010). 38, 647-654.
65. Lee, J., Kim, S., Lee, M., Song, J. H., Choi, S., Han, H. N., & Kim, D. Experimental and numerical study on the deformation mechanism in AZ31B mg alloy sheets under pulsed electric-assisted tensile and compressive tests. *Metallurgical and Materials Transactions A*, (2016). 47(6), 2783-2794.
66. Goldman, P., Motowidlo, L., & Galligan, J. The absence of an electroplastic effect in lead at 4.2 K. *Scripta Metallurgica*, (1981). 15(4), 353-356.

67. Jordan, A., & Kinsey, B. L. Investigation of thermal and mechanical effects during electrically-assisted microbending. *Journal of Materials Processing Technology*, (2015). 221, 1-12.
68. Wang, X., Xu, J., Shan, D., Guo, B., & Cao, J. Modeling of thermal and mechanical behavior of a magnesium alloy AZ31 during electrically-assisted micro-tension. *International Journal of Plasticity*, (2016). 85, 230-257.
69. Siopis, M. S., & Kinsey, B. L. Experimental investigation of grain and specimen size effects during electrical-assisted forming. *Journal of Manufacturing Science and Engineering*, (2010). 132(2), 021004.
70. Kinsey, B., Cullen, G., Jordan, A., & Mates, S. Investigation of electroplastic effect at high deformation rates for 304SS and Ti–6Al–4V. *CIRP Annals-Manufacturing Technology*, (2013). 62(1), 279-282.
71. Kang, W., Beniam, I., & Qidwai, S. M. In situ electron microscopy studies of electromechanical behavior in metals at the nanoscale using a novel microdevice-based system. *Review of Scientific Instruments*, (2016). 87(9), 095001.
72. Molotskii, M. I. Theoretical basis for electro-and magnetoplasticity. *Materials Science and Engineering: A*, (2000). 287(2), 248-258.
73. Kim, S., Kim, S., Yoo, D., Lee, J., Rhyim, Y., & Kim, D. Evaluation of the athermal effect of electric pulsing on the recovery behavior of magnesium alloy. *Metallurgical and Materials Transactions A*, (2016). 47(12), 6368-6373.
74. Kishkin, S., & Klypin, A. Effects of electrical and magnetic action on the creep of metals and alloys. *Doklady Akad. Nauk SSSR*, 325-327.
75. Callister, W. D., & Rethwisch, D. G. *Materials science and engineering: An introduction* Wiley New York. (2007).
76. Morris, J. W. (2013). Defects in crystals. *Materials science and engineering: An introduction* (pp. 76-107) Wiley.
77. Ashcroft, N. W., & Mermin, N. D. Solid state physics (holt, rinehart and winston, new york, 1976). *There is no Corresponding Record for this Reference*, (2005). , 490-495.
78. Van Vliet, K. J. 3.032 mechanical behavior of materials. *Massachusetts Institute of Technology, Cambridge, MA*, (2006).

79. Burgers vector. Retrieved from <https://www.doitpoms.ac.uk/tlplib/dislocations/burgers.php>
80. Gottstein, G. *Physical foundations of materials science* Springer Science & Business Media. (2013).
81. Kocks, U., & Mecking, H. Physics and phenomenology of strain hardening: The FCC case. *Progress in Materials Science*, (2003). 48(3), 171-273.
82. Barlat, F., Glazov, M., Brem, J., & Lege, D. A simple model for dislocation behavior, strain and strain rate hardening evolution in deforming aluminum alloys. *International Journal of Plasticity*, (2002). 18(7), 919-939.
83. Polmear, I. *Light alloys* Arnold. London, UK, (1995).
84. Aluminum corrosion resistance. Retrieved from <http://www.aluminiumdesign.net/design-support/aluminium-corrosion-resistance/>
85. DeGarmo, E. P., Black, J. T., Kohser, R. A., & Klamecki, B. E. *Materials and process in manufacturing* Prentice Hall. (1997).
86. America, E. N. *Understanding the Aluminum Alloy Designation System*, (2011).
87. Aluminum strengthening mechanisms. Retrieved from <http://www.aluminiumindustry.org/en/aluminum-strengthening-mechanisms.html>
88. Ma, K., Wen, H., Hu, T., Topping, T. D., Isheim, D., Seidman, D. N., Lavernia, E. J., & Schoenung, J. M. Mechanical behavior and strengthening mechanisms in ultrafine grain precipitation-strengthened aluminum alloy. *Acta Materialia*, (2014). 62, 141-155.
89. Huang, X., Kamikawa, N., & Hansen, N. Strengthening mechanisms in nanostructured aluminum. *Materials Science and Engineering: A*, (2008). 483, 102-104.
90. MATWEB. Aluminum 7075-T6; 7075-T651. Retrieved from <http://asm.matweb.com/search/SpecificMaterial.asp?bassnum=MA7075T6>
91. Park, J., & Ardell, A. Microstructures of the commercial 7075 al alloy in the T651 and T7 tempers. *Metallurgical Transactions A*, (1983). 14(10), 1957-1965.
92. ALCOA. (2006). Alloy 7075 plate and sheet. Retrieved from http://www.arconic.com/mill_products/catalog/pdf/alloy7075techsheet.pdf

93. Speedy Metals. 7075 aluminum bar. Retrieved from <https://www.speedymetals.com/information/Material7.html>
94. Hariharan, K., Kim, M. J., Hong, S., Kim, D., Song, J., Lee, M., & Han, H. N. Electroplastic behaviour in an aluminium alloy and dislocation density based modelling. *Materials & Design*, (2017). doi:10.1016/j.matdes.2017.03.072
95. Pierce, D., & Brusius, P. Electromigration: A review. *Microelectronics Reliability*, (1997). 37(7), 1053-1072.
96. Ho, P. S., & Kwok, T. Electromigration in metals. *Reports on Progress in Physics*, (1989). 52(3), 301.
97. Psyk, V., Risch, D., Kinsey, B., Tekkaya, A., & Kleiner, M. Electromagnetic forming—a review. *Journal of Materials Processing Technology*, (2011). 211(5), 787-829.
98. Brar, N., Joshi, V., & Harris, B. Constitutive model constants for Al7075-t651 and Al7075-t6. *SHOCK COMPRESSION OF CONDENSED MATTER 2009: Proceedings of the American Physical Society Topical Group on Shock Compression of Condensed Matter*, AIP Publishing 945-948.
99. Kino, T., Endo, T., & Kawata, S. Deviations from Matthiessen's rule of the electrical resistivity of dislocations in aluminum. *Journal of the Physical Society of Japan*, (1974). 36(3), 698-705.
100. Rider, J., & Foxon, C. An experimental determination of electrical resistivity of dislocations in aluminium. *Philosophical Magazine*, (1966). 13(122), 289-303.
101. Karolik, A., & Luhvich, A. Calculation of electrical resistivity produced by dislocations and grain boundaries in metals. *Journal of Physics: Condensed Matter*, (1994). 6(4), 873.
102. Zhao, J., Wang, G. X., Dong, Y., & Ye, C. Multiscale modeling of localized resistive heating in nanocrystalline metals subjected to electropulsing. *Journal of Applied Physics*, (In Press).
103. Kalpakjian, S., & Schmid, S. R. *Manufacturing processes for engineering materials* (5th ed.) Prentice Hall. New Jersey, USA: (2008).
104. Clark, K. W., Zhang, X., Vlassioux, I. V., He, G., Feenstra, R. M., & Li, A. Spatially resolved mapping of electrical conductivity across individual domain (grain) boundaries in graphene. *ACS Nano*, (2013). 7(9), 7956-7966.

105. Bridgman, P. W. Compressibilities and electrical resistance under pressure, with special reference to intermetallic compounds. *Proceedings of the American Academy of Arts and Sciences*, JSTOR 285-317.
106. Jacumasso, S. C., Martins, J. d. P., & Carvalho, André Luís Moreira de. Analysis of precipitate density of an aluminium alloy by TEM and AFM. *REM-International Engineering Journal*, (2016). 69(4), 451-457.
107. Meyers, M. A., & Ashworth, E. A model for the effect of grain size on the yield stress of metals. *Philosophical Magazine A*, (1982). 46(5), 737-759.
108. McNeal, T. A., Beers, J. A., & Roth, J. T. The microstructural effects on magnesium alloy AZ31B-O while undergoing an electrically-assisted manufacturing process. *Proceedings of the ASME 2009 International Manufacturing Science and Engineering Conference*, 1-10.
109. Woodford, C. (2017). Electron microscopes. Retrieved from <http://www.explainthatstuff.com/electronmicroscopes.html>
110. Handbook, A. Heat treating. *Vol*, (1991). 4, 744.
111. Baranov, S., Staschenko, V., Sukhov, A., Troitskiy, O., & Tyapkin, A. Electroplastic metal cutting. *Russian Electrical Engineering*, (2011). 82(9), 477-479.
112. Jones, E., Jones, J. J., & Mears, L. Empirical modeling of direct electric current effect on machining cutting force. *ASME 2013 International Manufacturing Science and Engineering Conference Collocated with the 41st North American Manufacturing Research Conference*, American Society of Mechanical Engineers V001T01A059-V001T01A059.
113. Egea, A. J. S., Rojas, H. A. G., Montaña, C. A. M., & Echeverri, V. K. Effect of electroplastic cutting on the manufacturing process and surface properties. *Journal of Materials Processing Technology*, (2015). 222, 327-334.
114. Merchant, M. E. Mechanics of the metal cutting process. I. orthogonal cutting and a type 2 chip. *Journal of Applied Physics*, (1945). 16(5), 267-275.
115. Tay, A., Stevenson, M., de Vahl Davis, G., & Oxley, P. A numerical method for calculating temperature distributions in machining, from force and shear angle measurements. *International Journal of Machine Tool Design and Research*, (1976). 16(4), 335-349.

116. Vedantam, K., Bajaj, D., Brar, N., & Hill, S. Johnson-cook strength models for mild and dp 590 steels. *AIP Conference Proceedings*, IOP Institute of Physics Publishing Ltd 775.
117. Hameed, S., Rojas, H. A. G., Egea, A. J. S., & Alberro, A. N. Electroplastic cutting influence on power consumption during drilling process. *The International Journal of Advanced Manufacturing Technology*, (2016). 87(5-8), 1835-1841.
118. Davidson, S. R., & James, D. F. Drilling in bone: Modeling heat generation and temperature distribution. *Journal of Biomechanical Engineering*, (2003). 125(3), 305-314.
119. Axelrod, J. (2013). Know temperature when metal glows red. Retrieved from <http://www.hearth.com/talk/wiki/know-temperature-when-metal-glows-red/>

LIST OF JOURNAL ARTICLES

1. **Ruszkiewicz, B. J.**, Grimm, T. Ragai, I., Mears, L., Roth, J.T., “A Review of Electrically-Assisted Manufacturing with Emphasis on Modeling and Understanding of the Electroplastic Effect.” *ASME. J. Manuf. Sci. Eng.* 2017; doi:10.1115/1.4036716.
2. **Ruszkiewicz, B. J.**, & Mears, L. (2016). “Temperature-Controlled Forming of 7075-T6 Aluminum Using Linearly Decaying Direct Electric Current.” *ASME. J. Manuf. Sci. Eng.* 2016; 138(9):091009-091009-9. doi:10.1115/1.4033902.
3. **Ruszkiewicz, B.J.**, Mears, L. (2017). “Evaluation of Grain Boundary Joule Heating as the Explanation of the Transient Electroplastic Effect in Pulsed Tension of 7075-T6 Aluminum. *ASME. J. Manuf. Sci. Eng. Submitted.*
4. **Ruszkiewicz, B.J.**, Gendreau, E., Niaki, F., & Mears, L. (2017). “Modeling and Investigation of Electroplastic Drilling of Mild Steel.” *ASME. J. Manuf. Sci. Eng. Submitted.*
5. **Ruszkiewicz, B.J.**, & Mears, L. (2017). “Evaluation of Current Density as the Representation of the Quantity of Applied Electric Current in Electrically-assisted Manufacturing” *ASME. J. Manuf. Sci. Eng. Expected Feb. 2018.*

CONFERENCE PROCEEDINGS AND PRESENTATIONS

1. **Ruszkiewicz, B.J.**, Gendreau, E., Niaki, F., & Mears, L. (2017). "An Investigation of Electroplastic Drilling of Mild Steel." *Proceedings of the 12th International Conference on Manufacturing Science and Engineering*, June 4-8, Los Angeles, CA.
2. Karumatt, N.G., **Ruszkiewicz, B.J.**, & Mears, L. (2017). "Electrically-assisted Drilling of USIBOR1500 Steel and its Implications for Electrically-assisted Machining." *Proceedings of the 12th International Conference on Manufacturing Science and Engineering*, June 4-8, Los Angeles, CA.
3. Khal, A., **Ruszkiewicz, B. J.**, & Mears, L., (2016). "Springback Evaluation of 304 Stainless Steel in an Electrically-assisted Air Bending Operation." *Proceedings of the 11th International Conference on Manufacturing Science and Engineering*, June 27-July 1, Blacksburg, VA.
4. Neveux, T., **Ruszkiewicz, B. J.**, Roth, J.T., Ragai, I., (2016). "Electrically-assisted Global Springback Elimination After Single Point Incremental Forming," *Proceedings of the 11th International Conference on Manufacturing Science and Engineering*, June 27-July 1, Blacksburg, VA.
5. Skovron, J., **Ruszkiewicz, B. J.**, Mears, L., (2016). "Electrically-assisted Flow Drill Screwing of 6063 Aluminum." *Proceedings of the 11th International Conference on Manufacturing Science and Engineering*, June 27-July 1, Blacksburg, VA.
6. **Ruszkiewicz, B. J.**, Mears, L., (2016). "Electrically-assisted Compression of Tungsten Carbide and its Implications for Electrically-assisted Machining." *Proceedings of the 11th International Conference on Manufacturing Science and Engineering*, June 27-July 1, Blacksburg, VA.
7. **Ruszkiewicz, B. J.**, Roth, J. T., Johnson, D. H., (2015). "Locally Applied Direct Electric Current's Effect on Springback of 2024-T3 Aluminum After Single Point Incremental Forming," *Proceedings of the 10th International Conference on Manufacturing Science and Engineering*, June 8-12, Charlotte, NC.
8. **Ruszkiewicz, B. J.**, Scriva, C., Reese, Z.C., Nihare, C. P., Roth, J. T., Ragai, I., (2015). "Direct Electric Current Spot Treatment's Effect on Springback of 90 Degree Bent 2024-T3 Aluminum," *Proceedings of the 10th International Conference on Manufacturing Science and Engineering*, June 8-12, Charlotte, NC.